

CHAPTER 9

PHYSICS STUDIES WITH THE ADDITIONAL HEATING SYSTEMS IN JET

J.-M. NOTERDAEME,^{a,b*} L.-G. ERIKSSON,^c M. MANTSINEN,^d M.-L. MAYORAL,^e
D. VAN EESTER,^f J. MAILLOUX,^e C. GORMEZANO,^g and T. T. C. JONES^e

^aMax-Planck-Institut für Plasmaphysik, Euratom-Association IPP, D-85740 Garching, Germany

^bUniversity of Gent, Electrical Energy, Systems, and Automation Department, Gent, Belgium

^cAssociation Euratom-CEA, CEA/DSM/DRFC Centre de Cadarache, 13108 St. Paul lez Durance, France

^dHelsinki University of Technology, EURATOM-Association TEKES, Helsinki, Finland

^eEuratom/UKAEA Fusion Association, Culham Science Centre, Abingdon, Oxon OX14 3DB, United Kingdom

^fLaboratory for Plasmas Physics, Association “EURATOM – Belgian State,” ERM-KMS, Trilateral Euregio Cluster Brussels, Belgium

^gFormer Member of the JET Joint Undertaking

Received August 1, 2007

Accepted for Publication November 14, 2007

The physics studies of the three “heating” systems that are installed on JET are reviewed. Results from the beginning of JET up to now are presented with some emphasis on the more recent ones. The systems were used not only for heating, where JET has laid the groundwork to qualify them for heating the next generation of machines to ignition, but also increasingly as tools to control the plasma. This role, already exploited on JET, will

become more and more important in the next machine, since main heating will be provided by the alpha-particle heating and one will have to rely on the heating systems to control the plasma during the burn.

KEYWORDS: ICRF, lower hybrid, neutral beam

Note: Some figures in this paper are in color only in the electronic version.

Contents—Chapter 9

I. INTRODUCTION

II. ION CYCLOTRON RESONANCE HEATING AND CURRENT DRIVE ON JET

II.A. Introduction

II.B. Some ICRF Heating Physics

II.C. Overview of the JET ICRF Systems

II.D. Development of ICRF Heating Scenarios

II.D.1. Heating in (D-T) Plasmas

II.D.1.a. D-T Experiments in 1997: Fundamental Deuterium Minority Heating and ³He Minority Combined with Harmonic Tritium Heating

II.D.1.b. Trace Tritium Experiments in 2003

II.D.1.c. Neutron Production due to Reactions Between ICRF-Accelerated Protons with Tritium

II.D.2. Mode Conversion in (³He)-D and (³He)-⁴He Plasmas

II.D.3. Inverted Minority Heating and Mode Conversion Scenario in (³He)-H and (D)-H Plasmas

II.D.4. Minority Heating in (H)-D and (³He)-D Plasmas

II.D.4.a. Polychromatic Heating

II.D.4.b. ICRF-Induced Spatial Transport

II.D.5. Second-Harmonic Minority Heating and Finite Larmor Radius Effect in (H)-D Plasmas

II.E. ICRF Current Drive

II.E.1. Ion Cyclotron Current Drive for Sawtooth and Neoclassical Tearing Mode Control

II.E.2. Fast-Wave Current Drive

II.F. ICRF Rotation

II.G. ICRF as a Tool

II.G.1. Alpha Tail Production

II.G.2. Plasma Start-Up

II.G.3. Simulation of the Dynamics of Burning Plasma

II.G.4. ICRF Power Modulation for Transport Studies

II.G.5. ELM Toroidal Propagation

II.H. Outlook and Conclusions

III. PHYSICS OF NBI IN JET

III.A. Introduction

III.B. Technical Overview and Evolution of the JET NB Injectors

III.C. Coupling of NB Power to JET Plasma and Operating Limitations

III.D. Application of NB Heating for High Fusion Performance Plasmas

*E-mail: noterdaeme@ipp.mpg.de

III.E. Fueling	IV.D.2. Counter-Current Drive Experiments
III.E.1. Global Plasma Fueling and Particle Confinement	IV.D.3. Electron ITBs
III.E.2. Local Particle Transport	IV.D.4. Damping of the LH Wave on Energetic Ions
III.F. NB Current Drive	IV.E. LHCD as a Tool
III.F.1. Theoretical Considerations	IV.E.1. Sawtooth Control of Hot-Ion H-Modes
III.F.2. NB Current Drive Experiments in JET	IV.E.2. The Role of LHCD in the Optimized Shear Configuration Development
III.G. Toroidal Rotation	IV.E.3. LHCD as a Tool to Change Plasma Current Profile in Noninductive Steady-State Scenarios
III.H. Conclusion and Outlook	IV.E.4. Toward Fully Noninductive ITB Plasmas with LHCD
IV. LHCD STUDIES AT JET	IV.E.5. LHCD in Real-Time Current Profile Control Development
IV.A. Introduction	IV.E.6. Role of LHCD in Hybrid Scenario Development
IV.B. Description and Limits of the LHCD System	IV.E.7. LHCD for NTM Control
IV.C. Coupling Issues	IV.F. CONCLUSIONS
IV.C.1. Optimization of LH Wave Coupling	REFERENCES
IV.C.2. LH Coupling in ITER-Like Conditions	
IV.C.3. SOL Characterization During LH and Gas Puffing and Modeling	
IV.C.4. Effect of ICRF on LH Coupling	
IV.D. LHCD Efficiency and Other Physics Issues	
IV.D.1. Operation Near to Fully Noninductive Current Drive	

I. INTRODUCTION

Since the beginning of the design of JET, one of the major research objectives was defined as “the study of plasma heating.” Several steps were envisaged, with an initial additional heating capability of 3 MW. More than 25 and eventually 50 MW were considered.

The first technique to be envisaged was neutral beam injection (NBI), which had already proved to be an efficient method of plasma heating on magnetic confinement fusion devices at the time the auxiliary heating requirements for JET were being defined. However, the development toward the multimewatt, 10-s capability needed for JET was an enormous step, with a target of 10 MW of net NBI power to be delivered through a single port. At the end of 1981, the project decided to increase further the heating systems’ capability by authorizing the construction of a second neutral beam line using a second port and of a new heating system based on rf waves in the ion cyclotron range of frequencies (ICRF) at a level of 15 MW, which was also a very large step compared to existing systems. The ICRF antennas were installed on the low-field side of the vessel along the wall between ports. A prototype ICRF antenna was the first system to deliver additional power in JET in 1984. Development of new antennas has since been proceeding and is still going on. The decision concerning a current drive system came later, in 1987, when confinement degradation with input power, which was not linked to a specific heating scheme, became apparent. The main objective was to study the effect of plasma current profile control on confinement and to provide data on possible steady-state operation of large tokamaks. Lower hybrid current drive (LHCD) was selected, using a single port and with power in the range of 8 to 10 MW.

The achievements in plasma heating and current drive with ICRF waves are summarized in Sec. II. The key

results over the present duration of the project (1983 through 2006) are covered, with emphasis on the more recent developments. The ground was laid by the success of the early experiments, with the achievement of 22 MW of ICRF power coupled to limiter plasmas and validation of minority hydrogen and ³He heating scenarios, including key observations of confinement degradation with external power and monster sawteeth. In 1997 a D-T campaign resulted in validation of ITER ICRF scenarios. More recent achievements include the development of ICRF mode conversion with real-time control of ³He in 2001 through 2003 and the demonstration of induced radial transport of resonant ions. ICRF waves are routinely used for heating and plasma control in all regimes of JET operation as well as in alpha particle physics studies and experiments on plasma heat transport. This section was written by L. G. Eriksson, M. Mantsinen, M.-L. Mayoral, J.-M. Noterdaeme, and D. Van Eester.

The main achievements of NBI heating and current drive are described in Sec. III. However, since NBI was involved in almost all of the JET experimental program, only the highlights of the NBI physics and applications are given here. These include the use of NBI heating to produce high fusion performance plasmas (including D-T), as well as specific neutral beam (NB) physics effects such as beam fueling (including helium and tritium injection), current drive, and beam-driven rotation that are all very important for the development of scenarios for ITER, for both the reference scenario (see Chap. 3 of this issue) and the advanced scenarios (see Chap. 4 of this issue). A brief technical overview and evolution of the JET NB injectors as well as operating limitations are given. This section was written by T. T. C. Jones.

The description and achievements of the LHCD system are described in Sec. IV. Some limiting technical problems that impact the physics program are also addressed. Achieving sufficient coupling has been one of

the major challenges of the LHCD experiments at JET. Major breakthroughs in coupling are described, including the development of techniques allowing good coupling to be achieved in the most extreme ITER-like conditions. The main results associated with the initial goals of the LHCD system including current drive and current profile control are discussed. LHCD has become progressively an important part of the JET experimental program and is now routinely used for the development of advanced scenarios and the control of magnetohydrodynamics (MHD) in the ITER reference scenarios. This section was written by C. Gormezano and J. Mailloux.

II. ION CYCLOTRON RESONANCE HEATING AND CURRENT DRIVE ON JET

II.A. Introduction

This section summarizes the JET achievements in the study of plasma heating and current drive using waves in the ICRF, with an emphasis on the more recent results. Reviews of earlier results can be found in Refs. 1 through 6.

An overview of the evolution of the ICRF system can be found in Chap. 2 of this journal issue, Sec. V.B. At the time of the JET design, techniques available for heating the plasma were neutral beam heating and heating with waves in the range of ion cyclotron resonance frequencies. Initially, a few megawatts from both systems were planned, to be increased later to 25 MW of neutral beam heating and 15 MW of ion cyclotron power. By 1988 both systems were capable of providing about 20 MW of power.

With the introduction of initially up to 3 MW of ion cyclotron resonance heating, the first indication of confinement degradation, already seen on smaller tokamaks, was observed¹: Increasing the heating power reduced the energy confinement time. Impurity effects were modest and did not play a significant role. Temperatures of up to 3 keV were obtained for both ions and electrons. As the power was increased, very large sawteeth⁷ would appear above a certain power level. In one of the first applications of ICRF beyond heating, ICRF minority current drive near the $q = 1$ surface⁸ was used to control the sawtooth instability. A sustained H-mode was obtained with ICRF alone, but operation with large ELMs was problematic: The edge density variations due to the ELMs led to large and fast coupling variations the system could not cope with.

ICRF heating is now routinely used in all regimes of operation at JET, and more specifically for L-H mode and H-L mode threshold studies (e.g., Ref. 9), comparison of confinement between NBI- and ICRF-heating-induced H-modes,¹⁰ for ITER physics experiments such as ρ^* scaling and beta limits,¹¹ for testing ITER-relevant ICRF scenarios,^{12–15} and for combined heating in high-performance plasmas^{5,6,16–18} and alpha particle physics

studies.¹⁹ Progress has been and is still being made in coupling high power to strongly ELMy plasmas.

The section is organized as follows. In Sec. II.B the basic physics of ICRF heating and current drive are discussed. An introduction to the JET ICRF systems is given in Sec. II.C. The wide range of choices for the interaction mechanisms allows a large range of options for heating and controlling the plasma. Sections II.D and II.E summarize the JET results on the extensive studies of the different heating and current drive scenarios. Because ICRF can easily separate heating and momentum input, it can be used to investigate the plasma rotation, discussed in Sec. II.F. In Sec. II.G, further applications are presented that make ICRF an interesting tool to explore ITER-relevant issues such as fast particles, plasma start-up, and transport.

II.B. Some ICRF Heating Physics

Heating with ICRF waves is one of the main auxiliary plasma heating mechanisms used in existing fusion devices. It is one of the methods planned for the next-step reactor ITER to heat the plasma to high temperatures required for fusion but also to tackle other tasks such as fusion burn control and control of plasma instabilities.

In the ICRF heating scheme, waves are launched into the plasma using a number of external antennas. The waves propagate until they are absorbed by one or more mechanisms or are transformed to another type of wave. The propagating wave is typically the fast wave; the transformation to another wave is called mode conversion.

Absorption occurs when the frequency matches the local fundamental ion cyclotron resonance frequency of one of the ion species in the plasma—hence the name—or a harmonic of it. The ions can be a minority species or the bulk, and the heating leads to a more or less energetic tail formation, or to bulk ion heating. Subpopulations with highly energetic (suprathermal) tails transfer their energy via Coulomb collisions to the bulk particles. The fast ion energy is transferred to the bulk ions or to the electrons, depending on the tail energy and the electron temperature.

Therefore, in some of the ICRF heating schemes that heat resonantly, ions end up providing dominantly electron rather than bulk ion heating. This occurs when only a small fraction of the ions in the plasma interacts efficiently with the ICRF waves. In the minority heating scheme, the minority species absorbs the wave power resonantly at its fundamental cyclotron resonance. With higher harmonic heating of a majority species ($\omega = n\omega_{ci}$, $n \geq 2$), the absorption mechanism is a finite Larmor radius effect and only the more energetic ions interact effectively with the waves. When the fundamental resonance of a minority corresponds to the harmonic of a bulk ion, the partitioning of the power between tail formation of the minority (H) and the further acceleration of the most energetic bulk (in this case D) ions depends

on the plasma parameters and the power density and is well understood. ICRF heating tends to accelerate relatively few resonating ions to high energies. The energetic resonating ions then transfer the absorbed wave power to the bulk plasma via collisions. However, since they are energetic, their averaged energy often exceeds the critical energy E_c at which collisions with bulk ions and electrons are equally strong, resulting in dominant collisional electron heating.

Conversion to one or more waves occurs in multi-species plasmas. The excited waves are commonly absorbed by electron Landau damping (ELD) and transit time magnetic pumping (TTMP) on the electrons, or by nonlinear effects on ions.

The combination of the frequency, the magnetic field, and the concentration of ion species (in the case of mode conversion) allows the interaction of the wave to occur at a chosen location in the plasma: the center, the high field side (HFS), or the low field side (LFS). This ample choice of options gives a large range of possibilities to influence the temperature and even the distribution function of different species (bulk ions or electrons, or ion subpopulations).

II.C. Overview of the JET ICRF Systems

An introduction to the JET ion cyclotron heating system together with some early results is given in Refs. 3 and 20. The technical aspects of the ICRF system are dealt with in Refs. 21 and 22.

The ICRF system on JET has a broad frequency range (23 to 57 MHz), providing access to a large number of scenarios for a wide range of magnetic fields.

ICRF heating started with two prototype antennas¹ (A01 and A02), designed to couple the power (6 MW was available) in limiter configuration. Both antennas had two poloidal straps. Whereas one antenna had the two straps in the same poloidal plane next to each other, end-fed (one at the top, one at the bottom) with short circuit in the equatorial plane, the other antenna had the two straps toroidally side by side, both center-fed with shorts top and bottom.

In a next step, eight antennas (A1) were installed in the torus, each with two poloidal straps, toroidally side by side. These antennas too were designed for limiter operation and had screen bars made of beryllium, approximately aligned to the magnetic field. Each antenna was powered through a network of coaxial transmission lines by two combined 2-MW generators. Up to 22 MW was coupled to the plasma.³

Since the change-over of JET from a limiter to a divertor machine, the waves are launched in the plasma with four arrays of antennas with four straps each.²¹ The phasing between the straps in one array can be chosen arbitrarily, but the combinations used most are the so-called dipole phasing $(0, \pi, 0, \pi)$ to launch waves with a symmetric toroidal mode number spectrum peaking at

$|n_\phi| \approx 27$, the +90-deg antenna phasing $(0, \pi/2, \pi, 3\pi/2)$ to launch waves predominantly in the co-current direction with an asymmetric toroidal mode number spectra peaking at $|n_\phi| \approx 14$, and the -90-deg antenna phasing $(0, -\pi/2, -\pi, -3\pi/2)$ for waves predominantly in the counter-current direction.

More recently, a number of enhancements have been made to allow the ICRF to cope with the strong and fast coupling variations, a result of the edge density variations caused by the edge-localized modes (ELMs). A standard matching system cannot cope with those fast variations.²³ On two of the four antenna arrays, 3-dB couplers were installed, a method originally suggested in Ref. 24 and very successfully implemented on ASDEX Upgrade.²⁵ As an alternative method to cope with ELMs, conjugate matching was installed on a third array.²⁶ Both systems confirm that ELMs can be effectively coped with. A new antenna²⁷ that incorporates both internal conjugate T-matching and an external 3-dB coupler will be tested in 2008.

II.D. Development of ICRF Heating Scenarios

II.D.1. Heating in (D-T) Plasmas

Since ion cyclotron resonance heating is the only heating method capable of heating ions in the dense core of a tokamak fusion reactor, it is a prime candidate to heat a plasma to ignition. For fusion reactors based on the D-T reaction, a logical choice is to tune the ICRF system to heat the D or T fuel ions. The wide frequency band of its ICRF system, its ability to confine very energetic particles, and its tritium capability make JET particularly apt to test ICRF heating scenarios likely to be exploited in future fusion reactors. Experiments were performed with ICRF only and in high-performance (e.g., optimized shear or hot-ion H-mode) pulses relying on NBI as well as ICRF heating. Extensive investigations were done in a campaign with full D-T experiments in 1997 and a campaign with trace T experiments in 2003. The D-T campaigns focused on addressing problems of how to reach fusion-relevant temperatures, on the development of diagnostics for plasmas in which fusion processes occur, and on the effect of fusion-born particles on the machine and its performance.

II.D.1.a. D-T Experiments in 1997: Fundamental Deuterium Minority Heating and ³He Minority Combined with Harmonic Tritium Heating. In the 1997 JET D-T campaign, both deuterium and tritium heating schemes were tested using H-mode single-null divertor plasmas with ITER shapes, edge safety factors q_{95} in the range $3.4 < q_{95} < 3.9$, and dipole phasing of the ICRF antennas.^{13,17,28-30} The potential of deuterium minority heating in tritium plasmas was demonstrated for the first time. Second-harmonic tritium produced energetic tritons above the critical energy, but it was demonstrated that adding a small minority of ³He ions

increases the fusion reactivity significantly. Tritium minority ICRF heating was shown to be a promising candidate to achieve bulk ion heating and create suprathreshold tritons. The discharges discussed in this paper are solely heated by ohmic and ICRF heating. For diagnostic purposes short “blips” of an NBI unit are required. When analyzing the data (e.g., the neutron yield), these time intervals are omitted except for the (charge-exchange) diagnostic data relying on them.

II.D.1.a.i. Fundamental Deuterium Cyclotron Heating. The experiments to test and optimize the deuterium minority heating scheme were carried out at 28 MHz with up to 6 MW of power and a toroidal magnetic field B_T of 3.7 T, leading to central ICRF power deposition; the plasma current I_p was either 3.3 or 3.7 MA (Refs. 13, 17, and 28). The fusion reactivity between ICRF-heated suprathreshold deuterons and thermal tritons is maximized at an average deuterium temperature close to 120 keV, the energy at which the D-T fusion rate peaks. This was achieved by varying the central density in the range 3.3 to $5.0 \times 10^{19} \text{ m}^{-3}$ and the deuterium concentration in the range 9 to 22%. The best results were obtained with a D:T ratio of 9:91 and a density of $5 \times 10^{19} \text{ m}^{-3}$ and launching 6 MW of ICRF power into the machine. A figure of merit $Q = P_{fus}/(P_{RF} + P_{OH})$ of 0.22 was sustained over 2.7 s, i.e., three energy replacement times, this duration of the ICRF pulse being dictated mainly by neutron economy and the length of the toroidal magnetic field’s flattop; P_{fus} , P_{RF} , and P_{OH} are the fusion power, the ICRF power launched, and the ohmic power, respectively, and P_{fus} was 1.66 MW while the maximal fusion rate reached $5.9 \times 10^{17}/\text{s}$. A confinement time of 0.87 s corresponds to an ELMy H-mode quality factor of 0.9, sufficient to reach ignition in ITER.

Over the years, different scaling laws have been used to characterize the confinement of tokamak discharges. At the time of the 1997 D-T experimental campaign, the scaling³¹

$$\tau_{97} = 0.029 I_p^{0.90} B_T^{0.20} P^{-0.66} M^{0.20} R_o^{2.03} N_{19}^{0.40} \varepsilon^{0.19} \kappa^{0.92}$$

was commonly preferred; here, I_p is the current in MA, B_T the magnetic field strength in T, P the auxiliary power in MW, M the effective atomic mass number, R_o the major radius in m, N_{19} the density in 10^{19} m^{-3} , ε the aspect ratio, and κ the plasma elongation. For typical parameters of the JET discharges, this expression constitutes a 20 to 25% reduction of the τ of the currently favored ELMy H-mode scaling law,

$$\tau_{H98(y2)} = 0.0562 I_p^{0.93} B_T^{0.15} P^{-0.69} M^{0.19} R_o^{1.97} \times N_{19}^{0.41} \varepsilon^{0.58} \kappa^{0.78} .$$

In Fig. 1, the neutron energy count spectra integrated over the ICRF pulse are shown, with a fit using a bi-Maxwellian distribution. For three shots with D concen-

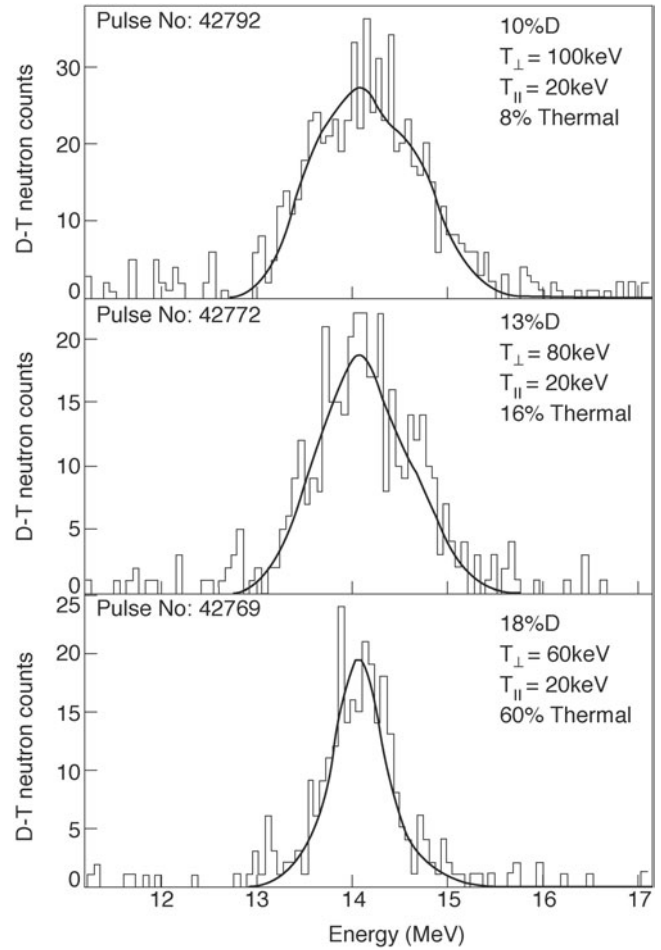


Fig. 1. Neutron energy spectra for (D)T ICRF heating Doppler broadened by the velocity of the deuterons; $P_{RF} \sim 5$ MW. The solid curves are best fits to the data of a combination of suprathreshold and thermal components.¹³

trations of 10, 13, and 18% respectively, the best fit is obtained for the perpendicular and parallel temperatures given in the right upper corner of the figures. At the lower concentration suprathreshold fusion reactions dominate (whereas the thermal ones account for only 8% of the yield). The thermal reactions become dominant at the higher concentrations.

To determine the deuterium concentration that maximizes the fusion reactivity, the deuterium was varied from 9 to 22% of the total ion density. The highest yield was observed at 9%, but the highest temperature and most robust ion heating were obtained at 18%. In shot 42769 a central ion temperature of 10.5 keV with a central electron temperature of 8.3 keV was obtained, for a density of $3.4 \times 10^{19} \text{ m}^{-3}$ and an ICRF power of 4.8 MW.

Recent measurement of the 14-MeV neutron spectrum using the magnetic proton recoil³² neutron spectrometer indicate that a strong suprathreshold deuteron

population was formed in the plasma with tail temperatures in the range from 90 up to 140 keV. These spectra were analyzed with a model that describes the observed neutron spectrum in terms of a bulk plus high-energy component. These show that the bulk ion temperature increases from 5.5 to 9 keV when the deuterium concentration goes from 13 to 18% and at the same time also the intensity of the bulk component relative to the high-energy one goes from 20% up to 80%. This is a clear indication of an effective bulk ion heating favored at higher deuterium concentration.

PION code calculations overestimate the neutron emission for these discharges at high deuterium fractions.¹³ To reproduce the observed neutron rate, it was necessary to artificially reduce the power in the fast wave to 40% of the input power. In Ref. 13 it was speculated that the missing power might take another route and go directly to the thermal ions. Neutron spectroscopy shows that the lack in energy density in the suprathermal ion component appears as an excess in the bulk part, resulting in a higher bulk temperature.³³ Suggested mechanisms are mode conversion to an ion Bernstein wave with subsequent damping on thermal ions or absorption of the fast wave by fully stripped impurity ions, which through collisional processes would produce bulk ion heating.

Because the fundamental cyclotron layer of any fully stripped impurity ion has a Z/A of roughly $\frac{1}{2}$, any D-heating scheme is bound to suffer from spurious impurity ICRF absorption. Impurity ions—such as Be—present in future reactor plasmas may thus parasitically absorb some of the launched ICRF power. This can be as much as several tens of percent of the ICRF power and contribute indirectly, because of the large impurity mass, also to bulk ion heating.

II.D.1.a.ii. Tritium Second-Harmonic Heating and ^3He Minority Heating. Tritium second-harmonic and ^3He minority heating are competing ICRF heating mechanisms since their respective cyclotron resonances coincide. A small fraction of ^3He has a major impact on the fusion performance of D-T plasmas. Second-harmonic tritium absorption relies on finite Larmor radius effects and is weaker at low ICRF power levels and/or when the bulk ions are not very energetic.

The discharge in which no ^3He was injected has a fusion yield of $1.5 \times 10^{16}/\text{s}$ for 6 MW of ICRF power, whereas the discharge with a ^3He puff prior to the application of the ICRF heating resulting in a concentration $N_{^3\text{He}}/N_e$ of about 4%, has a yield of $6.5 \times 10^{16}/\text{s}$, four times larger. Further increasing the concentration did not result in further improved performance. Both discharges had D:T = 10:90, $I_p = 3$ MA, and $B_T = 3.4$ T and were heated using ICRF heating at 34 MHz. The higher reactivity is due to the higher ion temperature. The different behaviors can clearly be summarized through the respective H-mode factors: $H_{97} = 1.1$ with ^3He and merely 0.75 without it. Part of the poor performance of the $\omega = 2\Omega_T$

case is due to the very high energy of the heated T, since second-harmonic heating is accelerating a tiny fraction of the tritons to very high energies: It is estimated that about 20% of the input power is lost due to those very energetic (MeV) tritons with massively wide orbits intersecting the limiters, and the wide orbits of the tritons broaden the collisional heating profile, reducing the global confinement. Second-harmonic heating accelerates particles well above the critical energy and thus yields electron rather than ion heating (e.g., see Fig. 11 in Ref. 13). It requires careful tuning (e.g., by adding ^3He to the mixture) to reduce this indirect electron heating to a minimum.

Optimized conditions were reached in a 45:55 D:T mixture with 10% of ^3He , $I_p = 3.3$ MA, and $B_T = 3.7$ T while heating the tritons and ^3He centrally with 8.7 MW at 37 MHz. Some key quantities of this optimal discharge are plotted in Fig. 2. The discharge is characterized by monster sawteeth,⁷ an H-mode that sets in when the ICRF reaches a power level of about 5 MW, and an H-mode factor reaching 0.95 prior to the first diagnostic beam blip. The values obtained would bring ITER close to ignition.

It is worthwhile to note that the JET ^3He results differ from the high-temperature TFTR supershots, in

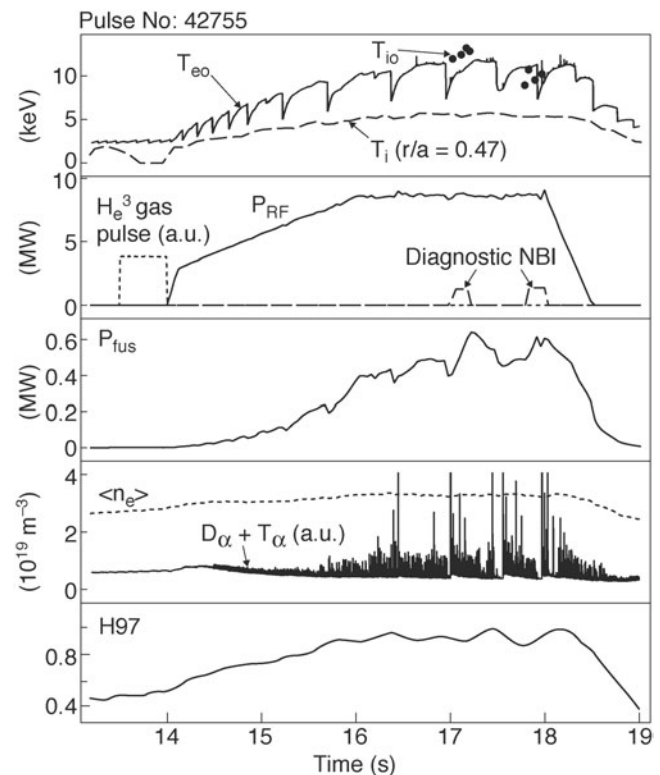


Fig. 2. Parameters of the ^3He minority ICRF discharge that generated central ion temperatures up to 13 keV. This plasma had 10% ^3He concentration, $I_p = 3.3$ MA, and $B_T = 3.7$ T (Ref. 13).

which—due to the high ion beta and the low ^3He concentration—the ICRF power was mainly absorbed by the tritons.^{34–36} In JET, an attempt was made to optimize the neutron yield in the second-harmonic tritium heating scheme in absence of ^3He , but optimal ICRF performance required working at densities so high that the performance was hampered by sawteeth.

Although the second-harmonic T heating scheme would produce mainly bulk ion heating in ITER (Ref. 37), the scheme performs differently on JET, producing highly energetic tails. These energetic tritium tails excite toroidal Alfvén eigenmodes, which were not observed with either deuterium or ^3He heating.¹³ This can be made plausible by noting that the slowing down time is longer for tritons than for deuterons and ^3He . The trapped fast tritons attain velocities that are high enough for tritons to be in precession resonance with the Alfvén eigenmodes.

Based on the experimental evidence on JET, the potential of the addition of a small minority of ^3He to enhance the D-T fusion rate was theoretically examined for ITER shortly after the D-T campaign.^{37,38} Whereas both D fundamental majority heating and second-harmonic T heating were found to be promising, the (^3He)-D-T combined scenario of fundamental cyclotron ^3He and second-harmonic T heating was seen to offer by far the best perspectives in terms of ion heating in ITER. The fast ion energy content is kept low due to the mass of the ^3He minority ions. Provided an antenna is designed to favor the optimal toroidal mode numbers, both heating (dipole phasing) and noninductive current drive ($\pm\pi/2$ phasing) can be realized efficiently in ITER with ICRF.

II.D.1.a.iii. Tritium Minority Heating. Tritium minority heating is a truly challenging ICRF heating scheme in JET (e.g., see Ref. 13): It requires the highest possible magnetic field values (3.9 T) and the lowest possible ICRF driver frequency, 23 MHz. Even under these extreme circumstances, the absorption layer is 0.4 m on the HFS of the magnetic axis. Compared to 37 MHz, the antenna loading drops by a factor of 2 to 0.7 Ω . The power levels were 2 MW at best. This proved insufficient to go into H-mode. The maximal reaction rate obtained ($1.5 \times 10^{16}/\text{s}$ in shot 43057) is 20 times higher than the thermal rate compatible with the ion temperature and density profiles obtained and is, therefore, due to ICRF-heated tritons fusing with thermal deuterons.

Together with results obtained on TFTR, the JET D-T campaign provided a unique opportunity for validating the performance of the ICRF scenarios foreseen for reactor plasmas. It has been shown in both machines that bulk ion heating can be achieved and that schemes have to and can be optimized to minimize the power to the electrons. In the TFTR experiments NBI was a key ingredient to produce the hot-ion mode that ensured that the rf waves predominantly heated the ions. In JET the

potential of rf heating to heat reactor-relevant plasmas in the absence of NBI was successfully tested. Adding a sufficient amount of ^3He in the second-harmonic heating scenario avoids the formation of high-energy tails, which would lead to less desirable indirect electron heating. The physics picture seems to be consistent with what was expected from modeling.^{30,39} The good agreement between experimental and model-produced data gives confidence in the predictions for the performance of the next-step machine.

II.D.1.b. Trace Tritium Experiments in 2003. In 2003, a “trace tritium” campaign was organized at JET to explore a number of specific tritium-related aspects, one of which was the tritium minority heating scheme.^{15,40} This scheme was briefly studied in the previous tritium campaign at JET (using concentrations $\sim 5\%$) as well as on TFTR (using concentrations up to 20%). Since it aims at heating one of the fusion fuel ion species, it is a possible candidate for providing ICRF heating to future reactor plasmas. But since this scenario lies outside the planned ICRF system frequency range for ITER (40 to 55 MHz) and in view of the technical difficulties to design wide-band ICRF antennas, including this scheme in the list of desired ICRF heating scenarios for ITER would have to be strongly motivated. Hence, the need for a study of its potential.

Tritons were usually brought into the machine via gas puffs (yielding concentrations $\sim 3\%$), but occasionally a tritium beam was adopted. From neutron emission data and gamma ray spectra measurements,⁴¹ it could be inferred that ICRF-driven T tails of 80 to 120 keV were formed.⁴² Since these energies are close to the energy at which the D-T fusion reaction rate peaks, the neutron yield was increased by three orders of magnitude during the ICRF phase of the discharge. The neutron yield is dominated by 14-MeV suprathermal emission up to $2.9 \times 10^{16}/\text{s}$. Due to the modest energies of the T tails, the T heating also contributed indirectly to bulk ion heating (the critical energy was about 80 keV for these shots), while at the same time good direct electron heating was observed. The experimental data were cross-checked with the SELFO code⁴³ against theoretical findings. Good agreement was found between the HFS peaking of the two-dimensional (2-D) neutron emissivity profile (in between the magnetic axis and the tritium cyclotron layer at $R = 2.5$ m) and the corresponding fast triton midplane density (Fig. 3); the peaking is the result of barely passing tritons, while the signature of fast tritons with trapped orbits and turning points near the T cyclotron layer is observed as well. The SELFO simulations confirmed earlier predictions that the impurities are capable of absorbing non-negligible fractions of the ICRF power. D absorption near the edge was further identified—and confirmed experimentally via a neutral particle analyzer (NPA)—as a competing mechanism.

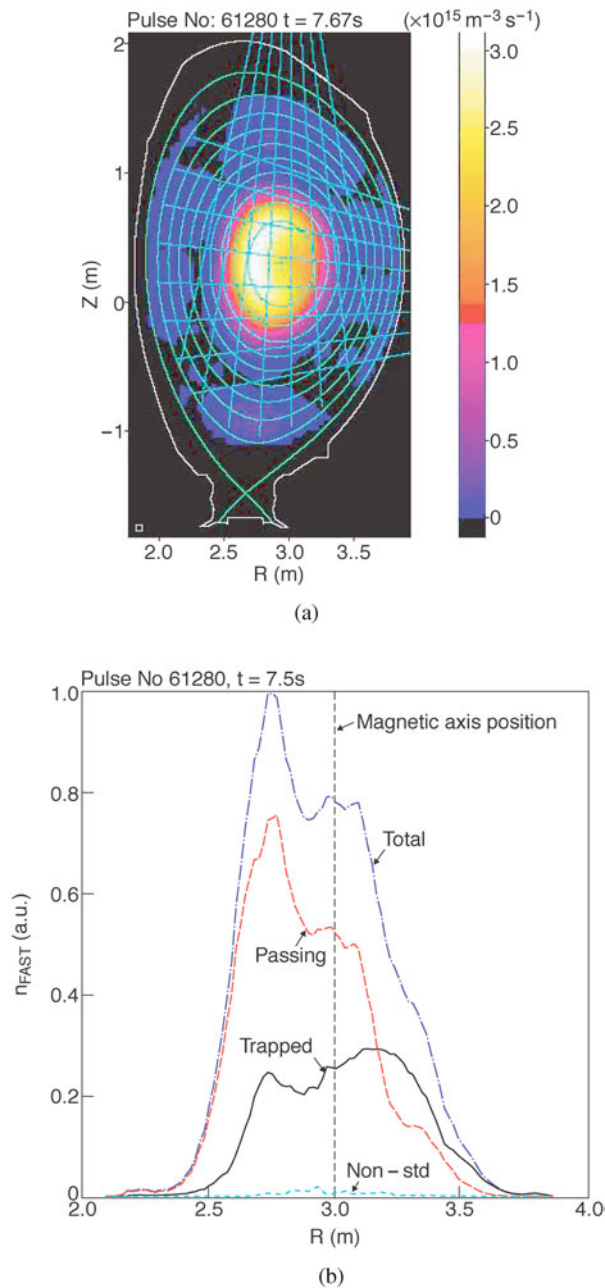


Fig. 3. (a) D-T neutron emissivity profile at $t = 7.7$ s for T(D) ICRF heating (dipole phasing, 23 MHz). (b) Fast ($E > 50$ keV) triton midplane density simulated with the SELFO code for the same discharge (61280). The majority of D-T neutrons originate from passing tritons. Their higher density on the HFS of the magnetic axis is due to the longer time spent there and is in good agreement with the observed neutron profile.¹⁵

The phasing of the antenna significantly impacts on the discharge. Counter-current ($-\pi/2$ phasing) wave launch yields slightly higher ion and electron temperatures but produces 20% fewer neutrons than co-current

($+\pi/2$) launch, an observation in line with the usual “pinch effect” interpretation of inward or outward ICRF-induced radial transport of the ICRF-heated ions (e.g., see Ref. 40 and the references therein), further discussed in Sec. II.E.4.b.

Neutron emission spectroscopy provided evidence of toroidal rotation of fast tritons at a speed of about 300 km/s for $\pi/2$ phasings, with a change in direction from being co-current with the plasma for $+\pi/2$ to being counter-current for $-\pi/2$. Compared to the speed observed for a symmetric “dipole” wave spectrum (π phasing), $+57 \pm 41$ km/s, this difference is statistically significant.⁴⁴

A few pulses were dedicated to second-harmonic heating of tritium at low concentration.¹⁵ At higher concentrations this is the reference ICRF heating scenario for ITER and was examined during the TFTR (Ref. 34) and JET (Ref. 13) D-T campaigns. In the trace tritium campaign, fast tritons with energies above 700 keV were observed, but the experimental analysis turned out non-trivial because of the competing fundamental cyclotron absorption of residual ^3He . Second-harmonic heating of tritium, relying on finite Larmor radius effects, is not strong enough relative to the competing absorption mechanisms at the low concentrations examined.

II.D.1.c. Neutron Production due to Reactions Between ICRF-Accelerated Protons with Tritium. In addition to the (intended) D-T, D-D, and D- ^3He reactions, other nuclear reactions can take place in magnetically confined fusion plasmas. Some of these reactions require high energies that can be reached only with ICRF heating. One example is the endothermic neutron-producing p-T reaction between protons and tritons with a large cross section above 1 MeV. In ICRF-heated T-rich plasmas during the 1997 JET D-T campaign, excess neutron rates up to 40% above those expected were observed.⁴⁵ This point was readdressed in the trace T campaign to highlight its origin. Also in those plasmas with reduced T content, the excess was identified.⁴⁶

The experiments were performed in deuterium plasmas with a small fraction of 5 to 8% of hydrogen into which 3 to 5 mg of T was puffed. The magnetic field was 3.45 T and the plasma current 1.8 MA, with a fairly low central density of $2 \times 10^{19}/\text{m}^3$ to favor the production of highly energetic proton tails; the choice of $f = 51$ MHz places the H cyclotron layer at $R = 3.12$ m, close to the magnetic axis. To improve fast-ion confinement, $+\pi/2$ phasing was used (inducing a radially inward ICRF-induced pinch); typically, 6 to 7 MW of ICRF power was launched into the plasma and both monochromatic and polychromatic excitations were applied.

The highly energetic proton tail was identified via nuclear gamma-ray measurements and by high-energy NPA measurements. Polychromatic excitation tends to spread out the ICRF power and to result in less energetic tails. This was experimentally confirmed. The neutron yield from the p-T reaction increases with background

tritium density and tail temperature; the experimentally observed excess neutron yield seems to follow this scaling.

The excess neutron fraction was evaluated for a number of other pulses in the trace tritium campaign. The p-T neutron excess is solely observed in ICRF-heated pulses, NBI not being capable of reaching the required temperatures. When the (diagnostic) neutral beam is on, the D-T reactions are abundant and make the detection of the p-T-related excess difficult. In that case the total and D-T + D-D related yields essentially agree.

II.D.2. Mode Conversion in (^3He)-D and (^3He)- ^4He Plasmas

ICRF mode conversion with ^3He ions in D or ^4He plasmas has been systematically investigated in order to develop efficient localized on-axis and off-axis bulk electron heating. The fast wave (FW) launched from the antennas can indeed be mode-converted to short-wavelength waves at the ion-ion hybrid confluence/cutoff pair, referred as mode conversion layer R_{MC} , on the HFS of the fundamental ^3He ion cyclotron resonance layer $R_{RES}(^3\text{He})$. One or more short-wavelength waves, which can be of different nature depending on the scenario (i.e., Alfvén waves, ion Bernstein waves, electromagnetic ion cyclotron waves), can be excited and will damp strongly by ELD and TTMP on the bulk electron on the short timescale of the electron-electron collisions.

In these experiments, reported in detail in Ref. 47, B_T was in the range of 2.4 to 3.7 T and I_p in the range of 1.3 to 2 MA and 6 MW of ICRF power were applied at an ICRF frequency of 33 or 37 MHz. $R_{RES}(^3\text{He})$ was consequently located centrally whereas the fundamental D (or ^4He) ion cyclotron layer $R_{RES}(\text{D})$ was far off-axis on the HFS. As the ^3He concentration [^3He] was scanned from 1 to 2% up to 20%, a reproducible transition from the minority heating to the mode conversion regime was observed. Peaks in the gamma-ray energy spectra due to fast ^3He ions with energy above 1 MeV reacting with ^9Be and ^{12}C impurities ions decreased and finally disappeared as [^3He] was increased. The electron temperature response to the ICRF power modulation became prompt, consistent with stronger direct electron heating. Electron power deposition profiles were deduced from fast Fourier transform (FFT) and break-in-slope (BIS) analysis⁴⁸ performed for pulses with different ^3He flow rates, as represented in Fig. 4. With increasing ^3He flow rate, a transition from a rather broad central to a more peaked off-axis direct electron heating was observed. These results were consistent with the increase in the mode conversion power fraction and the movement of R_{MC} to the HFS farther away from $R_{RES}(^3\text{He})$ as the ^3He concentration was increased. For the pulses represented on Fig. 4, the integrated electron power deposition over the plasma volume increased from about 15% of the launched power to 70% for pulse 54249 with [^3He] \sim 10%. Note that similar analysis of shots performed with the mode con-

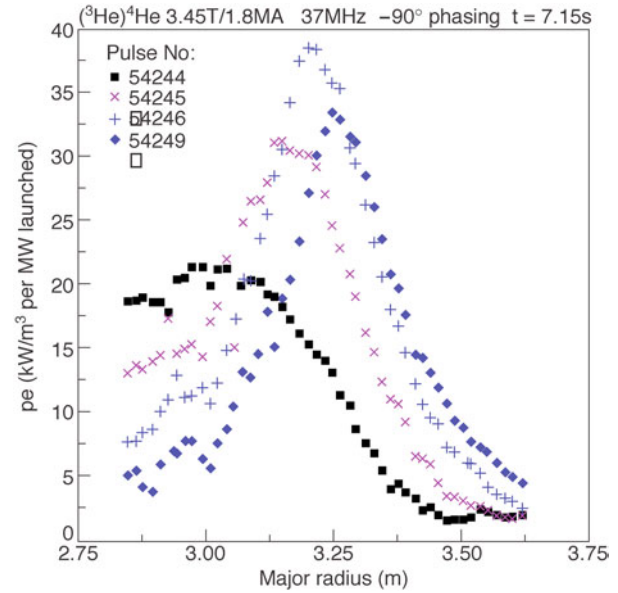


Fig. 4. Direct electron heating profiles from BIS analysis of T_e data for four ^4He pulses different only in their ^3He gas flows: 0.8×10^{21} el/s in pulse 54244, 1.3×10^{21} el/s in pulse 54245, 1.9×10^{21} el/s in pulse 54246, and 2.4×10^{21} el/s in pulse 54249. Note that the electron power deposition from mode conversion layer on the HFS is seen on the same flux surface on the LFS. The magnetic axis is situated at ~ 2.95 m (Ref. 45).

version layer more centrally located [i.e., 3.45 T, 33 MHz, $R_{RES}(^3\text{He}) \sim 3.2$ m, and $R_{MC} \sim 3$ and 2.7 m] had shown that the maximal direct electron power density was obtained for [^3He] in the range of 12 to 20%. The best performances obtained with the mode conversion layer maintained in the plasma center required tuning of ^3He flow injection during the main heating phase in order to keep [^3He] constant. In that case, central electron temperature up to 8 keV was obtained with 5 MW of ICRF. The influence of the position of R_{MC} on the global confinement in L-mode mode conversion shots is reported in Ref. 49.

Finally, some parasitic absorption of the ICRF power by the energetic D ions (135 keV) coming from the diagnostic beams was observed. It was found that if the resonance condition is fulfilled for an NBI deuteron in the vicinity of the ICRF mode conversion layer, due to large Doppler shift, strong wave-particle interaction can occur in spite of the high D concentration. This effect was found to be maximized for higher parallel wave vector component k_{\parallel} obtained with antenna dipole phasing and minimized for -90 -deg antenna dipole phasing, which gives lower k_{\parallel} and counter-current propagating waves (in the direction opposite that of the D beam's injection).

This first set of experiments on the mode conversion regime highlighted the necessity to control more efficiently the ^3He concentration throughout the pulse.

Consequently, techniques have been developed during the past few years to control $[^3\text{He}]$ in real time using the JET real-time central controller, which links a measurement of $[^3\text{He}]$ to the opening of the gas injection valve.⁵⁰ Furthermore, mode conversion is now routinely used in L-mode, H-mode, and optimized shear plasma as a tool for transport analysis (see Sec. II.D.4).

II.D.3. Inverted Minority Heating and Mode Conversion Scenario in (^3He)-H and (D)-H Plasmas

The ICRF scenarios foreseen for the nonactivated phase of ITER in H plasmas,^{38,51} rely on the heating of a minority of ^3He or D ions. In these so-called “inverted scenarios,” in which the ion minority species has a smaller charge-to-mass ratio than the ion majority species, i.e., $Z_{\min}/A_{\min} < Z_{\text{maj}}/A_{\text{maj}}$, the FW dispersion relation places the mode conversion layer R_{MC} between the ICRF antenna and the minority ion cyclotron resonance layer R_{RES} . The FW absorption in such conditions has been investigated in detail for the first time^{14,15,52} with different concentrations of ^3He ions or D ions.

The minority concentration $[^3\text{He}]$ of ^3He ions in H plasma was varied from 1 to 10%, with up to 5 MW of ICRF power and the minority resonance layer $R_{RES}(^3\text{He})$ at the plasma center. For $[^3\text{He}]$ up to 2%, efficient heating of the minority ^3He has been observed. The energy of the tail was influenced by the choice of antenna phasing, as shown in Fig. 5. The higher T_e and R_{NT} [from the $^9\text{Be}(^3\text{He},n)^{11}\text{C}$ reaction for energies above 0.9 MeV] obtained with +90-deg phasing were consistent with the expected wave-induced pinch effect^{53,54} (see Sec. II.E.4.b). A maximum T_e of 6.2 keV was obtained. As $[^3\text{He}]$ was increased above 2%, a transition from the minority heating to the mode conversion regime was observed. Different signals confirm this transition from heating of the minority tail to a direct heating of the electrons. The T_e response to ICRF power modulation becomes very prompt, and the fast ^3He ion population, detected from the γ -ray emissions, which requires ^3He ions with energy above 0.9 MeV, gradually disappears (see Fig. 6, showing discharges with increasing $[^3\text{He}]$ concentrations). With R_{MC} in the plasma center and dipole phasing, efficient direct electron heating produced T_e of 8 keV with 5 MW of ICRF power. Direct electron power deposition at the mode conversion layer was confirmed by FFT and BIS analysis⁴⁸ of the T_e response to ICRF power modulation.

A second set of experiments used minority heating of D ions in an H plasma. In contrast to the similar experiments with ^3He as minority, no D fast ions were detected, even at the lowest D concentrations, either by the NPA or from the γ -ray emissions. No neutrons were produced and a maximum electron temperature of only around 3 keV was obtained. Direct electron heating was observed on the LFS. The reason is the presence of 2 to 3%

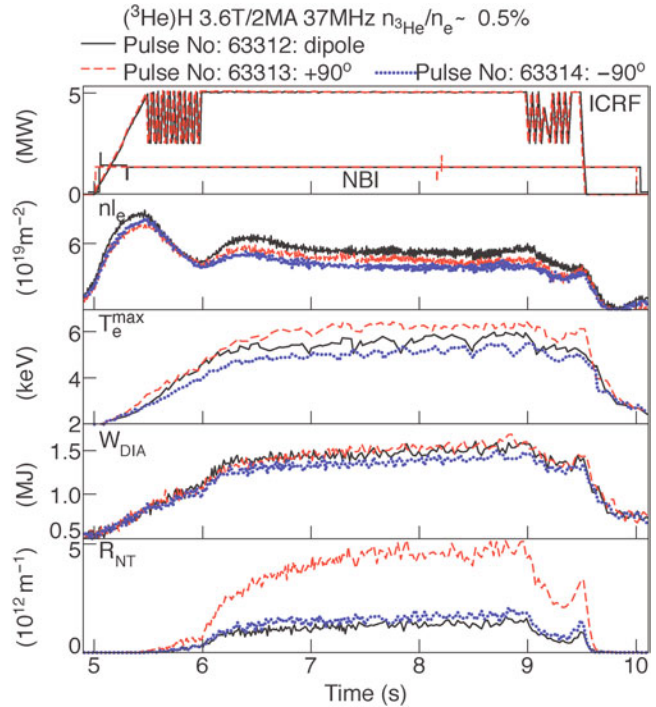


Fig. 5. Evolution of the ICRF and NBI power (H beams), central line integrated electron density, maximum electron temperature, plasma diamagnetic stored energy, and neutron rate for $[^3\text{He}] \sim 0.5\%$. From Ref. 52.

of carbon C^{6+} , which has the same Z/A ratio as the D ions and influences the FW propagation in the same way as a higher equivalent D concentration, leading directly into the mode conversion regime (see Fig. 7). Concentrations of C^{6+} as low as 0.5% suffice to prevent efficient absorption on the D minority at $R_{RES}(\text{D})$. This effect virtually rules out the D minority heating scenario for the nonactive phase of ITER in H plasmas, leaving ^3He minority heating as the only viable choice.

II.D.4. Minority Heating in (H)-D and (^3He)-D Plasmas

II.D.4.a. Polychromatic Heating. The scenario for increasing the ion temperature and maximizing the D-D reactivity is one in which a significant fraction of the power is directly absorbed by the deuterons but for which the deuterium tail is not too energetic.^{5,16,29} Working at high densities is instrumental in this respect since it curtails tail formation and favors bulk ion heating. A set of approximate but practical expressions to estimate the relative power densities due to H fundamental and D second-harmonic heating and the power density level required to guarantee dominant indirect D heating has been proposed.²⁹ This leads to a simple expression for the ICRF power level under which one should stay in JET in order to guarantee that ion heating dominates electron heating.

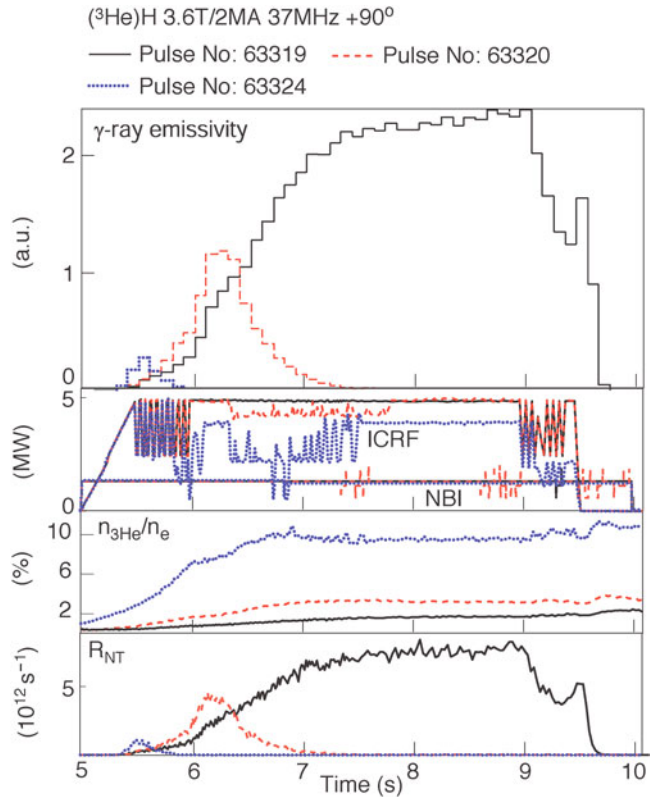


Fig. 6. Evolution of the γ -ray emissivity, ICRF and NBI power, ${}^3\text{He}$ concentration, and neutron rate for pulses 63319, 63320, and 63324. From Ref. 52.

Above this threshold power, polychromatic rather than monochromatic excitation is advised.

Polychromatic excitation—spreading out the power deposition due to the simultaneous use of several different frequencies of the ICRF waves—reduces the average energy of the resonating ions and increases the bulk ion-heating fraction. This method has been extensively investigated in JET (Refs. 5, 16, 29, and 55). It has been found to be quite effective for reducing the ratio of the electron over the ion temperature (T_e/T_i) (note that depositing power more off-axis can potentially influence the energy confinement). This is illustrated in Fig. 8, which shows the temperature profiles for two L-mode discharges with an ICRF power of 3 MW. In one, a single central resonance was used, whereas there were three resonance locations in the other (3.0, 3.1, and 3.4 m). The power transferred to the electrons for these discharges has been simulated with the SELFO code⁴³ and shows a reduction in the electron heating power, consistent with the experimental observation.

II.D.4.b. ICRF-Induced Spatial Transport. The interaction of resonating ions with ICRF waves not only leads to a distortion of their velocity space distribution function but also induces their spatial transport. This

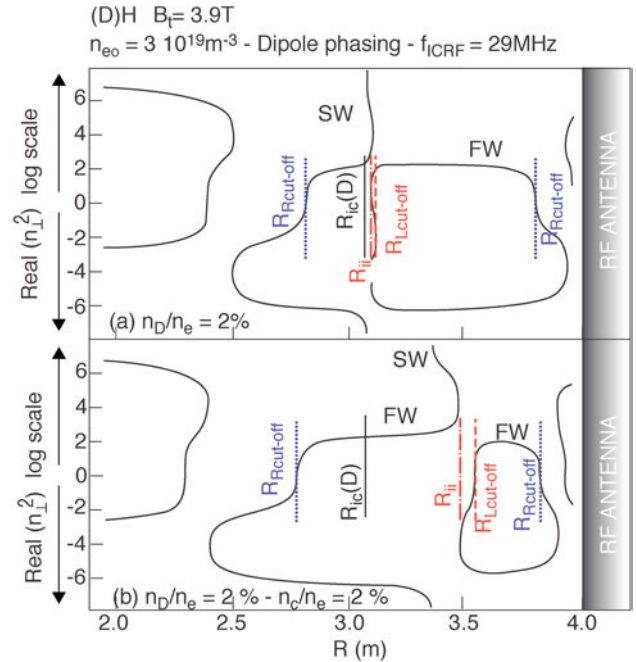


Fig. 7. Real part of the square of the perpendicular refractive index obtained from the resolution of the cold plasma dispersion relation. Fast wave (FW) and slow wave (SW) branches are represented. The following radial locations are indicated: FW left cutoff $R_{Lcut-off}$, FW right cutoff $R_{Rcut-off}$, FW resonance R_{ii} , and D cyclotron resonance R_{ic} . Two cases are plotted: (a) with 2% of D and (b) with 2% of C and 2% of D. From Ref. 52.

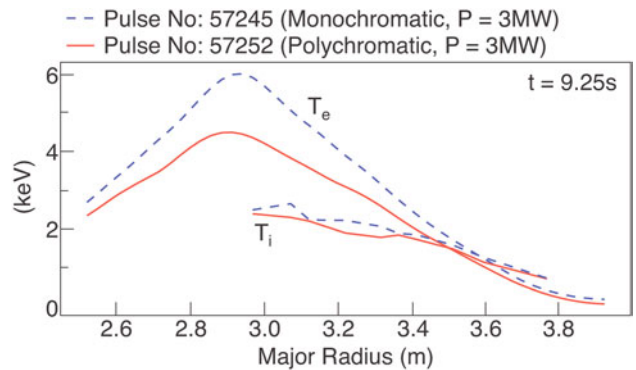


Fig. 8. Measured ion and electron temperature profiles for two discharges with 3 MW of ICRF power: pulse 57245, with single-frequency central resonance, and pulse 57252, with three frequencies with two resonances on the LFS of the magnetic axis. From Ref. 55.

is due to a fundamental property of wave-particle interaction in a torus. A resonating ion that absorbs a wave quantum gains an energy $\Delta E = \hbar\omega$. However, if the wave propagates toroidally with a wave vector k_ϕ , the

wave quantum also carries toroidal momentum. As a result the particle's toroidal angular momentum P_φ is changed by $\Delta P_\varphi = R\hbar k_\varphi = N_\varphi \hbar$. Thus, the change in energy can be related to change in toroidal angular momentum $\Delta P_\varphi = (N_\varphi/\omega)\Delta E$. The toroidal angular momentum for a particle is given by $P_\varphi = mRv_\varphi + Ze\psi/2\pi$, where ψ is the poloidal flux (a flux surface label). Consequently, for a trapped particle, which has $v_\varphi = 0$ at the turning point, the change of P_φ at a cyclotron resonance, $\omega - k_\parallel v_\parallel = n\omega_{ci}$, along its orbit gives rise to a radial change of the turning point position. Initially, one could think that for a symmetric toroidal mode number spectrum the changes in P_φ would cancel. However, the cyclotron resonances do not occur at the same position along the orbit of a resonating ion for N_φ 's with opposite signs. Assuming decorrelation between the changes at the two resonance locations, the process then leads to diffusion of the resonating ions in the phase space direction P_φ . The practical consequence of this was first analyzed in Ref. 56, and some tentative signs were reported in Ref. 57. However, as indicated in Ref. 58, the effect should be significantly more pronounced for waves launched with an asymmetrical toroidal mode number

spectra. Then, the change in P_φ leads to a drift of the turning points of resonating trapped ions as they gain energy. The drift is outward in minor radius for waves propagating in the toroidal direction counter to the plasma current and inward for co-current propagating waves. The first experimental evidence for this ICRF-induced drift (or pinch effect in the case of an inward drift) was reported in Ref. 53, where a number of quantities, such as TAE mode activity and sawteeth, related to the fast-ion pressure gradient were found to be strongly affected by the direction of propagation of the ICRF waves. In particular, the fast-ion-induced toroidal Alfvén eigenmode (TAE) activity increased significantly for co-current propagating waves, consistent with a peaking of the fast-ion pressure profile due to the ICRF-induced inward transport of the resonating ions. There were also indications that this effect could play a role for the triggering of internal transport barriers⁵⁹ (ITBs). The evidence reported in Ref. 53 was indirect. However, more direct measurements later became possible with the aid of tomographic reconstructions of gamma rays from the interaction of fast ions with beryllium and carbon impurities.⁵⁴ An example is shown in Fig. 9, which displays the

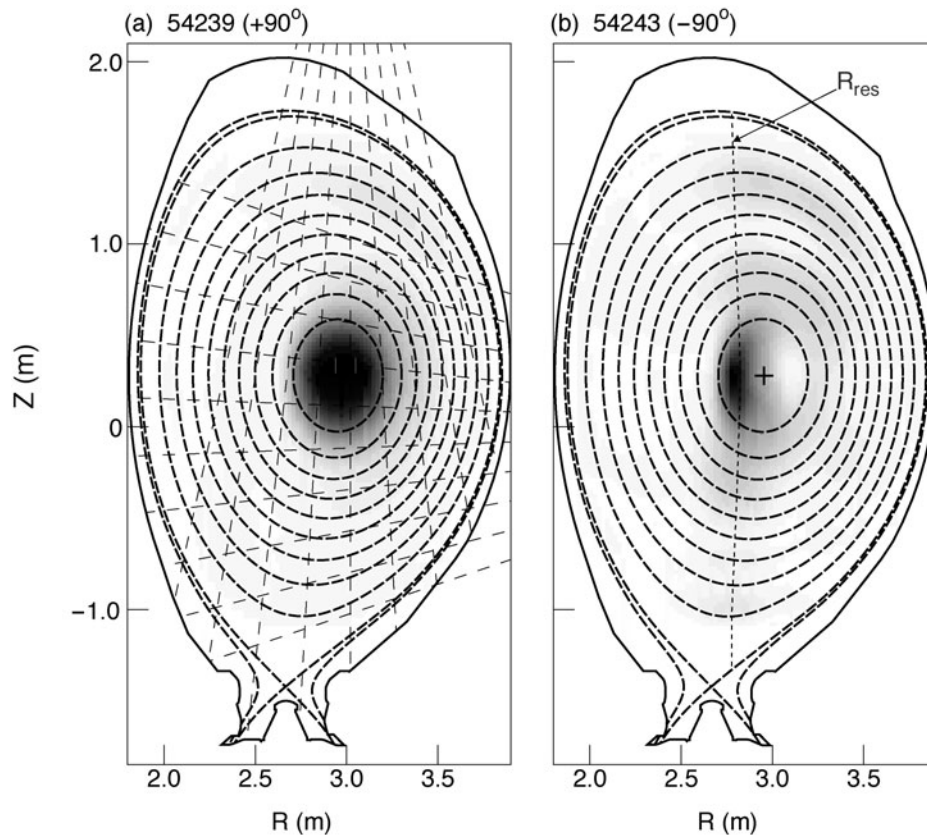


Fig. 9. Contour plots of the reconstructed γ -ray emission profile from reactions between ^3He minority ions and impurities (carbon and beryllium), normalized to the peak emissivity. The lines of sight of the neutron profile monitor are shown in (a) and the ICRF resonance location in (b). From Ref. 54.

reconstructed gamma rays due to the presence of fast resonating ^3He minority ions during (^3He)-D HFS ICRF heating for two discharges with directed waves; +90- and -90-deg phasings of the ICRF antennas give rise to waves propagating predominantly in the co-current and counter-current directions, respectively.

To interpret the figure, we need to consider the topology of the fast ions. With +90-deg phasing the turning points of the trapped ions, which are mostly close to the resonance layer $\omega = n\omega_{ci}$, should be driven inward almost vertically. When a turning point reaches the equatorial plane, the particle detraps into a co-passing orbit.⁶⁰ Since the affected ions tend to be very energetic, the resulting detrapped orbit is often passing in the potato regime.⁶¹ On the other hand, with counter-current propagating waves the turning points are driven outward and the ions stay trapped. Since a trapped ion spends most of its time close to the turning point, one would expect to see a gamma-ray emission concentrated around the resonance layer $\omega = n\omega_{ci}$ in the latter case, whereas with significant detrapping of resonating ions one should see a more symmetric emission during heating with an HFS resonance. This picture is consistent with the observations in Fig. 9. Thus, ICRF-induced spatial transport in the presence of waves with a toroidally asymmetric propagation is well established. The control offered by the phasing can be applied for different purposes, e.g., saw-tooth control (see Sec. II.E.1) and facilitating the triggering of ITBs (Ref. 59).

II.D.5. Second-Harmonic Minority Heating and Finite Larmor Radius Effect in (H)-D Plasmas

One of the principal ICRF heating schemes foreseen for ITER is second-harmonic heating of tritium $\omega \approx 2\omega_{cT}$. Since the wave absorption at the ion cyclotron resonance is a finite Larmor radius (FLR) effect, it is weak at low energies but increases strongly as the ratio of the ion Larmor radius, $\rho = v_{\perp}/\omega_{ci}$, to the perpendicular wavelength of the fast wave increases. However, when the ion Larmor radius further increases (corresponding typically to the MeV range), the absorption weakens again and effectively prevents particles from reaching higher velocities. To predict with confidence the performance of second-harmonic heating of T in ITER, it is important to have a good understanding of the resonant ion energy distribution.

Experiments have been performed with second-harmonic ICRF heating of hydrogen in deuterium plasmas to assess the role of FLR effects on the resonant ion distribution function.^{39,62} The distributions of ICRF-heated hydrogen ions have been experimentally measured with a high-energy NPA. By changing the electron density, the energy E^* , around which the wave-particle interaction becomes weak, is varied. The dependence of the ion distribution on E^* is observed for a number of discharges and FLR effects are clearly seen to affect the high-energy tail. Experiments have been analyzed with

the combination of ICRF modeling codes PION and FIDO, including FLR effects, and good agreement with measurements has been found. Figure 10 shows the measured and calculated distribution functions for three simulated discharges, including error estimates for the simulated distributions. The discharges were carried out at two different densities, leading to energies E^* of approximately 0.7 MeV in one and 1 MeV in the other two; the ICRF power was 2.9 MW in two of the discharges and 3.5 MW in the third. The higher power was designed so as to keep the total fast-ion energy content approximately constant when comparing the higher-density discharge to a lower-density one (the energy content was estimated as being $\sim P_{\text{ICRF}}t_s$, where t_s is the ion-electron slowing-down time). Two different powers at the same density were used to show that the measured E^* did not depend on the power.

It should be noted that a positive effect of this reduction of wave-particle interaction at the energy E^* caused by FLR effects is that the resonating ions are prevented from becoming too energetic, which can limit losses due to finite orbit width effects. Moreover, not only are FLR effects important for the distribution function itself, but they also have implications for the plasma response to

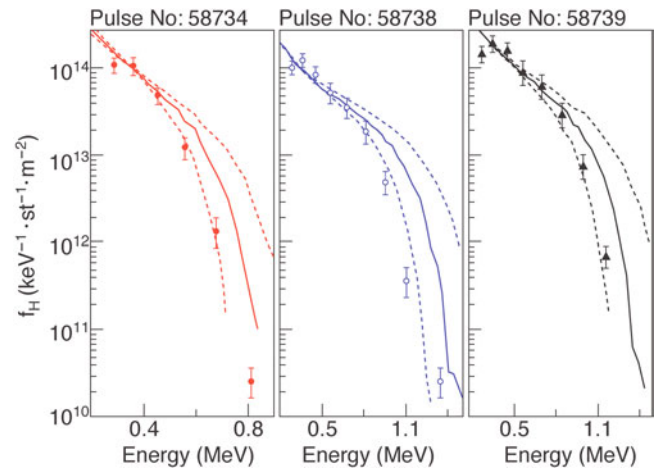


Fig. 10. High-energy parts of the resonant hydrogen distributions. Points with error bars are the NPA measurements, full lines are from the FIDO simulations, and dashed lines are the estimated errors for the simulations (due to uncertainty in plasma parameters). By comparing discharges 58738 (low power) and 58739 (high power), both of which have an estimated $E^* \sim 1$ MeV, one can see that the shape of the distribution is not different for different power levels. The number of energetic particles, however, is higher in the high-power pulse. Second, again as predicted by quasi-linear theory, the discharge with high density, 58734, with an estimated $E^* = 0.7$ MeV, has a tail that starts to fall rapidly at energy lower than that in 58738 even though the estimated fast-ion energy content is similar in the two discharges. From Ref. 62.

the waves. The results discussed here emphasize the importance of taking FLR effects into account to higher orders when the dielectric properties of the plasma are calculated.

II.E. ICRF Current Drive

With ICRF power being able to heat the electrons even at high density and to provide them with some additional momentum in the toroidal direction, it can also be used to drive current. This capability was investigated both for influencing the current profile and for driving net current.

II.E.1. Ion Cyclotron Current Drive for Sawtooth and Neoclassical Tearing Mode Control

Sawtooth oscillations might be beneficial in a reactor since they could remove the helium ash from the center of the plasma. On the other hand, the fast fusion born alpha particles are likely to induce sawteeth with long periods. Unfortunately, the crashes of such sawteeth can trigger neoclassical tearing modes (NTMs) by providing seed islands for the instability.^{63,64} Thus, to avoid triggering NTMs, it is of interest to develop methods to control the length of the sawtooth periods. One possibility is to affect the shear at the $q = 1$ surface, s_1 . If certain conditions are met, a sawtooth crash can be induced by increasing s_1 above a critical level, s_{1crit} , determined by the layer physics around the $q = 1$ surface (i.e., s_{1crit} depends on local parameters at the $q = 1$ surface only).⁶⁵ This method of sawtooth control has been demonstrated comprehensively at JET by the use of ion cyclotron current drive^{8,66–68} (ICCD). Moreover, it has been shown experimentally that in scenarios in which ICCD has been used to shorten the sawtooth period, the onset of NTMs could be prevented or delayed, as compared to discharges with otherwise similar parameters but without ICCD (Refs. 63 and 64). In one of the discharges in Fig. 11, the sawtooth period was kept short with the aid of ICCD, whereas in the other the ICRF waves were not tuned to provide short-period sawteeth. In the discharge without the shortened sawtooth periods, a (3,2) NTM was triggered at a $\beta_N \sim 1$. On the other hand, in the discharge with shortened sawteeth this value went up to almost 2 without any onset of NTMs.

Several ICCD scenarios have been used for sawtooth control. These include using minority ions resonating with the waves at their fundamental cyclotron frequencies^{8,66,68} and interaction at the second-harmonic ion cyclotron frequency.⁶⁷ Furthermore, both HFS and LFS resonances have been used successfully to control sawteeth.^{8,66–68} In one respect these experiments were not completely representative of the conditions expected in a reactor: The sawteeth were not stabilized by very energetic ions (in the MeV range), like the fusion-born alpha particles. To investigate if sawteeth with

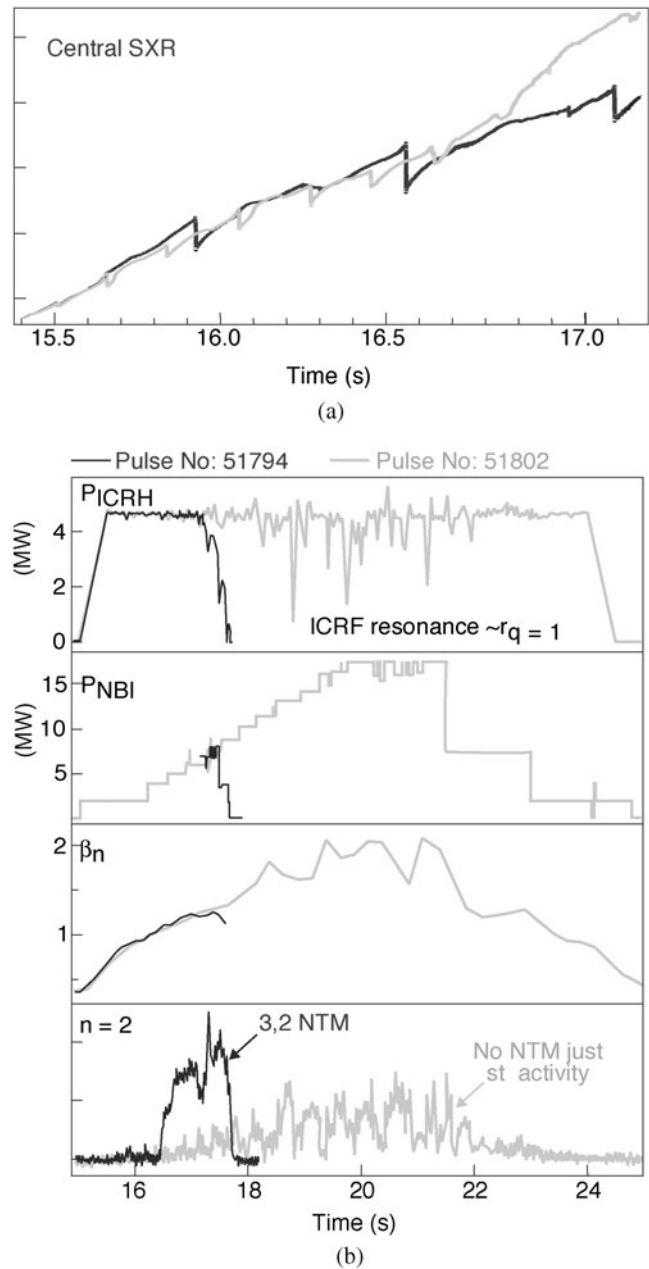


Fig. 11. In similar plasmas with $\beta_N \sim 1$, NTMs were found to be triggered after crashes of long sawteeth, whereas no triggering was observed in plasma in which ICCD had been tuned to produce short sawteeth. (a) Trace of soft X-ray emission and (b) normalized beta, β_N , and MHD signal for $n = 2$ modes. From Ref. 63.

long periods induced by fast ions in the MeV range could be destabilized by local current drive near the $q = 1$ surface, a number of experiments were carried out in which half of the available ICRF power in JET was used to create very energetic minority ions in the center of the plasma and the other half was used to

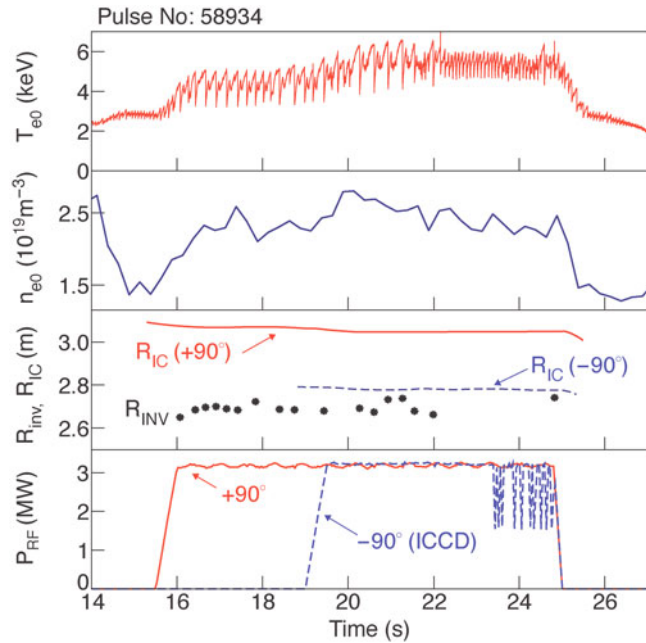


Fig. 12. Overview of discharge 58934, which demonstrated shortening of fast-ion-induced long sawtooth periods by minority ICCD. The traces (bottom to top) are ICRF power for $+90^\circ$ -deg central H resonance and -90° -deg power for minority ICCD with an H resonance on the HFS; major radius of the H cyclotron resonance for the -90° -deg ICCD and major radius of the sawtooth inversion radius; central electron density; and central electron temperature measured by electron cyclotron emission. From Ref. 69.

destabilize the concomitant long sawteeth by the application of ICCD (Ref. 69). The experiments were successful and provided strong evidence that long sawteeth, induced by fast ions, can be shortened by controlling s_1 . The results of an experiment demonstrating this point are shown in Fig. 12, where it can be seen that the conditions evolved for a short while after the switch-on of the ICCD power and before they became optimal for inducing short-period sawteeth. Detailed analysis of discharge 58934 with the SELFO code has shown that the applied ICCD indeed should have increased the shear at the $q = 1$ surface, consistent with the experimental observation and theoretical expectations.⁷⁰

II.E.2. Fast-Wave Current Drive

The demonstration of fast-wave current drive (FWCD) has turned out to be relatively difficult due to the low single pass absorption of the ICRF waves experienced in most of today's tokamaks. Owing to the weak direct electron absorption, parasitic mechanisms can often dominate even in scenarios with nominally dominant direct electron absorption. A number of mechanisms are

possible, including RF-sheath effects and cyclotron resonances of residual ion species. The first evidence for direct electron damping by ELD and TTMP on JET was reported in Ref. 71, and more dedicated experiments aimed at detecting fast-wave electron heating (FWEH) were presented in Ref. 72. In fact, it is much easier to detect FWEH than FWCD. In the former case symmetric antenna spectra peaking at relatively high parallel wave numbers (dipole phasing of the JET antennas) can be used, whereas current drive phasing typically peaks at parallel wave numbers about half those for dipole phasing. Since the direct electron absorption decreases rapidly with the parallel wave number at low to moderate electron temperatures, it has been hard to develop JET scenarios to demonstrate FWCD. Most of the work in the field of FWCD has been done in DIII-D (Refs. 73 and 74) and Tore Supra.⁷⁵ To improve the direct electron damping by increasing the electron temperature, FWCD experiments at JET have more recently been carried out in plasmas with electron transport barriers.⁷⁶ However, even under these conditions it was difficult to avoid parasitic absorption. In fact, it proved to be more difficult to damp significant wave power on the electrons via TTMP/ELD for current drive phasings than for dipole phasing even when the single-pass damping was similar,⁷⁶ indicating that rectified rf-sheet potentials were implicated in the parasitic absorption. The latter could be estimated in two ways:

1. by comparing discharges with different phasings in which similar temperatures and stored energies were achieved through variation of the ICRF power
2. by measuring the total energy escaping the plasma (radiated power from bolometers plus the power going to the divertor measured by thermocouples) and comparing it to the total input energy (ohmic plus auxiliary heating).

The difference between the latter two quantities represents the fraction of energy not absorbed within the plasma. Both estimates showed that a substantial fraction of the ICRF power could not be accounted for when current drive phasings were used. In addition to rectified rf-sheet potentials, orbit losses of fast residual ^3He ions accelerated by the ICRF waves could have played a role, but estimates based on simulations showed that it should have been a minor effect. Moreover, due to the high temperature, i.e., long current diffusion time, and the interplay with bootstrap current, it was quite difficult to change the central current density in plasmas with an electron transport barrier. Nevertheless, clear evidence of FWCD was seen.⁷⁶

II.F. ICRF Rotation

Plasma rotation plays an important role in tokamaks in various aspects: Shear in the toroidal rotation is an

essential factor in the formation of transport barriers, and rotation stabilizes resistive wall modes, allowing higher β to be achieved. On present machines, ICRF heating can be used to study plasmas with low momentum input such as will be expected, even with beams, in ITER.

In a number of machines (Refs. 77 through 80 and references therein), a substantial plasma rotation is observed despite little or no toroidal momentum input; a number of mechanisms have been postulated to explain this effect.⁸¹

The radial profile of the plasma rotation was measured on JET with the charge-exchange recombination spectroscopy diagnostic. The flexible ICRF system allows us to inject waves either with no net toroidal momentum or with some toroidal momentum, directed with or counter to the plasma current. The location of the wave absorption can be varied over the whole plasma cross section. This provides comprehensive information to compare the measurements with different theories.

Off-axis location of the resonance layer leads to an off-axis peaking of the toroidal rotation, in the codirection, independently of the direction of momentum input and whether the location of the resonance layer is on the HFS or LFS of the center.⁸⁰ This rules out theories that rely mostly on effects arising from the ICRF-driven fast ions to account for the ICRF-driven plasma rotation. Cen-

tral power deposition results in centrally peaked rotation profiles, whereas MHD modes can lead to strong braking of the plasma rotation and very flat rotation profiles.⁸⁰

Detailed comparison of discharges with co-injected and counterinjected central wave momentum did identify the toroidal rotation component due to the wave momentum, as shown in Fig. 13 (Ref. 82). The change in rotation induced by the wave, however, is found to be overlaid on an underlying mechanism, not yet accounted for by theory, giving rise to co-current rotation.

II.G. ICRF as a Tool

In addition to using the properties of the ICRF scenarios for heating and current drive and for investigating discharges with low momentum input, specific aspects of ICRF can also be used to provide powerful tools in a number of areas.

II.G.1. Alpha Tail Production

Acceleration of ^4He ions to MeV energies with ICRF was developed to simulate α particles, to study their effect in a quasi-steady-state plasma regime where heating by fast ^4He is the dominating heating process, and to test α diagnostics without the activation resulting from

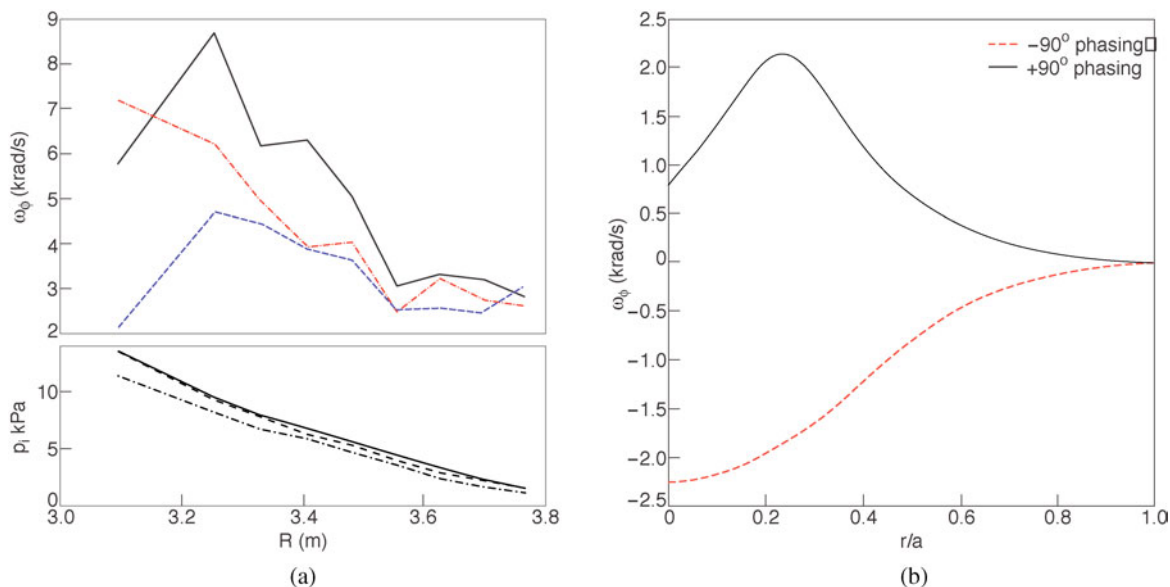


Fig. 13. (a) Carbon impurity rotation profiles and ion pressure profiles for (solid line) a discharge with 5.5-MW ICRF power in the co-current direction, (dashed line) a discharge with the same power in the counter-direction, and (dotted-dashed line) one in which 2 MW of co-current ICRF power was replaced by 2-MW LH power (which carries only 10% of the momentum of the co-current ICRF waves for equal power). The discharge with LH has somewhat lower ion pressure and lower stored energy than the two ICRF discharges. Therefore, one can conclude that the stronger rotation of the discharge with co-current ICRF power is not due to higher ion pressure or higher stored energy—otherwise, the discharge with LH would have rotated less than the discharge with counter-ICRF power. (b) The rotation profile resulting from inserting the fast-ion torque simulated by the SELFO code in the momentum diffusion equation. The difference in rotation profile between co-current and counter-current corresponds to the experimental value. The absolute values, however, do not.

the production of “real” α 's from the fusion reaction. This could be used, for example, in ITER in the nonactivated phase of operation.

The method developed on JET (Ref. 83) relies on third-harmonic heating $\omega = 3\omega_c$ of ^4He ions injected at high energy (120 keV) with the NBI. Third harmonic was used because the wave electric field component E_+ giving rise to absorption is small at the fundamental in a ^4He plasma, whereas there would be strong competition at $\omega = 2\omega_c(^4\text{He})$ and $\omega = 4\omega_c(^4\text{He})$ by the residual H remaining in the plasma. In experiments on JET up to 8 MW of ICRF power was applied at 57 MHz using waves with a symmetric toroidal wave spectrum. The absorption at harmonics is an FLR effect, and clear differences were observed between beams with 70 and 120 keV (Fig. 14). Information on the confined high-energy ^4He ions was obtained with a gamma-ray spectrometer, which showed peaks at the gamma-ray energy of 4.44 MeV (Ref. 42). They are due to the $^9\text{Be}(\alpha, n\gamma)^{12}\text{C}$ reaction between the accelerated ^4He and the intrinsic ^9Be present in the plasma. The reaction is sensitive to the high-energy part of the α distribution because of resonances at 2 MeV and at energies larger than 4 MeV. This demonstrates not only the presence of the fast ^4He particles but also the feasibility of the reaction to diagnose fast ^4He . Further evidence of α tail production came

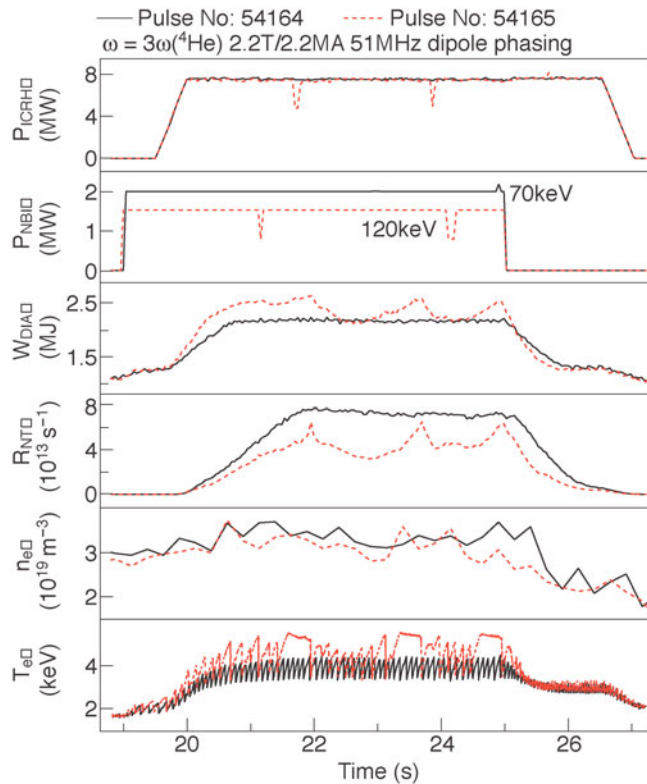


Fig. 14. Overview of two discharges with $\omega = 3\omega_c(^4\text{He})$, one with 70-keV beams and one with 120-keV beams.

from multiple toroidal and elliptical eigenmodes detected in the discharge with the 120-keV beams. The scheme was used in JET to study the alpha confinement in shear-reversed plasmas.⁸⁴

II.G.2. Plasma Start-Up

Using the standard ICRF antennas on JET, discharge initiation and wall conditioning experiments were performed on JET. Comparison with similar experiments on ASDEX Upgrade and TEXTOR showed that the breakdown time depends on the gas pressure and not on the machine size, indicating that the antenna near electric field plays a fundamental role in the plasma breakdown.⁸⁵

On JET a combinations of gases (80% He and 20% H) was first used to improve the plasma homogeneity. Analysis of the mass spectrum data indicates noticeable outgassing of deuterium, water, and hydrocarbons.

II.G.3. Simulation of the Dynamics of Burning Plasma

The dynamic of α particle heating and control of an equivalent $Q = 10$ burn was experimentally investigated using ICRF hydrogen minority heating in deuterium plasmas.^{68,86} The main aims were to demonstrate the qualitative features and to control a situation of “thermal runaway.” Indeed, in this situation obtained for Q larger than a threshold value, it is expected that a change in the plasma energy will result in a change of the α -particle power P_α larger than the increase of the loss power P_{loss} . P_α is then expected to be subject to unstable excursion that could be compensated by a change in the external heating. The experiments were performed in ELMy H-mode at $B_T = 2.5$ T and $I_p = 2.5$ MA. One component of the ICRF heating was applied in response to real-time measured plasma parameters (neutron D-D neutron rate ΔR_{D-D} , central electron density $n_e(0)$, central electron temperature $T_e(0)$, or volume-averaged electron temperature $\langle T_e \rangle$) to simulate the self-heating effect from α particles $P_{\alpha, sim}$, and a second component was used as external heating P_{ext} to control the “burn.”

In the first algorithm used, $P_{\alpha, sim}$ was assumed proportional to the measured ΔR_{D-D} , itself proportional to $T_e(0)^{1.5 \text{ to } 2.0}$, in a similar way to the appropriate scaling of the thermal D-T reaction rate ΔR_{D-T} . With P_{ext} simply preprogrammed, the onset of thermal runaway was found for $Q \approx 8$. Then, as illustrated in Fig. 15, a feedback term was added to the preprogrammed P_{ext} waveform to stabilize the excursion of $P_{\alpha, sim}$ at a reference level. Note the strong variation in $P_{\alpha, sim}$ due to sawteeth and the partially compensating effect of P_{ext} . The second algorithm used assumed $P_{\alpha, sim}(t) \propto R_{D-T, sim}(t)$ with $R_{D-T, sim}(t)$ a function of $T_e(0)$, $n_e(0)$, and $\langle T_e \rangle$ (see Refs. 68 and 86). Similar results were obtained with a more pronounced thermal instability, reflecting a more realistic calculation of $P_{\alpha, sim}$. Of course, in these kinds of scale model experiments of reactor-like scenarios, it is not possible to preserve all the

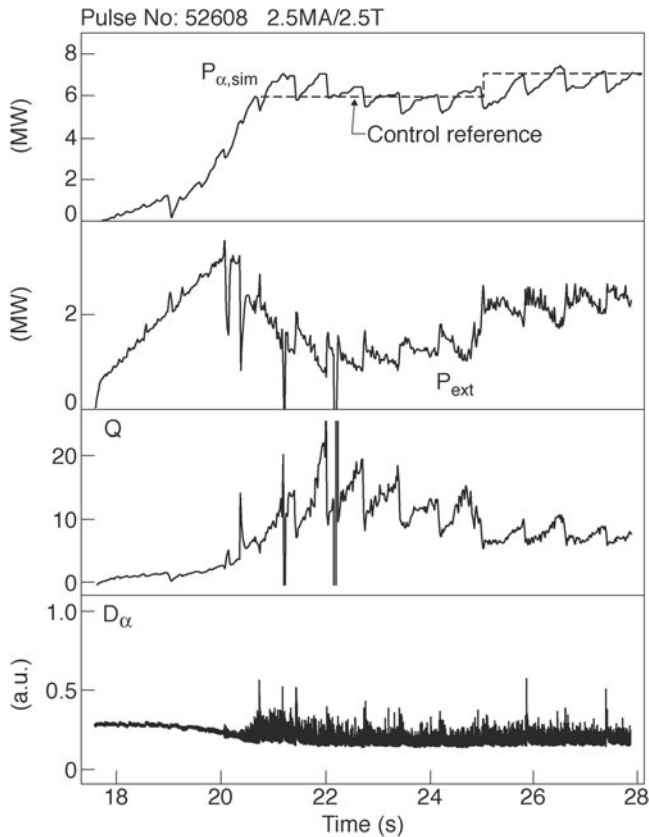


Fig. 15. Evolution of the alpha simulated power $P_{\alpha, \text{sim}}$, the external ICRF P_{ext} , the fusion gain factor $Q = 5P_{\alpha, \text{sim}}/P_{\text{ext}}$, and the ELMs. From Ref. 68.

relevant dimensionless timescales; nevertheless, several of the expected dynamic features of self-heated plasmas were successfully demonstrated.

II.G.4. ICRF Power Modulation for Transport Studies

A standard method to determine where the ICRF power is absorbed inside the plasma is to examine the ion and electron response to modulation of the launched power. Strictly speaking, this temperature response to abrupt ICRF power level changes merely provides a first good guess of the actual power deposition profile rather than the power deposition profile itself: Not only local sources but also heat losses and heat transport determine how the temperature evolves as a function of time and location. Making use of this, modulation of the ICRF power becomes an even more powerful tool for doing transport studies.^{48,87}

The electron temperature response to the ICRF power level changes is Fourier analyzed, and the amplitudes and phases of the first few temperature harmonics are compared with those predicted by the ASTRA transport model.⁸⁸ The ASTRA code not only solves the transport

equation on the modulation timescale but also allows integrating the slow time evolution. The former dynamics is governed by the perturbative transport coefficients, whereas the latter incorporates the actual transport. ASTRA flexibly allows testing various transport models. In particular, the stiffness of the electron heat transport in JET has been examined, the main outcome of the study being that the electron heat transport in JET is stiff and that the modulation analysis clearly identifies this stiffness. More recently, the same technique was adopted to probe ITB plasmas and demonstrated that ITBs are regions in which the diffusion locally becomes so low that heat wavefronts are essentially stopped when reaching it.⁸⁸ More in-depth analysis—which is still going on—brought out a number of more exotic effects such as the asymmetric (in/out) nature of the transport barriers and the fact that no presently available model is capable of reproducing simultaneously all experimentally observed features.

The crosschecking of ASTRA results against experimental data can be extended by adopting the “convoluted” information hidden in the temperature response to study local transport parameters in more detail. This idea is further elaborated upon in Chap. 10 of this issue.

II.G.5. ELM Toroidal Propagation

ELMs affect, through a fast change of the density in the edge, the coupling of the ICRF antennas.⁸⁹ A data acquisition system with high time resolution was used on JET to investigate the response of the four toroidally distributed antenna arrays. The signals change rapidly at the rising edge of the ELMs. The delay in the appearance of the perturbation on toroidally spaced antennas cannot distinguish between a toroidal or a poloidal rotation of a helical perturbation, or a combination of both. Assuming that the rotation is purely toroidal, the delay indicates a propagation of the ELMs moving in the electron diamagnetic direction with an average velocity propagation of typically 200 km/s (with values as low as 50 km/s and as high as 1200 km/s). The highest values correspond to the low-density cases. This could constraint the efficient working of a robust ELM-resilient ICRF system.

II.H. Outlook and Conclusions

The powerful and flexible ICRF system of JET over the years not only has allowed us to develop ICRF heating scenarios and investigate many fundamental ICRF physics aspects but first and foremost has contributed substantially to the results obtained on JET in numerous areas and has proved itself a powerful tool beyond simple heating.

The D-T experiments were a unique opportunity to fully qualify the ICRF scenarios for reactor plasmas. Bulk ion heating can be achieved, and the results are consistent with modeling. The control of MHD instabilities

with ICRF, of the transport of fast particles, and of plasma rotation confirms its capability to be used for multiple purposes, not just heating alone. Its use as a tool to produce energetic particles, condition walls, control a simulated plasma burn, probe transport, and investigate the plasma edge shows its wide versatility.

Further developments, including the capability to operate in regimes with strong ELMs, by using 3-dB couplers as implemented on ASDEX Upgrade, and conjugate-T matching and the installation of an ITER-like antenna²⁷ will continue to provide important contributions toward the physics and technology of ICRF for ITER.

III. PHYSICS OF NBI IN JET

III.A. Introduction

Although NBI had already been proved as an efficient method of plasma heating on magnetic confinement fusion devices when the auxiliary heating requirements for JET were being defined, the development toward the multimewatt, 10-s capability needed for JET was an enormous step. The original design performance of the JET NBI systems has been far exceeded, however, and the system is still the subject of ongoing performance enhancements, which is a testimony to the robustness and flexibility of the original design.

Following a brief technical overview in Sec. III.B, a discussion emphasizing the operational flexibility while drawing attention to any limitations is given in Sec. III.C. The following subsections then present examples of scientific exploitation of the physical properties and technical features of NBI in JET. These include the use of NB heating to produce high fusion performance plasmas (including D-T) in Sec. III.D, as well as specific NB physics effects such as beam fueling (including helium and tritium injection) in Sec. III.E, current drive in Sec. III.F, and beam-driven rotation in Sec. III.G.

It must be emphasized, however, that NB heating on JET has proved to be a mainstay of the experimental program and has contributed to virtually every facet. It therefore is not possible by any means to cover in the present summary all applications of NBI, which although they may have become routine are nevertheless of fundamental importance. Examples of such routine applications include establishing the confinement databases in JET and the characterization of the various divertor configurations, all of which have needed reliable high-power plasma heating and which would not have been possible without NBI.

III.B. Technical Overview and Evolution of the JET NB Injectors

The JET device is equipped with two NBI beamlines. Eight positive ion neutral injector (PINI) beam

sources are installed per beamline. The PINI consists of a “bucket” type filamented ion source and a set of electrostatic accelerator grids supported within a ceramic main insulator. The PINI beam sources were developed especially for JET and have been subsequently adopted on a number of other magnetic fusion devices within and also outside Europe. The basic beamline and PINI configuration is described in Ref. 90. The beamline is arranged into four quadrants in which a common residual ion deflection magnet and set of ion dumps (catering for full and fractional energy ions) serve a pair of PINI beams. The basic PINI design allows for variations to provide significant flexibility in the choice of acceleration voltage. In particular, tetrode (four-grid) and triode (three-grid) versions were developed and optimized for the production of ≈ 80 and 120 to 160 kV energy beams, respectively. For hydrogen isotopes, the ratio of accelerated atomic, diatomic, and triatomic ions has, to date, been optimized to maximize the full-energy component in the neutral beam (i.e., originating from atomic ions), through the appropriate choice of magnetic configuration of the ion source. The PINIs (source and accelerator grids) and beamline components such as deflection magnet coils, residual ion dumps, and box scraper, are all fully actively cooled. Other components such as the neutralizer, magnet liner, calorimeter, and duct scraper/liner rely on thermal inertia with interpulse heat removal via water cooling. The beamline design pulse length is 10 s, limited by the inertial components, though the power supplies are rated for 20 s and the actively cooled components are essentially suitable for continuous operation. The entire beamline and ancillary equipment were designed to standards compatible with tritium beam operation.

The injection geometry (Fig. 16) is such that one set of beams make a single pass through the plasma, with residual shinethrough power impinging on the inner tokamak wall, and a second set are slightly more tangential, making a double-pass, with residual shinethrough power impinging on the outer tokamak wall. The PINIs are arranged in two vertical banks of four on each beamline designated *normal* (single pass) and *tangential* (double pass). Compared with the torus major radius of 2.96 m, the tangency radii of the normal and tangential beams are 1.31 and 1.85 m, respectively.

The two basic PINI types (tetrode and triode) were originally foreseen to facilitate an evolution from all 80-kV/60-A PINIs, operated in hydrogen delivering ≈ 15 MW, to all 160-kV/30-A PINIs in deuterium delivering the same power with plasma heating characteristics similar to those in hydrogen, determined by the penetration of the beam into the plasma, which depends only on velocity (or energy per unit mass) for the different isotopes. The first JET beamline installed at machine Octant 8 was commissioned in 1986, in 80-kV (tetrode) PINI configuration, and operated initially in hydrogen. Due to limitations in the power-handling capability of

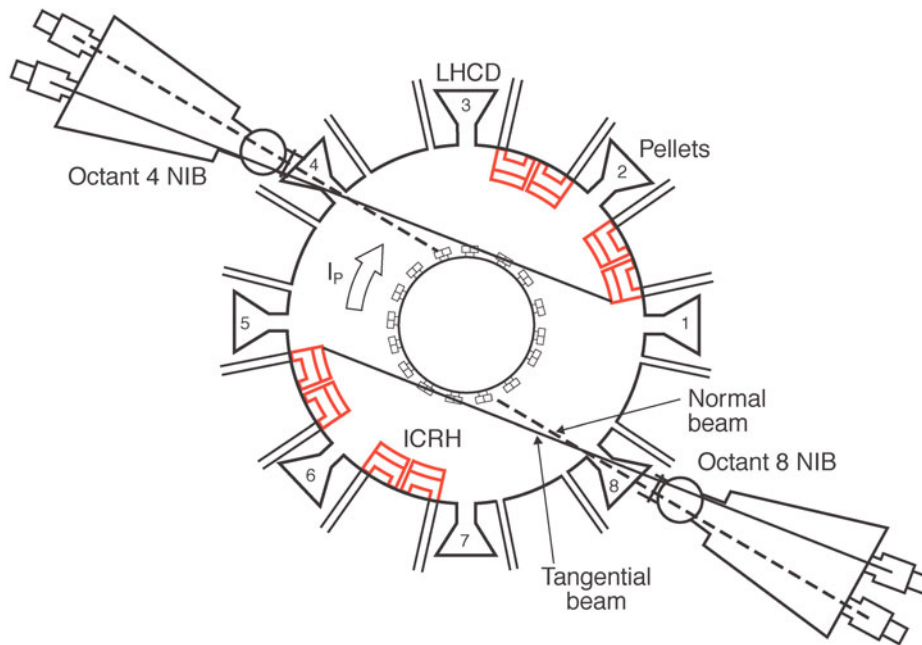


Fig. 16. Plan view showing location of neutral injector boxes (NIBs) and illustrating basic JET NBI geometry.

the full-energy residual ion dump, in part due to unforeseen reduction in the neutralization gas target due to beam-gas interaction heating effects,⁹¹ the voltage and power were limited below the original design values in hydrogen.

Operation soon switched to deuterium beams, which despite the reduced accelerated beam current (41 A at 80 kV) resulted in substantially higher neutral beam power of about 10 MW from the single beamline. The second beamline at Octant 4 was commissioned in 1988 (also using tetrode PINIs at 80 kV), and total injected power of >20 MW was achieved in that configuration.

In the period 1988 through 1991, the triode PINI accelerator was progressively introduced, though in slightly modified form compared with the original design, configured to accelerate deuterium beams at 140 kV/30 A. The reasons for this slight reduction in energy for the triode PINI were twofold, namely, to reduce the power on the full-energy ion dump and to allow eventual tritium beam operation at 160 kV/30 A, which provides a useful power increase due to the higher neutralization efficiency (at the lower beam velocity of the heavier isotope) and to taking full advantage of the current capability of the high-voltage power supplies. It should be noted in this context that for a fixed accelerator geometry, the optimum perveance relationship $Im^{1/2}/V^{3/2} = \text{constant}$ must hold, relating the energy (V), current (I), and isotopic mass (m) in order to maintain the beam optics. Following a limited period of operation with all PINIs configured for 140-kV/30-A deuterium beams (total power ≈ 16 MW) in 1991, it was concluded that this was not the optimum choice for high fusion performance hot-ion H-mode scenarios (see below).

The NBI configuration adopted for the first full deuterium-tritium experiment (DTE1) in JET therefore utilized eight 130-kV/30-A triodes on the Octant 8 beamline and eight modified “high-current” 80-kV/50-A tetrodes on the Octant 4 beamline, delivering a maximum combined power of >20 MW in deuterium and >22 MW when the Octant 8 beamline was operated in tritium. The design requirements, commissioning, and operation in tritium for the DTE1 experiment are described in detail in Ref. 92.

In 2003 the Octant 8 beamline was upgraded⁹³ by further modification of its eight PINIs to a 130-kV/60-A configuration, which required a major reconfiguration of the existing high-voltage power supplies and installation of additional new high-voltage power supplies, bringing the total deuterium power capability to 24.5 MW.

As well as operation with all the hydrogenic isotopes (including tritium), the large-scale open-structure beamline cryopumps were shown to be compatible with the use of helium as the beam parent gas (both ^3He and ^4He isotopes) through the use of argon prepulse frosting, and this has become a standard mode of operation for occasional dedicated campaigns. Technical aspects and operation experience of helium beam production are discussed in Ref. 94.

III.C. Coupling of NB Power to JET Plasma and Operating Limitations

NB heating is a very flexible technique, which has the advantage that the ability to couple power to the confined plasma is essentially independent of the magnetic

configuration and the value of the toroidal field and is effective over a wide density range. The beams become progressively attenuated as they pass through the plasma, as a result of a combination of charge exchange, ion impact, and electron impact ionization. The beam energy is therefore matched to the size of the device through the energy dependence of the cross sections for charge exchange and ion impact ionization, which mainly determined the choice of beam energy in JET to be of order 100 keV. Ionization of the beam as it traverses the plasma produces a local source of fast ions that thermalize by coulomb collisions as they circulate around the torus with an initial parallel velocity determined by the tangential component of the injection velocity. At low densities the shape of the power deposition profile per unit volume depends mainly on the geometry and is peaked on-axis. Peaked target plasma density profiles further enhance the peaking of the beam power deposition profile. At higher densities the power deposition profile becomes progressively flatter and eventually hollow, though even at the highest densities in JET nearly all the NBI power is deposited well within the H-mode edge transport barrier. At the lowest operating densities ($\approx 1.5 \times 10^{19} \text{ m}^{-3}$) residual beam shinethrough of the normal bank beams onto the graphite vessel can become high ($\approx 40\%$ of injected power). Operating instructions and interlocks impose a minimum allowed line-integrated target density for NBI and permit only a short period of beam (0.5 s) at the lowest densities. However, beam fueling normally results in a sufficient density rise at the end of the 0.5-s "notch" period to allow the beams to continue.

The application of NB heating is essentially independent of the plasma edge conditions. In particular, there is no practical constraint on the edge density (minimum or maximum) under normal operating conditions, and NB transmission is not affected by ELMs. Conversely, there is no deleterious effect from NBI on the plasma edge, e.g., from impurities that might affect the H-mode transport barrier under essentially all normal operating conditions. Only under extreme conditions of high edge density or very strong gas fueling/recycling does the possibility exist for excessive localized power loading on the side of poloidal structures located immediately adjacent to the beam ports (e.g., limiter or antenna elements) from the impact of beam ions created at the plasma edge, in the scrape-off layer, or by beam-gas collisions, especially at low toroidal field when the ion toroidal Larmor radius is large. However, suitably designed graphite tiles have essentially eliminated the problem on JET. For counterinjection of beams an additional restriction on plasma-limiter distance and/or density is necessary to limit the risk of vessel hot spots due to enhanced first-orbit losses. Similar occasional restrictions are necessary in experiments in which the toroidal field ripple is deliberately increased by applying a difference current to alternate sets of interleaved toroidal field coils.

Large ELMs result in sudden changes in the far stray vertical field, which affects beam alignment due to the influence on the beam before it is neutralized. The JET neutral beam magnetic field compensation⁹⁵ utilizes cancellation coils under active feedback control to maintain the stray field within an acceptable operating window, but large ELMs at high plasma current can produce occasional trips. Nevertheless, NB heating has routinely and successfully been applied in H-mode discharges with large ELMs up to 5-MA plasma current.

The neutral beams are transmitted into the JET plasma via a compact rotary high-vacuum valve assembly (used for isolation of the torus and beamline vacuum systems) and drift duct located between adjacent toroidal field coils. Due to the relatively long path length through the rotary valve and duct and the short horizontal distance across the duct determined by the toroidal field coils, reionization of the beam due to beam-gas interactions in this region presents an operational limit. This results from the unfavorable ratio of the gas conductance of the duct relative to the product of the beam current and reionization cross section. The manifestation of this limit is pressure evolution within the duct in response to the dumping of reionized beam particles due to their trajectories in the predominantly vertical stray poloidal field of the tokamak. The problem is exacerbated by the nonuniformity of the magnetic field leading to focusing and consequent localized hot spots on the duct walls, which in turn lead to enhanced thermal gas desorption. The duct protection has had to be progressively upgraded to accept higher reionization power density,⁹⁶ but the pressure rise in the duct can nevertheless restrict the available pulse length at high power depending on the tokamak magnetic scenario.⁹⁷ The main parameter affecting the duct limit is the plasma current, especially at very low values when the reionized power can reach unprotected areas far downstream in the mouth of the tokamak port. In practice, long-pulse NB heating has been routinely applied over a range of plasma currents from 0.5 to 7 MA with acceptable duct reionized power distributions, though a minimum current of 0.8 MA is normally applied for routine NBI. Heavy gas fueling in long high-power NB pulses can occasionally exacerbate the problem of duct pressure excursions in some scenarios.

The continual upgrades to the JET NB systems and their monitoring and protection systems have led to a progressive increase in both power and pulse length, with record values of power (23 MW) and injected energy per pulse (186 MJ) achieved in the most recent campaigns in 2006 and 2007, with a routine maximum delivered power of >20 MW. As a result of the flexibility of NB, it has remained the predominant heating method throughout the JET program, delivering high power in all plasma configurations over a very wide range of operating parameters.

III.D. Application of NB Heating for High Fusion Performance Plasmas

NB heating has been extensively developed in JET for the production of plasmas with high values of fusion reactivity, fusion amplification factor Q , and fusion triple product $n_i(0)\tau_E T_i(0)$. In particular, the hot-ion H-mode scenario was optimized to maximize fusion performance in the preparation for D-T experiments in JET (Refs. 98, 99, and 100) and was successfully exploited in the preliminary tritium experiment¹⁰¹ (PTE) and in the (DTE1) campaign.^{102–104} The hot-ion H-mode defines a regime in which intense NB heating at low electron density results in a situation in which the electron temperature T_e is raised sufficiently that the beams predominantly heat the ions, while the heat exchange between ions and electrons is weak. Under these conditions the ion temperature T_i exceeds T_e over a substantial proportion of the plasma volume (Fig. 17), and the thermal transport is predominantly via the ion channel, which is characterized by low thermal diffusivity. The centrally deposited NB heating profile further contributes to the good core confinement, and the core NB fueling helps to sustain a peaked density profile that in turn maintains peaked beam deposition. The highest-performance discharges were supplemented by moderate (≈ 3 -MW) H-minority ICRF heating in combination with >20 MW NB heating. A substantial contribution to plasma thermal energy arises from the large H-mode pedestal that develops over the course of the long ELM-free periods (≥ 1 s), and a significant contribution to the total reaction rate is attributable to beam-plasma reactions involving unthermalized fast ions. For example, in record D-T pulse 42976 shown in Fig. 18, $P_{fusion} = 16.1$ MW for $P_{NB} = 22.3$ MW and $P_{ICRH} = 3.1$ MW, with $Q_{in} = P_{fusion}/P_{total} = 0.62$ and thermonuclear fraction $f_{th} = 0.63$ (Ref. 104). Factors that play an important role in maximizing the performance and duration of the high fusion yield phase of these discharges are low edge recycling and avoidance of terminating MHD events, in both the core and the outer region, e.g., external kink instabilities.¹⁰⁵ Optimization of the plasma shape and edge recycling and careful gas puffing to avoid or delay such instabilities could all be carried out without affecting the effectiveness of NB heating.

The key NB characteristics giving rise to the favorable hot-ion mode behavior are core fueling and predominant ion heating. The instantaneous slowing-down rate of beam ions in a plasma is given by¹⁰⁶

$$\frac{dE}{dt} = -\frac{2E}{\tau_s} \left[1 + \left(\frac{E_{crit}}{E} \right) \right]^{3/2}, \quad (1)$$

where τ_s is the characteristic slowing-down time on the electrons and E_{crit} is the so-called critical energy (see Sec. II.B), and where for a pure hydrogen plasma of ion isotopic mass A_i and beam isotopic mass A_b

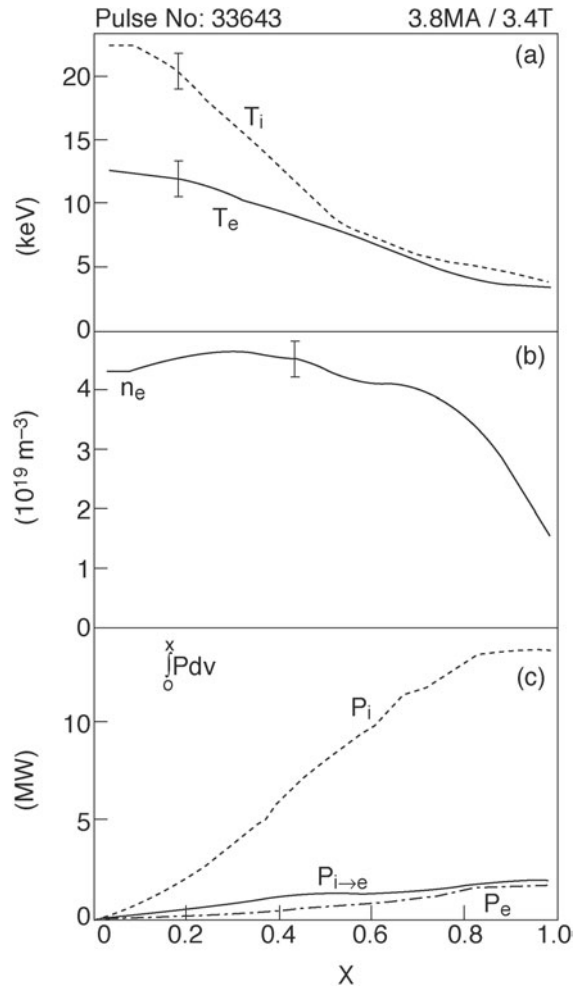


Fig. 17. Profiles of (a) ion and electron temperature, (b) electron density, and (c) rate of heating and ion-electron heat exchange integrated over the volume within a given minor radius at the time of maximum stored energy in hot-ion H-mode discharge 33643. From Ref. 99.

$$E_{crit} = 14.8 \frac{A_b}{A_i^{2/3}} T_e. \quad (2)$$

For high values of E/E_{crit} the beam ion energy loss is mainly through electron collisions, and at $E = E_{crit}$ the rate of energy loss to plasma ions and electrons is equal. The total energy transfer for a beam ion injected at energy E to ions and electrons is equal for $E = 2.41E_{crit}$ (Ref. 107). From these considerations it is clear that under JET hot-ion H-mode conditions, such as those illustrated in Fig. 17, the ions are preferentially heated, and that lower-energy beams favor ion heating, as well as increasing the fueling per unit power. This partly explains why it was advantageous to retain one set of 80-kV PINIs in the NB energy mix during the preparations for DTE1, as

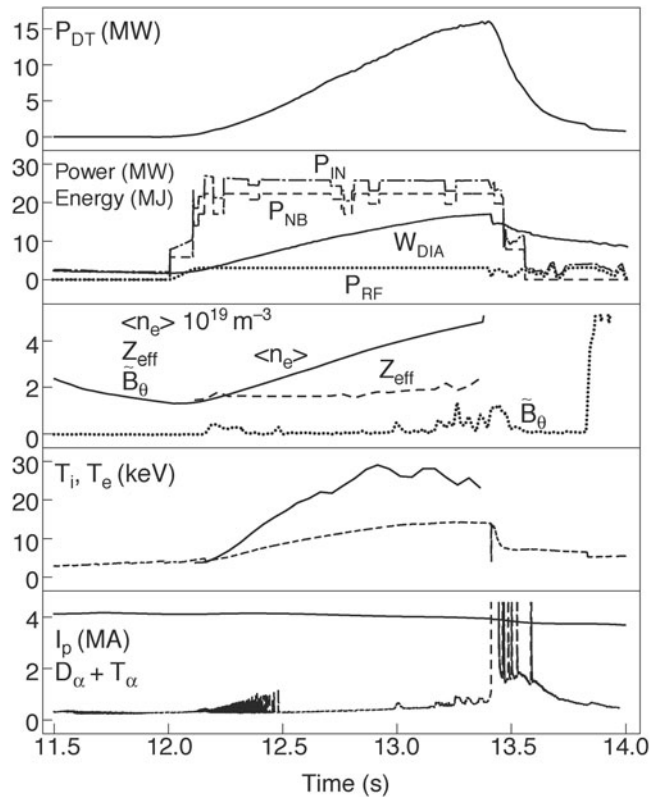


Fig. 18. Time traces for D-T hot-ion H-mode discharge 42976 (4 MA/3.6 T), which attained the highest fusion power. From Ref. 204.

mentioned in Sec. III.B, in addition to the higher power delivery.

The NB-heated ELM-free hot-ion H-mode was particularly well suited to the demonstration of unambiguous electron heating by alpha particles in the DTE1 campaign. The ideal experiment for this purpose must be designed such that the alpha-particle heating provides the maximum possible contribution to the electron power balance in the core plasma, over a period that is long compared with the alpha-particle thermalization time. This requires the maximum Q value, whilst minimizing the direct heating of the electrons by the external heating as well as the heat transfer to the electrons from ion-electron equipartition. All these requirements were satisfied by the hot-ion H-mode with exclusively NB external heating. The experiment consisted of varying the D-T mixture at constant beam power, by using different combinations of deuterium and tritium beams, and by wall-loading at the correct isotopic mix (see Sec. III.E.1). The relationship between the central electron temperature and the power balance in the core region was then investigated as the reaction rate was varied according to the fuel mixture. The experimental details were all optimized to eliminate, as far as possible, other sources of electron temperature changes, and the results provided unambig-

uous evidence for alpha-particle heating,^{108,109} in line with predictions assuming classical slowing down and confinement of the alpha particles.

In an interesting variation of the neutral beam-heated hot-ion H-mode, the ability to inject helium beams was exploited. Experiments with both ^4He and ^3He NBI at 120 keV into deuterium plasmas have been carried out.¹¹⁰ Due to the higher value of E_{crit} for helium, a slight enhancement in ion heating was observed, as expected, compared with deuterium beams at the same power, with ^3He beams giving a more peaked deposition profile due to the higher velocity at the same injection energy. The main purpose of these experiments was to allow analysis of neutron emissivity profiles resulting purely from thermonuclear D-D reactions, without any contribution from beam-plasma reactions. The analysis yielded ion temperature profiles that gave good agreement with other diagnostics. A further result from the measurements described in Ref. 110 is that there was no measurable effect on the He beam deposition profile, attributable to the formation of helium metastables (during the neutralization process) with resultant increase in cross sections for ionization processes in the plasma.

III.E. Fueling

In a tokamak of JET's size and with beam power in the range of 10 to 20 MW at order 100 keV energy, the particle source ($\approx 10^{21} \text{ s}^{-1}$) from NBI represents a significant fueling source. Furthermore, since the source is in general centrally deposited, and certainly well beyond the scrape-off layer and the edge transport barrier in the H-mode, it is of high fueling efficiency. These NB fueling characteristics have been of importance in establishing and developing the high-performance regimes in JET, and also the advanced scenarios in which significant beam fueling within the ITB occurs. In this section, two examples of different kinds of experiment are discussed, namely, studies of global and local fueling and particle confinement in JET, that were facilitated by the particular fueling characteristics of NBI.

III.E.1. Global Plasma Fueling and Particle Confinement

In performing experiments on particle confinement in tokamak plasmas, in contrast with measurements of energy confinement, it is in principle much more difficult to define the source term and its spatial profile due to the effect of particle recycling. The flux of recycled particles generally exceeds the external fueling rate, and the recycled particle source is difficult to discriminate from the external gas fueling.

Early analysis of the beam fueling characteristics of limiter (L-mode) and X-point (H-mode) plasmas in JET (Refs. 111, 112, and 113) highlighted the importance of the separate effects of core fueling by beams and edge

fueling by the recycled particles. These analyses also demonstrated that excess fueling, over and above the beam particle input, could be explained only by net desorption of gas from the plasma-facing surfaces, especially limiters and divertor target plates. The dynamics of the density response to beam heating and fueling in general exhibited characteristics of an excess fueling phase (recycling coefficient $R > 1$) followed by a beam fueling phase with efficiency less than unity ($R < 1$). Due to the unambiguous knowledge of the beam fueling within the bulk plasma, as a particle source distinct from that due to recycling, it was possible to analyze the dynamic density transients following NBI to infer simultaneous values of the global plasma particle confinement time τ_p and the dynamic retention time (of order seconds) of particles within those plasma-facing components responsible for the dominant recycling fluxes, as well as the magnitude of the dynamic particle inventory available for release from those surfaces.¹¹² This approach identified the importance of the plasma-facing components as dynamic particle reservoirs, which can act as both fueling source or sink. Such insight was subsequently useful in the optimization of conditions for high fusion performance operation and other experiments dependent on low-recycling conditions.

This topic was studied in detail in the DTE1 campaign, since it is of crucial importance in the control of the D-T fuel mix. Although the combination of PINs operated in deuterium and tritium had been selected to provide approximately balanced D and T beam fueling, it was clear that contribution to fueling from the wall reservoirs would potentially disturb the fuel mix, which strongly affects fusion reactivity, as illustrated by the following example of a TRANSP code¹¹⁴ prediction of the D-T fusion power, using data from a reference D-D hot-ion H-mode discharge with 19-MW deuterium NBI. The prediction describes the situation with mixed D and T beams at the same total NB power. The result can be expressed as

$$P_{D-T} = 4f(1-f) \times 6.2 \text{ MW} + 2f \times 0.13 \times P_{NB}^{D0} + 2(1-f) \times 0.20 \times P_{NB}^{T0}, \quad (3)$$

where the terms represent the thermal and beam-plasma (D \rightarrow T and T \rightarrow D) contributions, respectively. The parameter f represents the fraction of tritium in the plasma, assumed to be uniform throughout the volume. The ratio of T:D NB fueling is about 3:4 for the chosen beam mix. If the plasma fueling during the ELM-free period is dominated by NB fueling, the plasma mix would then reflect that of the beams, i.e., $f = 0.43$, close to the optimum in this parameter. However, from the D-D discharges it was not possible to establish the relative contribution to plasma fueling from the beams and from recycled particles; this can be supposed to be in the ratio 1: f_w . In contrast to the earlier experiments on beam fueling discussed above,

excess global fueling was not observed in these discharges, and the density rise corresponded reasonably closely to the beam fueling. Compared with those earlier experiments, the wall conditions had been carefully optimized to reduce recycling to the absolute minimum, and the divertor cryopump provided an additional particle sink. However, dynamic particle *exchange* with plasma-facing surface reservoirs remained a likely possibility. In particular, in a D-T discharge if f_w is significant, and if furthermore it is postulated that the isotopic composition of the recycling flux reflects that of the walls/divertor surfaces, achieving the desired plasma D-T composition would require control of the D-T content of the recycling surface reservoirs. This crucial aspect was confirmed in the series of experiments described below.

The principle of the mixture control experiment was to scan the beam D-T mix from zero to 100% at constant power under conditions in which the recycling particles consisted of deuterium only. A predictive TRANSP run was carried out for an 11-MW NB-heated D-D reference discharge, resulting in an equation similar in form to Eq. (3). Using this, P_{D-T} was computed for various beam mixes between zero and 100% tritium. For each beam mix, f was first computed for various values of f_w (assuming the composition of recycled particles was pure deuterium). The family of curves for P_{D-T} versus beam mix shown in Fig. 19 is thus obtained; each curve is identified with a value of the parameter f_w . This procedure formed the basis of the mixture control experiment, carried out under low-recycling conditions when the vessel surfaces had not been exposed to significant tritium

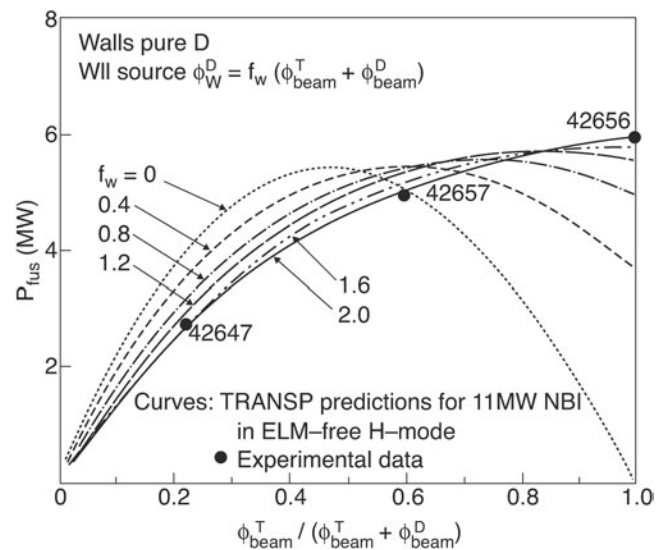


Fig. 19. Predicted and achieved D-T fusion power versus beam D:T fueling ratio for an ELM-free plasma with 11-MW total NBI, for various fractions f_w of the total plasma fueling attributable to deuterium fueling from the plasma-facing components. From Ref. 205.

(especially from gas fueling, which is effective at loading the walls). In Fig. 19, the best match to the experimental data is obtained for the curve labeled $f_w = 2$. This result led to the unambiguous conclusion that the vessel walls should be preloaded to reflect the desired plasma D-T mix for the high-performance D-T discharges. It is to be expected that suprathreshold tritium beam ions incident upon plasma-facing components are more likely to contribute to long-term tritium retention, due to greater implantation depth, than thermal ions.¹¹⁵ However, in general in DTE1 discharges the gas fueling rates and thermal particle recycling rates greatly exceeded the beam-ion losses, and therefore use of tritium NBI is not considered to have affected the total long-term tritium retention in JET significantly.

III.E.2. Local Particle Transport

The well-defined local particle source from NB-injected particles lends itself to experiments to measure local particle transport coefficients. NBI has been used to inject minority species for this purpose, in particular helium, in order to simulate a central source of thermalized alpha particles for the study of helium ash transport.

The first simulated helium ash transport experiments¹¹⁶ in JET were conducted prior to the installation

of the pumped divertor. Although they were carried out in X-point plasma configurations (L- and H-modes) there was no pumping of the helium, which consequently recycled fully. However, it was still possible to obtain information on the effective helium particle diffusion coefficient from the radial redistribution of the thermalized He^{++} , following a 0.5-s He beam “blip” during the transient period after the He beam was terminated but before the onset of helium recycling. The He^{++} density was measured with charge-exchange recombination spectroscopy (CXRS) viewing a deuterium beam on the other injector box. Results for an L-mode plasma are shown in Figs. 20a and 20b. By comparing the results with a predictive simulation, the effective diffusion coefficient D_{He} was inferred, with $D_{\text{He}} \approx 0.3 \text{ m}^2 \text{ s}^{-1}$ (L-mode) and $\approx 0.6 \text{ m}^2 \text{ s}^{-1}$ (H-mode). Results from thermal transport analysis in similar discharges indicated that $\chi_{\text{eff}}/D_{\text{He}} \approx 3$, which suggested that transport of thermalized He ash from the core should not set a fundamental limit to maintaining an ignited plasma against the possibility of He buildup, provided the edge exhaust and pumping were adequate.

In subsequent experiments in L-mode and ELMy H-modes on other machines, however, it was always found that the He exhaust rate is limited by the pumping efficiency and not by He transport in the plasma.^{117–120} More

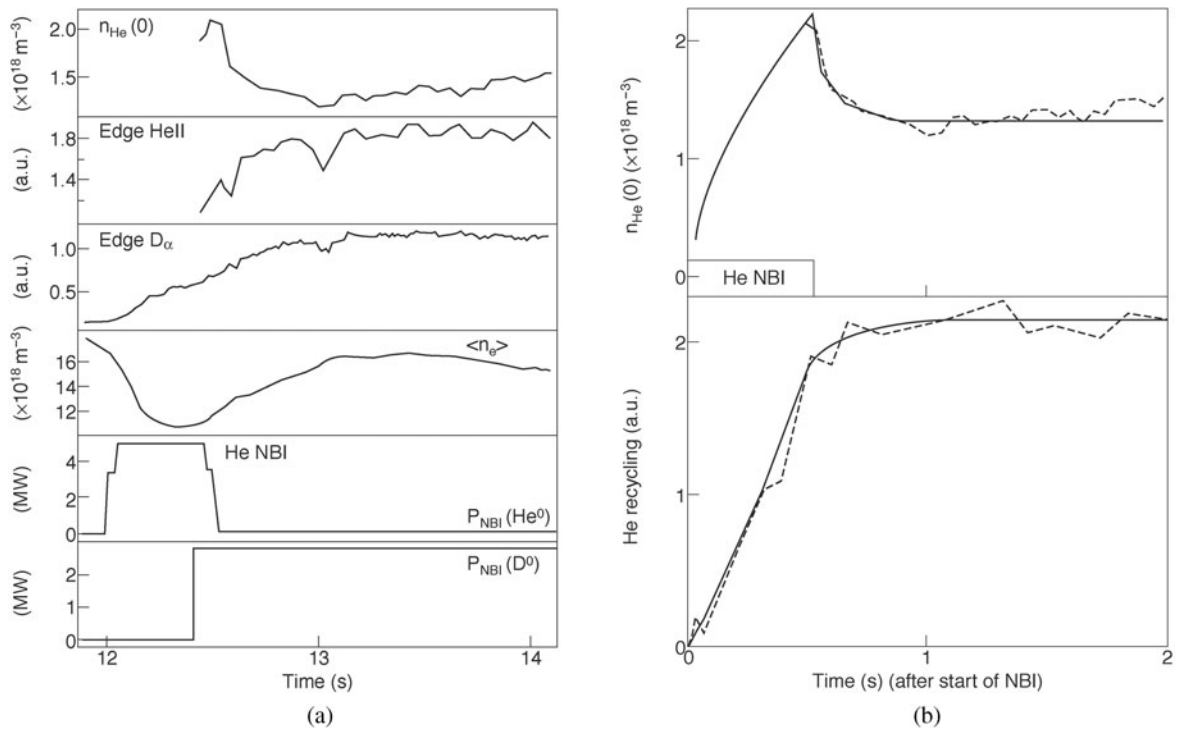


Fig. 20. (a) Time traces for JET discharge 22977 (3.5 MA/2.5 T, double null X point) showing L-mode evolution of central helium density $n_{\text{He}}(0)$ and He recycling following a 120-kV $^4\text{He}^0$ NBI pulse. From Ref. 116. (b) Measured (dashed line) and fitted (solid line) evolution of $n_{\text{He}}(0)$ and edge HeI recycling signal for the JET discharge depicted in (a). From Ref. 116.

recent experiments in JET were therefore conducted in H-mode and ITB plasmas but with more sophisticated transport analysis and with the benefit of He pumping from the divertor cryopump using Ar frosting in the JET MkII GB divertor configuration. As well as providing the opportunity to study He exhaust via the complete process, including edge exhaust and pumping, it was important to check that the He transport characteristics through the ITB layer itself would not pose a problem for He accumulation in the core, in contrast to the standard L- and H-mode situations. When there is complex structure of the internal transport coefficients, it is essential to use a central source of He. The experiments on He transport through the ITB reported in Ref. 121 studied the He particle replacement time with a central source of He delivered by NBI within the ITB. In these experiments approximately 60% of the helium was deposited within $r/a = 0.4$, i.e., within the region enclosed by the ITB. Quasi-steady-state He exhaust was achieved using the Ar-frosted divertor cryopump, which reduces the He recycling flux and helps to maintain a low edge density throughout. The discharge shown in Fig. 21 has a value of the ratio of the He replacement time to energy confinement time $\tau_{\text{He}}^*/\tau_E \approx 5$ that is acceptable for the avoidance of He accumulation in a burning plasma, dem-

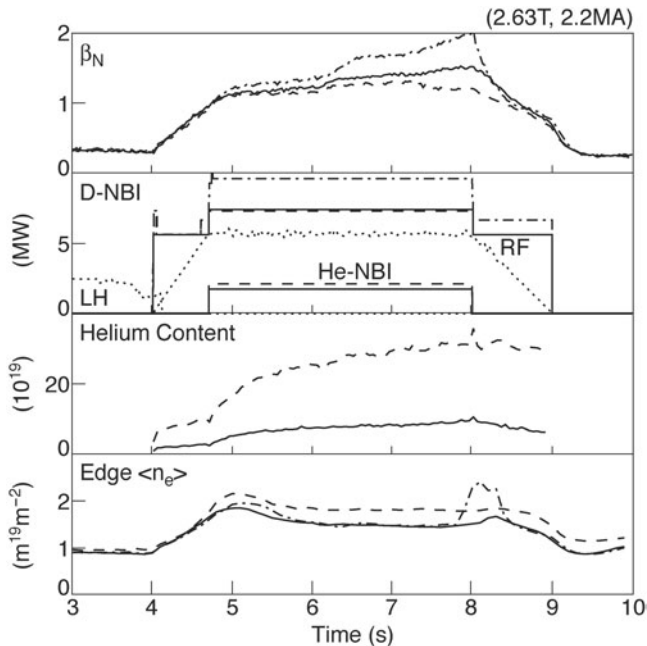


Fig. 21. Comparison of three ITB discharges: one with 8-MW D beams and 2-MW He beams but without Ar-frost divertor cryopumping of He (dashed lines), the same pulse repeated but with He pumping (solid lines), and a reference 10-MW D-only NB pulse (dashed-dotted lines). Note that LH and ICRF powers are shown for only one pulse for clarity. From Ref. 121.

onstrating that the ITB does not prevent effective He removal. The experiments also demonstrated that the value of τ_{He}^* is dominated by edge transport and recycling (i.e., the limitation of the pumping).

In addition to the experiments on transport of NB-injected helium, a very detailed study of local particle transport for NB-injected tritium was possible through the interpretation of 14-MeV neutron emissivity profiles following short 100% tritium beam “blips” into deuterium target plasmas. The most recent and very extensive set of such measurements was carried out during the JET trace tritium experiment (TTE) campaign in 2003 and is reported in Ref. 122. The same reference also describes detailed studies of fast particle behavior based on comparison of predicted 14-MeV neutron profiles, due to reactions of the injected tritons prior to thermalization, with the measured neutron data. Energetic He^{++} particle populations, produced by acceleration of beam-fueled helium by high-harmonic ICRF heating to MeV energies, has also been the subject of detailed investigation in JET at fast-ion β values relevant to ITER (Ref. 109).

III.F. NB Current Drive

III.F.1. Theoretical Considerations

The following simple relation expresses the result of an analytic Fokker-Planck treatment of the electrons¹²³ to give the beam-driven current for a toroidal plasma in the large aspect ratio approximation in the low collisionality banana regime, where it is assumed that the inequality $v_b \ll v_e$ holds for the fast ions and electrons, respectively:

$$\frac{I}{I_f} = 1 - \frac{Z_f}{Z_{\text{eff}}} + 1.46\sqrt{\varepsilon} \frac{Z_f}{Z_{\text{eff}}} A(Z_{\text{eff}}) . \quad (4)$$

Here, I/I_f is the ratio of the net current to the fast circulating ion current and $\varepsilon = r/R$ is the inverse aspect ratio. $A(Z_{\text{eff}})$ is a function whose value ranges from 1.67 for $Z_{\text{eff}} = 1$ to 1.18 for $Z_{\text{eff}} = 4$. Z_f is the charge of the fast beam ions. In Eq. (4), the second term represents the electron current in the absence of trapped electrons and is an approximation of a displaced Maxwellian electron distribution that holds for $v_b \ll v_e$. The third term is the reduction in the magnitude of the electron current due to the presence of trapped electrons; this term is minimum in the plasma center and tends to zero on-axis. The inequality $v_b \ll v_e$ is valid for hot plasmas such as those in NB current drive experiments in medium-sized and large tokamaks such as JET.

Equation (4) in principle may be applied locally in the plasma, thereby characterizing the beam-driven current density at a given magnetic flux surface. In actual calculations of the beam-driven current, an NB power deposition code may be used to determine the radial profile of the beam-ion source function. In computing the local fast-ion current density j_f , 2-D Fokker-Planck or

Monte Carlo calculation of the beam ion velocity distribution is normally performed, incorporating the effects of trapping of the unthermalized ions. Equation (4) is then used to compute the local ratio of net beam-driven current to fast-ion current j/j_f . The effect of fast-ion trapping is to reduce the local value of j_f ; the proportion of the beam ions in trapped orbits depends on injection angle and deposition profile. In the absence of trapping, an analytic solution to the Fokker-Planck equation for the beam ions can be written as follows¹²⁴:

$$j_f = \frac{S\tau_s eZ_f v_0}{(1+u_c^2)} \int_0^1 f_1(u) u^3 du, \quad (5)$$

where τ_s is the fast ion slowing-down time on the electrons, S is the local fast-ion source rate due to beam deposition, and u is the fast-ion velocity normalized to the injection velocity v_0 . The distribution function f_1 is the first-order Legendre polynomial component of the fast-ion velocity distribution and is given by

$$f_1 = u^{2\beta} \left(\frac{1+u_c^3}{u^3+u_c^3} \right)^{1+2\beta/3}$$

with

$$\beta = \frac{m_i Z_{eff}}{2m_f \bar{Z}},$$

$$u_c^3 = \frac{3\sqrt{\pi}}{4} \frac{m_e \bar{Z} N_{Te}^3}{m_i v_0^3},$$

and

$$\bar{Z} = \sum_i \frac{m_f n_i Z_i^2}{m_i n_e}, \quad (6)$$

where the subscripts i and f refer to the plasma and fast ions, respectively.

The efficiency for generating the fast-ion current is defined as the ratio of fast-ion current density j_f to NB power deposited per unit volume $P_d (= m_f v_0^2 S/2)$. Evaluation of the above expressions shows that the highest efficiency is achieved by operating at the highest electron temperature and lowest density in order to maximize τ_s and by choosing the fast-ion energy to be close to the critical energy at which the effects of collisions with electrons and collisions with thermal ions are approximately equal. In practice, the choice of beam energy in JET is determined by the heating requirements (central power deposition, preferential ion heating, and fueling). It should be noted that once ion heating dominates, increasing the electron temperature (e.g., by supplementary ICRF heating) is ineffective for increasing τ_s . Since the circulating fast-ion current (I_f) increases with beam tangency, the constraints posed by the restricted port ac-

cess in JET (due to the large number of toroidal field coils) further limit the NB current drive efficiency in JET.

III.F.2. NB Current Drive Experiments in JET

Only a limited set of experiments dedicated to NB current drive have been conducted in JET (Ref. 125) in view of the factors discussed in the previous paragraph.

In experiments on noninductive current drive, a significant change to the current profile following application of the drive mechanism can be expected only over a timescale that is long compared with the resistive diffusion timescale (many seconds in large devices such as JET). This is due to the fact that the driven currents induce local return currents in the plasma, via changes in the local toroidal electric field, which decay on a resistive timescale governed by radial diffusion of the poloidal magnetic field. The total noninductive plasma current in principle can be computed from the expression

$$I_{NI} = I - \int \sigma_{nc} E_{\parallel} dA, \quad (7)$$

where I is the measured plasma current, σ_{nc} is the neo-classical conductivity, and the integral is over a poloidal cross section. However, the local time-dependent parallel electric field E_{\parallel} may not be directly available from measurements. The noninductive beam-driven current therefore is usually inferred from the measured and predicted surface loop voltage and a realistic assumption about field diffusion.

In the JET experiments a fully time-dependent calculation of the surface loop voltage was carried out for a reference discharge using the TRANSP code,¹¹⁴ in which the NB- and bootstrap-driven currents were computed from the measured plasma profiles and from a numerical solution of the Fokker-Planck equation for the fast ions. This agreed well with the measured loop voltage, indicating the validity of the noninductive current computation. Equation (7) was also evaluated for many other NB-heated discharges, assuming radially constant E_{\parallel} derived from the measured loop voltage. The resultant interpreted noninductive currents agreed well with the summed theoretical values of beam-driven and bootstrap contributions, computed for the measured plasma and beam deposition profiles. These JET results are illustrated in Fig. 22 and are taken from Ref. 125.

Although the JET NB systems are not well optimized for maximizing the magnitude of the beam-driven current, NB current drive nevertheless plays a fundamental role in the control of magnetic shear in the advanced tokamak scenarios in conjunction with LHCD, and advanced real-time multivariate control of all the heating and current drive systems has been successful in prolonging the duration of the regime toward quasi-steady-state conditions in JET in more recent experiments.¹²⁶

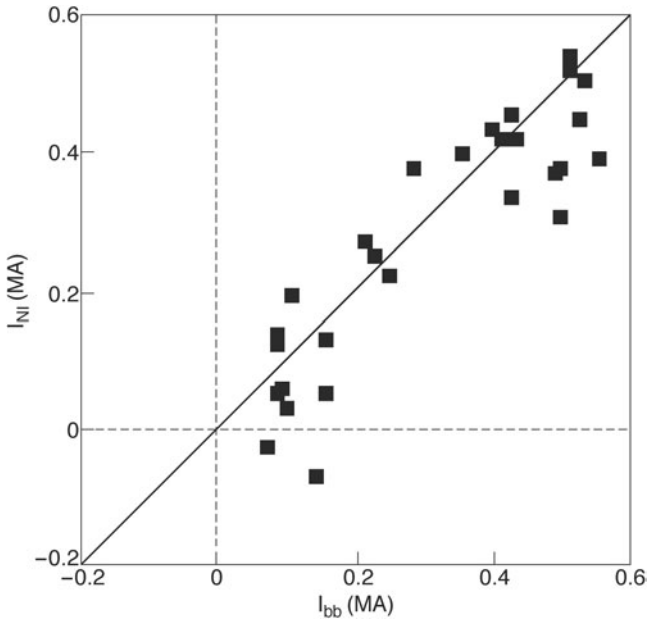


Fig. 22. Experimentally interpreted total noninductive current (I_{NI}) versus predicted value I_{bb} (beam-driven plus bootstrap current) for several pulses with co-NBI and counter-NBI. The magnitudes of the beam-driven and bootstrap currents are similar (about 250 kA) in these JET plasmas. From Ref. 125.

III.G. Toroidal Rotation

Toroidal rotation is a natural consequence of the angular momentum imparted to the plasma by the beam. The trajectory of an incoming beam particle intercepts each flux surface at a characteristic pitch angle ξ that varies with minor radius (r). The imparted angular momentum per beam particle (L_f) resulting from its ionization at a major radius R_f depends only on the tangency radius (R_T) of the particle trajectory, and hence the beam-line geometry, irrespective of the major radius (R); i.e.,

$$L_f = m\xi v_b R_f = m v_b R_T, \quad (8)$$

where m is the beam particle mass and v_b is the beam particle velocity.

If the beam particle is ionized at large enough major radius, the resulting ion will undergo a trapped banana orbit. The condition for this may be expressed in terms of the local pitch angle:

$$\xi > \xi_t = \sqrt{\frac{2\varepsilon}{1+\varepsilon}}, \quad (9)$$

where the inverse aspect ratio $\varepsilon = r/R$.

Particles ionized farther inboard will undergo passing orbits. The mechanism for momentum transfer is different in the two cases of trapped and passing particles. In the former, the radial electric current associated with

the radial displacement of the ion orbits exerts a $j \times B$ toroidal torque on the plasma.¹²⁷ For the passing particles, most of the momentum is transferred via Coulomb collisions as the ions thermalize (though there is also a small $j \times B$ term in this case). A third contribution to the torque is due to that part of the momentum of the injected particles in passing orbits that remains after they have fully thermalized and joined the background ion population, due to the plasma rotation. This contribution is denoted the transformation torque. The combined result is that a radially distributed toroidal momentum source is supplied by NBI, which drives and sustains plasma rotation. There are other drivers of toroidal rotation such as the $E \times B$ term in the ion pressure balance, which can become significant in regions of high ion pressure gradient, such as ITB or H-mode transport barrier. However, in JET the rotation from NBI dominates.

The momentum imparted to the plasma is transported radially in a way analogous to the thermal flux, and it can be described by a viscosity or more commonly by a momentum diffusivity. It has generally been assumed in the literature that momentum transport is subject to anomalous enhancement over the neoclassical values in a way similar to thermal transport. Early studies of beam-driven rotation in JET (Ref. 128) indicated a strong correlation between central rotation velocity and central ion temperature. Since the heating and momentum sources are closely related, it may be shown as in Ref. 128 that the ratio of the momentum and ion thermal diffusivities χ_ϕ/χ_i may be estimated without carrying out a local transport analysis. The results in Ref. 128 suggested that $\chi_\phi/\chi_i = 1 \pm 0.3$, evaluated from a database including L-mode, H-mode, and hot-ion H-mode with intense NB heating and central ion temperatures up to 25 keV and central rotational angular velocity of up to 190 krad s⁻¹.

In further JET experiments¹²⁹ the evolution of the radial rotation velocity profile from CXRS has been analyzed. The separate effects of the prompt torque exerted at large normalized minor radius and the delayed buildup of the central velocity on a timescale set by the collisional slowing-down time have been elucidated from these measurements, illustrated in three time frames following application of NBI in a hot-ion H-mode discharge (Fig. 23).

In more recent JET experiments on rotation in NB-heated plasmas,¹³⁰ radial profiles of rotation velocity and ion temperature from CXRS were subject to analysis of the respective gradient scale lengths in order to investigate in more detail the relationship between χ_ϕ and χ_i . Since the transported quantity is momentum, the rotation profiles are converted to profiles of momentum density by multiplying by the local mass density. The results showed that contrary to the earlier results and also to the assumption generally made in predicting the rotation in ITER, there can be significant variation in χ_ϕ/χ_i , and the ratio was generally found to be in the range 0.18 to

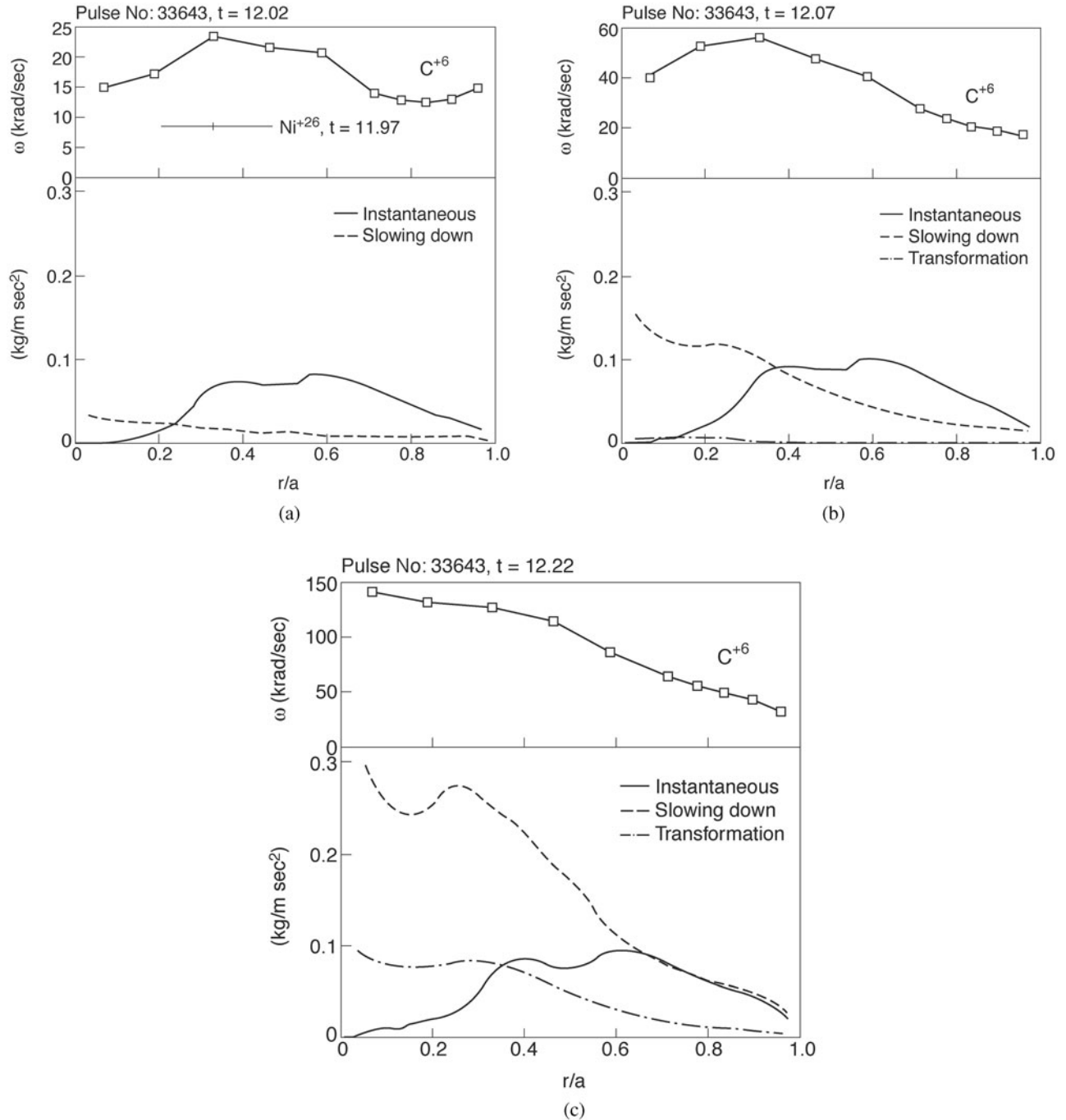


Fig. 23. (a) Toroidal angular velocity averaged over the first 50 ms after application of strong NB heating (top) and calculated torque per unit volume for prompt ($j \times B$) and collisional torque transfer to the plasma from NBI (bottom). (b) Same as for (a) but averaged over the period from 50 to 100 ms after start of NBI. (c) Same as for (a) and (b) but averaged over the period from 200 to 250 ms. All are from Ref. 129.

0.35 for measurements made with H-mode and ITB plasmas. The lowest values were found in high-density plasmas closest to the ion temperature gradient turbulence threshold, which had the highest values of χ_i , whereas proximity to the threshold did not seem to affect the

momentum density gradient. However, even for low plasma density scenarios such as the ITB cases, the ratio is still significantly less than unity. The analysis took account of the fact that the profiles of the momentum and ion-heating source term are not necessarily strongly

coupled. This is due to the fact that when the electron temperature is sufficiently low, a significant proportion of the NB heating is delivered to the electrons. This means that in high-density JET H-modes, for example, the momentum source can be flat or even hollow while the ion heating profile is peaked. Such differences in source terms, together with differences in momentum and heat diffusivities, explain why for JET plasmas a coupling between NB-driven rotation and ion temperature does not always hold.

III.H. Conclusion and Outlook

The JET NB injectors have been demanded in nearly every JET experimental operational shift since the first NB system was commissioned in 1986. The flexibility of the NB heating technique and reliability of the JET PINI beam sources, beamline components, and ancillary equipment have enabled the JET NB systems to contribute to an extremely wide range of experiments. NBI has provided the dominant heating power contribution to all the basic plasma modes of operation (L-mode, ELM and ELM-free H-mode, advanced scenarios, and regimes optimized for high fusion performance) over a wide range of basic machine operating parameters (plasma current, toroidal field, magnetic configuration, and density). In addition, there are many examples of specialized experiments that were possible only by making use of the particular characteristics or capabilities of the NB injectors in the areas of current drive, particle confinement and transport, and toroidal rotation. Not all of these particular characteristics translate directly to the next step such as ITER or to a reactor; for example, the much higher energy (1 MeV) of the ITER heating beams means that electron heating will predominate, and the fueling and momentum input per unit power will be much lower than in JET. However, these qualities have enabled experiments to be carried out in JET that were crucial for addressing key physics issues for ITER. For example, the ion-heating properties of NB heating in JET provided the only route to obtaining a high enough fusion Q in D-T plasmas to allow a direct observation of alpha-particle self-heating. Similarly, the high momentum input has led to a level of understanding of momentum confinement that gives a good level of confidence in the extrapolations of rotation behavior in low-torque ITER plasmas, which are expected to play an important role in ITER's performance through turbulence suppression. The JET NB injectors continue to be developed and enhanced. A major upgrade of the PINI beam sources, beamline components, and power supplies is in progress, scheduled for commissioning in 2010. This will raise the NB-injected power to at least 34 MW and the pulse length to 20 s (Ref. 131). This upgrade will permit a program of experiments to support ITER's needs through the ability, for example, to study plasmas at high current and toroi-

dal field while maintaining key dimensionless parameters such as β and ρ^* as close as possible to ITER value.

IV. LHCD STUDIES AT JET

IV.A. Introduction

The lower hybrid (LH) range of frequencies satisfies $\omega_{ci} < \omega < \omega_{ce}$ and depends on the excitation of the so-called slow wave that propagates nearly parallel to the magnetic field with the electric field aligned with the magnetic field. The wavelength parallel to the magnetic field is less than the vacuum wavelength and is defined by its parallel refraction index, n_{\parallel} , which is the ratio of the vacuum wavelength to the parallel wavelength in the plasma. This parameter determines the initial angle of propagation of the wave relative to the magnetic field and in part the trajectory within the plasma, which is also determined by the local plasma parameters. The LH wave is evanescent at the edge of the plasma. To minimize the power reflected back to the LH launcher, the width of the evanescent layer has to be minimized. This cutoff density is a function of frequency and is $1.7 \times 10^{17} \text{ m}^{-3}$ for $f = 3.7 \text{ GHz}$. Once the slow wave has tunneled through the evanescent layer at the plasma edge, it can become a backward wave if n_{\parallel} is above a critical value, the so-called accessibility condition.

Initial applications of LH waves were to heat bulk plasma ions, which requires n_{\parallel} to be in the range of 2 to 5 in order to have a perpendicular index n_{\perp} high enough to obtain ion Landau damping (see Ref. 132 and references therein). However, if high-energy ions are present in the plasma, such as alphas in fusion plasmas, coupling of the wave to fast ions can take place at much lower values of n_{\parallel} . Bulk ion heating was moderately successful. Major successes were obtained for current drive application of the LH waves (LHCD). In effect, the slow wave propagating parallel to the magnetic field can accelerate electrons in one direction if the wave has an asymmetric launch spectrum. The larger the speed of accelerated electrons, the more effective the current drive. n_{\parallel} values of 1 would correspond to the speed of light but the corresponding wave is not accessible. Very effective LHCD experiments were achieved in the early 1980s in several small experiments (for example, see Ref. 132), leading to fully noninductive current drive. In addition, suppression of MHD instability events, such as sawteeth, likely to be due to change of the plasma current profile by LHCD, was also reported.¹³³

It is on this basis that it was decided in 1986 to select LHCD among various methods of noninductive current drive in tokamaks (lower hybrid waves, fast waves, electron cyclotron waves, NBI, etc.) for the development of a current profile control system for JET, taking into account the availability of high-power sources and current

drive efficiency. The frequency chosen was 3.7 GHz as a compromise between the density required for coupling (the higher the frequency, the higher the density in front of the coupler needed to tunnel the LH wave) and the coupling to alpha particles and ICRF-induced fast ions (the lower the frequency, the stronger the damping). The range of n_{\parallel} spectrum (around 1.85) was selected so as to produce off-axis current drive, according to rather simple considerations. A prototype system was used in 1990 through 1992. The full system was installed in 1993 and has been in continuous operation since.

From 1993 to 1995, the LHCD system was used to suppress sawteeth in ELM-free H-mode plasmas and in high-power ICRF-heated plasmas, during the current plateau. The principal use of the LHCD in JET started with the 1996 experiments with an extensive use in the prelude phase of advanced tokamak scenarios such as optimized shear plasmas (see Chap. 4 of this issue). A more systematic approach was used starting in 1999 in which the LHCD has proved to be an essential system for the development of advanced scenarios in providing an externally controllable current profile tool. In particular, its use in the prelude phase has permitted us to compensate for varying plasma conditions at the start of advanced scenario plasmas.

The description of the LHCD system together with the presentation of some limiting technical problems that have an impact on the physics program are given in Sec. IV.B. Achieving sufficient coupling has been one of the major challenges of the LHCD experiments at JET. Major breakthroughs in coupling are described in Sec. IV.C, including the development of techniques allowing good coupling to be achieved in the most extreme ITER-like conditions. Current drive and other physics results are discussed in Sec. IV.D. Main achievements of LHCD as a current profile control tool are given in Sec. IV.E. Conclusions and outlook for LHCD are described in Sec. IV.F.

IV.B. Description and Limits of the LHCD System

The full LHCD system for JET was designed with the capability to launch up to 10 MW to the plasma for 20 s, aiming at generating off-axis current drive in high-performance plasmas. At the time, proper conditions for fusion-relevant performances at JET were not developed and the initial design of the launcher system was for a 5-MA limiter plasma.

An LHCD launcher has to generate an rf electric field polarized parallel to the magnetic field with a spatial distribution along the field matching the wavelength of the desired wave and a minimum density determined by the cutoff density. All presently operating subsystems use an array of waveguides mounted close to the plasma edge, the so-called grill. Introducing a controlled phase shift between single-mode waveguides results in a field distribution that propagates along the array with a veloc-

ity, and thus an n_{\parallel} , that is determined by the phase shift. The launcher is composed of 48 multijunctions¹³⁴ (waveguides with internal power splitting), each splitting into eight narrow waveguides of dimensions 9 mm × 72 mm, so that the launcher mouth consists of 384 narrow waveguides in 12 rows and 32 columns. In addition, there are 2 passive waveguides on each side of each row, to smooth the transition in electric field between the waveguides and the protection limiters. Built-in $\pi/2$ phase shifters in the small waveguides provide a narrow n_{\parallel} spectrum with high directivity. The peak of the main lobe in the n_{\parallel} spectrum can be varied between 1.4 and 2.3 by varying the phase difference between adjacent multijunctions. The majority of the LHCD experiments have been carried out with 0-deg phasing between multijunctions, which gives an n_{\parallel} spectrum centered at $n_{\parallel 0} = 1.84$, with full width $\Delta n_{\parallel} = 0.46$. The quality of the wave coupling is assessed by the power reflection coefficient, which is the amount of power reflected back to the source, divided by the forward power. To ensure good coupling of the LH waves, the radial position of the launcher was adjusted in real time using hydraulic actuators (the typical response time used in real-time application was 0.1 to 1 m/s) to maintain the requested value of reflection coefficient (usually in the range 3 to 5%) by using a feedback loop on the reflection coefficient.

A prototype LHCD system¹³⁵ was used in the experiments in 1990 through 1992, when JET was still in limiter configuration. In particular, the prototype system was used in the development of 7-MA limiter discharges, allowing enough volt-second saving for a 2-s plateau to be achieved. The full 3.70-GHz LHCD system has been in operation in JET since 1994 (Ref. 136) with a divertor configuration. Accordingly, the shape of the launcher had to be adjusted to the new (at the time) shape of 3- to 5-MA divertor plasmas. The launcher was not actively cooled given the low power losses in the launcher (~3%) and the maximum pulse duration expected at the time of design. A view of the launcher inside the JET torus can be seen in Fig. 24.

One of the difficulties in launching high-power LH waves in the plasmas is arcing in the long vacuum waveguides (due to an increase in the neutral pressure as the temperature of the waveguides increases when they are powered) and at the grill mouth. A rather complex conditioning procedure has been set up that is described in Ref. 137, aiming at reducing the increase of gas in the vacuum waveguides. It has been established that the power handling of the full LHCD system on plasma was limited by the maximum electric field in the waveguides once the waveguides had been conditioned by an extensive vacuum conditioning campaign, the limit being 400 to 500 kV/m. The electric field depends on the forward power density and the reflection coefficient. Therefore, high power ($P_{LH} > 6$ MW) can be coupled only when the reflection coefficient is low (<3%), and feedback control of the launcher position on the reflection coefficient

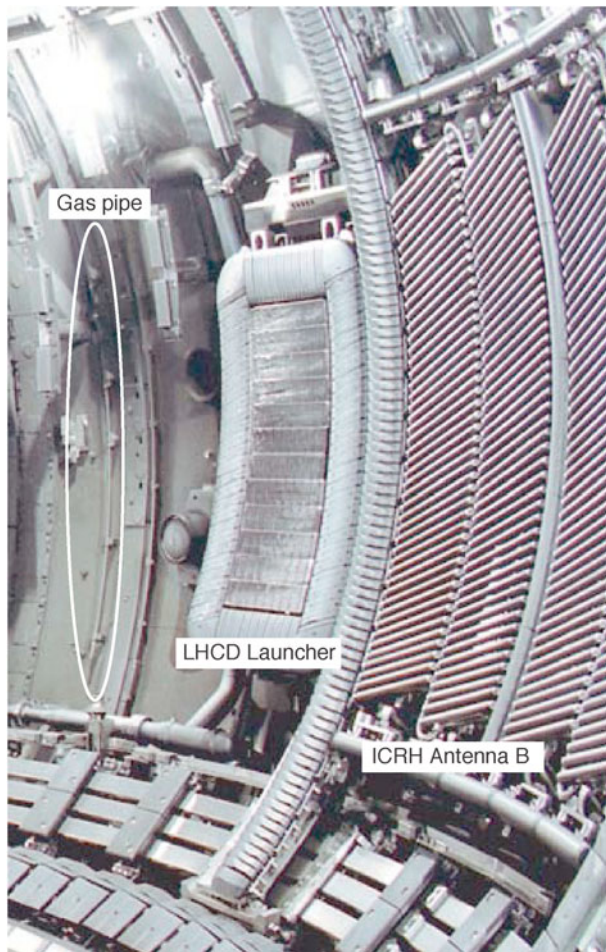


Fig. 24. View of the LHCD launcher during an opening of the machine in 1995. The damage to the top left of the launcher waveguides has already taken place. The location of the gas pipe can be seen ~ 1 m to the left of the launcher. To the right are the beryllium shields covering the straps of ICRF antenna B.

was therefore used routinely in these high LHCD power experiments performed in plasma limiter configurations. High-power pulses with $P_{\text{LH}} \geq 5$ MW and 12-s duration have been delivered to the plasma and the maximum coupled energy has reached 68 MJ, as can be seen in Fig. 25 (the loss of LH power due to degraded coupling conditions when ICRH is turned on has since been attributed to rf sheaths affecting the scrape-off layer (SOL) plasma, described in Sec. IV.C.4). The maximum coupled LH power in these conditions has reached 7.3 MW, using 8.2 MW of generator power. In addition, sawteeth have been fully suppressed in 2- and 3-MA discharges, with central $n_{e0} < 2.0 \times 10^{19} \text{ m}^{-3}$ and $< 1.3 \times 10^{19} \text{ m}^{-3}$, respectively, i.e., in conditions close to full noninductive current drive and with off-axis LH power deposition profiles. The time evolution of q_0 and the sawtooth activity for a 3-MA discharge are shown in Fig. 26 (Ref. 138).

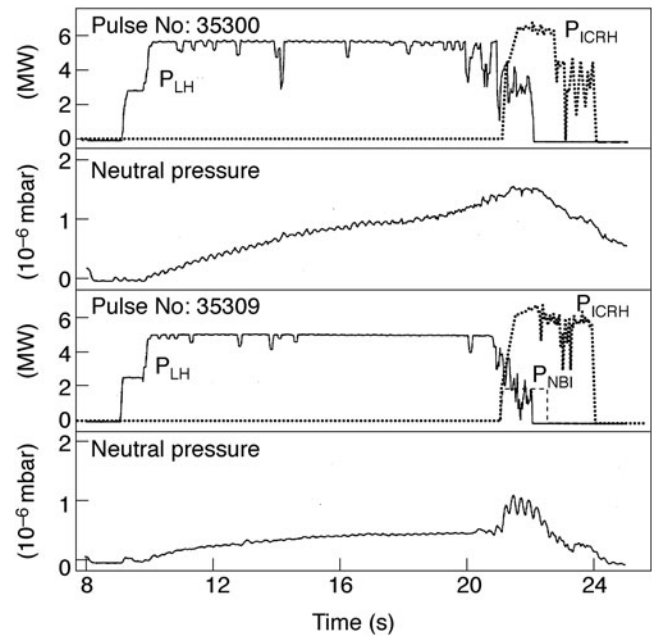


Fig. 25. Maximum coupled LH energy during plasma pulses and evolution in neutral gas pressure in the launcher tank. From Ref. 137.

Although the value of q_0 (from magnetic reconstruction) cannot be determined with great accuracy, the relative change is more demonstrative, an equivalent ohmic pulse presenting a stationary q_0 . The role of LHCD as a tool to change the current profile was thus demonstrated.

However, in H-mode plasmas with divertor configuration, launching high LH power became a very severe problem due to the reduction of electron density in front of the launcher. Operation with the LHCD launcher as close as possible to the last closed magnetic surface was attempted to try to reduce the reflection coefficient, but this sometimes resulted in the production of metallic impurities detrimental to high-quality plasmas. This is attributed to harmful plasma-launcher interaction and is characterized by increased radiation in front of the LHCD antenna, measured by a bolometer camera situated in the same octant as the launcher, in addition to iron and nickel line radiation measured by ultraviolet spectrometers. Since its first operation in 1994, the present JET LHCD launcher has accumulated damage such as blobs and protuberances on its top left corner and melted material in the middle of the rows, as can be seen in Fig. 24, although this does not prevent power being launched through the damaged waveguides. A recent visual inspection of the grill has established that the damage continues to accumulate, and determining the causes is relevant to future applications of LHCD in fusion devices. In Ref. 139 three causes of impurity radiation from the LHCD launcher—fast electrons created parasitically in the SOL (see paragraph below),

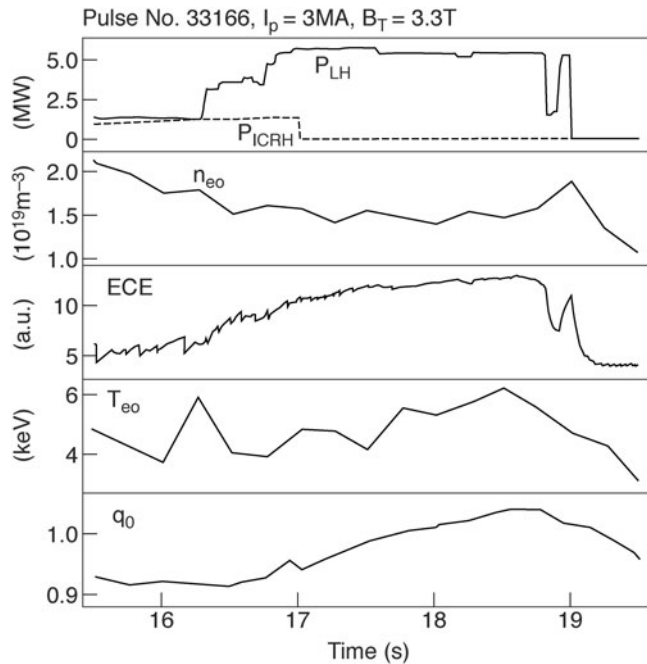


Fig. 26. High-power LH pulse and the resulting sawteeth suppression. Central q values are calculated from magnetic reconstruction. From Ref. 138.

arcs in the waveguides or at the grill mouth, and fast ions escaping from the main plasma—have been investigated and their occurrence in JET assessed. Attempts have been made to find a correlation between the impurity generation from the launcher and the heating sources and plasma parameters. In particular, the fast ions are found to be responsible for the enhanced radiation for $P_{\text{NBI}} + P_{\text{ICRF}} > 8$ MW, whereas the destructive action of the other two candidates—the fast electrons and the arcs—depends on the launched LHCD power and the launcher power handling. This study is proceeding.

Another potential problem is the formation of hot (bright) spots on components magnetically connected to the grill region. These bright spots were first observed in JET in 1996 in the divertor region¹⁴⁰ and are also attributed to the acceleration of electrons in front of the grill mouth. The most probable reason is the fast electron generation by parasitic absorption of the very high n_{\parallel} modes of the LH wave spectrum (with $n_{\parallel} > 20$) in front of the grill mouth.¹⁴¹ These high- n_{\parallel} components are due to small-scale-length features of the grill mouth. For example, the septums separating each small waveguide are 2 mm wide, with sharp edges, which result in abrupt changes in the electric field. This effect could be minimized by a better shape of the grill mouth as proposed in Ref. 142, but it was not possible to test this on JET. It has been shown¹⁴³ that an important parameter is the distance from the last closed flux surface to the limiter. The brightness of the spots clearly decreased with increasing

distance, possibly because the density in front of the grill decreases (this was shown to be a key parameter for the total amount of power lost to that mechanism in other machines; for example, see Ref. 144). With a new infrared camera, quantitative measurements (temperature) of hot spots on components magnetically connected to the LH antenna have been obtained for the first time in JET (Ref. 145). The temperature depends on power density per row rather than simply on total power, suggesting that the electric field is the relevant parameter. This is also consistent with observations in other machines.¹⁴⁴

All of these effects have severely limited the amount of LHCD power available in high-performance plasmas. The techniques to overcome long-distance coupling were developed in the 2000s and are described in the next subsection.

IV.C. Coupling Issues

IV.C.1. Optimization of LH Wave Coupling

How well the LH wave is coupled depends partly on the antenna geometry, but mainly on the electron density in front of the grill, $n_{e, \text{grill}}$, which must be above the cutoff density for good coupling. The coupling of the slow wave using an array of waveguides is usually described by the 2-D linear theory developed by Brambilla,¹⁴⁶ which was found to be in satisfactory agreement with several experiments, except at high power density, where evidence of nonlinear effects has been observed (for example, see Ref. 147). In addition, it neglects nonlinear interactions of the electric field with the plasma in front of the grill, although evidence for such effects in certain conditions has been reported, including in JET (hot spots; see Sec. IV.B). The current JET launcher is composed of multijunctions that have, among others, the advantage of reducing the power reflected back to the source,¹³⁴ compared to a conventional launcher (i.e., made of an array of independently powered waveguides). However, the launcher was initially designed for limiter plasmas, and it had to be adapted to the new JET divertor configuration late in the project. The multijunction lengths were reduced so that the poloidal shape of the launcher matched the poloidal limiter shape. A consequence of this is that the distance from the front end of the antenna to the E-plane junction is not that originally selected for optimizing the launcher's spectrum directivity and reflection coefficient. Also, it differs on the different rows. This means that it is not possible to obtain the low reflection coefficients predicted in Ref. 148 using the slow wave coupling code SWAN (Ref. 149) specially developed for modeling multijunctions. In Ref. 150, the effect of the nonoptimal distance to the E-plane junctions on the reflection coefficient for each row was modeled using the same code. The results are closer to the experimental results than the prediction using the ideal distance to the E-plane junction originally intended. To try to

compensate at least partly for this, the radial distance between the launcher protection limiter and the waveguides was decreased to ~ 2 mm to minimize the width of the evanescent layer. Also, as mentioned in Sec. IV.B, real-time applications (control of the plasma shape and location and/or of the launcher position) were developed to optimize coupling in various plasma conditions. The most successful scheme, i.e., control of the launcher position to maintain the reflection coefficient in a predetermined range, was limited by the fact that having the launcher too close to the plasma during high NBI + ICRF power could lead to detrimental interaction of fast particles with the grill.

On ASDEX, it was shown that LH wave coupling could be improved by puffing gas.¹⁵¹ This pointed to a possible means to control coupling independently of the main plasma conditions and motivated the installation of a specially designed gas pipe next to the JET launcher in 1995. This pipe is situated ~ 1 m away from the launcher toroidally and is at the wall, i.e., ~ 0.5 m behind the typical launcher position radially. It is fed from the top and has eight holes of increasing diameter from top to bottom, to counterbalance the conductance change along the pipe and provide the same amount of neutrals poloidally. Improvement of the coupling was observed on all rows when puffing D_2 . However, the improvement was marginal on the two top rows.^{140,152} No improvement was observed when puffing gas from locations not magnetically connected to the launcher. To try to improve the reflection coefficient on the top rows, two holes were added at the top of the gas pipe at the end of 1996. This had little success: For the same quantity of gas, compared to results obtained with the eight-hole pipe, the coupling on the top rows was very little improved, and it was worse on the bottom row. An in-vessel inspection in 2002 revealed that the additional holes were made too wide (see discussions in Sec. IV.C.2).

As mentioned in the introduction, the possible uses of LHCD evolved as new scenarios were developed. For example, predictive modeling showed that an additional (off-axis) current drive component would make it possible to sustain the q profile of advanced tokamak scenarios on the timescale required.¹⁵³ However, such applications required coupling large amount of LH power reliably in plasmas with H-mode edge. The n_e decay length of the SOL plasma in H-mode is smaller than in L-mode. As a result, n_e in the far SOL, at the location of the launcher, usually becomes lower than $n_{e,cutoff}$. Also, the rapid $n_{e,SOL}$ changes due to ELMs affect the reflected power and can increase the number of trips from the launcher safety system. Finally, the plasma shape in these plasmas, especially at high triangularity, often does not follow the launcher poloidal shape, so coupling conditions on different rows vary. This makes it very difficult to provide sufficient LH power. Experiments in 1998 demonstrated that although it was possible to obtain good coupling in ITB plasmas with

H-mode edge, the quantity of gas needed for good coupling on all rows was too high and degraded the plasma performance.¹⁵⁴ SOL studies in 1999 showed that puffing CD_4 increases n_e in the SOL plasma without affecting n_e at the separatrix (and hence is less likely to affect the main plasma performance).¹⁵⁵ This made it a good candidate for LH coupling and motivated experiments described in Ref. 156 that showed that with relatively small amounts of CD_4 , the LH wave coupling can be improved sufficiently in plasmas with ITBs, without affecting the main plasma performance. Additionally, good coupling was possible even with the launcher positioned far behind the limiters (up to 2 cm), where it is protected from detrimental interaction with fast particles escaping the plasma. In some of these experiments, measurements with a reciprocating Langmuir probe (RCP) showed that the increase in $n_{e,SOL}$ is local; i.e., it occurs only in the flux tube magnetically connected to the LH antenna (and gas pipe). This suggested that LH plays a role in the ionization process, either through losing some of the LH power in the SOL or because of changes in the local transport. Modeling with EDGE2-D (Ref. 157) explored the latter and showed that the change in n_e could be reproduced assuming changes of the transport in the SOL (Ref. 158). These experiments made LHCD available for a larger number of applications in JET. In particular, it made it possible to demonstrate that ITBs could be sustained by controlling the q profile^{159–161} (see Sec. IV.E). As described below, in more recent experiments D_2 has been used successfully to improve LH coupling in ITB plasmas and is now preferred to CD_4 . By puffing D_2 near the launcher, 3.5 MW of LH power was coupled in a plasma with ITB and ELMy H-mode, at the same time as 8 MW of ICRF and 20 MW of NBI.

IV.C.2. LH Coupling in ITER-Like Conditions

From 2003, the emphasis was put on demonstrating coupling in ITER-relevant conditions. This represents a challenge, because it means obtaining good LH coupling for plasma-launcher distances (d_{PL}) of ~ 15 cm (the typical d_{PL} in JET is 6 cm), in plasmas at high triangularity (δ) with H-mode edge. Since CD_4 is not desirable for ITER, because of tritium codeposition issues,¹⁶² it became important to try to use D_2 again. Also, in the 2002 shutdown, the two holes that had been added at the top of the gas pipe were blocked. This made it likely that less gas would be required for similar coupling improvement and supported the proposal to use D_2 . In 2003, good LH wave coupling in ITB plasmas at low δ with type I ELMs was demonstrated with CD_4 (Fig. 27) and with D_2 (Fig. 28; Ref. 163) with $d_{PL} = 11$ cm (the launcher was 0.5 cm behind the poloidal limiters). With D_2 the type I ELMs are smaller, indicating that D_2 affects the plasma edge differently than CD_4 . Experiments using ITB plasmas at high δ but small d_{PL} showed that good LH coupling could

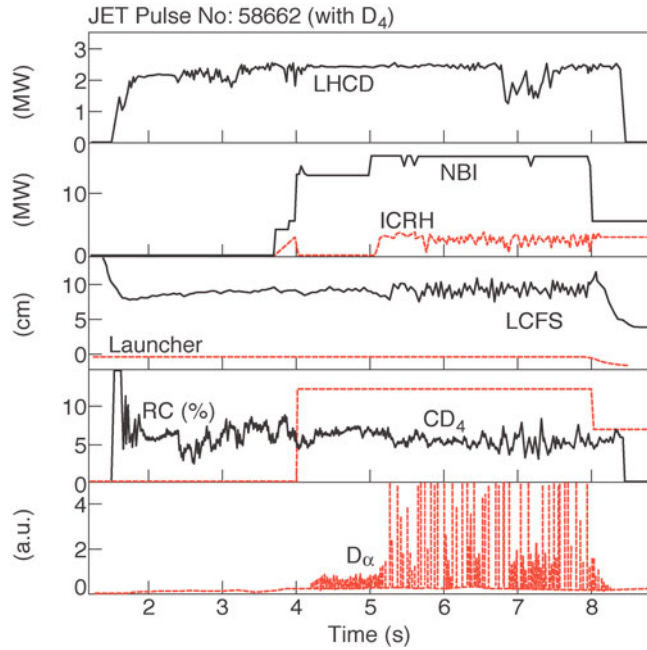


Fig. 27. Long-distance LH coupling during type I ELMs, using CD_4 injection near the launcher. The panels show LHCD power, NBI and ICRH powers, positions of the LCFS and launcher relative to the limiter, average reflection coefficient and CD_4 puffing rate (12×10^{21} el/s), and D_α signal. From Ref. 163.

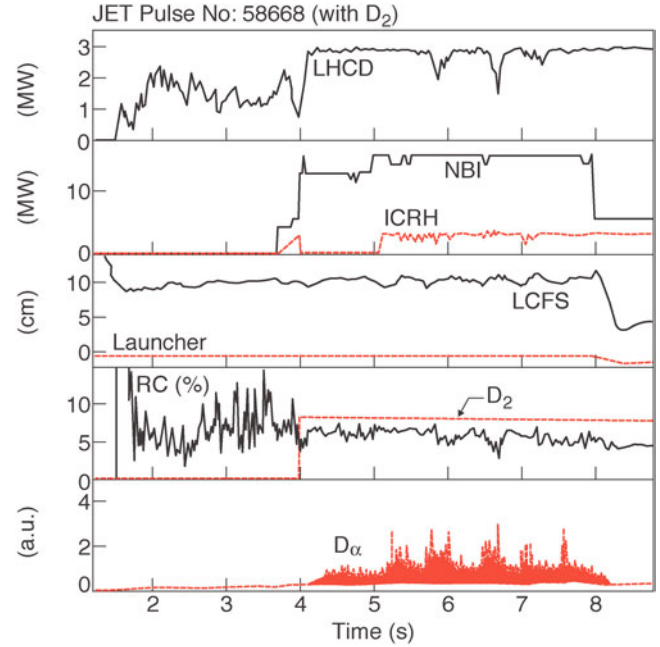


Fig. 28. Long-distance LH coupling using D_2 injection. The launcher-plasma distance is 11 cm. The panels show LHCD power, NBI and ICRH powers, positions of the LCFS and launcher relative to the poloidal limiter, average reflection coefficient, D_2 puffing rate (8×10^{21} el/s), D_α signal. From Ref. 163.

be obtained on all rows, despite the fact that the plasma-row distance varies due to the strong plasma shaping, by puffing D_2 from the near gas pipe. These results were improved during the 2006 and 2007 experimental campaigns: Good LH coupling at ITER-like δ was obtained at d_{PL} up to 15 cm in ITB plasmas ($\delta_{lo} \sim 0.5$ and $\delta_{up} \sim 0.4$; Ref. 145) and hybrid plasmas ($\delta_{lo} \sim 0.4$ and $\delta_{up} \sim 0.5$; Ref. 164), where δ_{lo} and δ_{up} refer to the lower and upper triangularity (Fig. 29). In these experiments the launcher was 1 cm behind the poloidal limiter. It is important to note that the performance of the ITB plasmas was not modified by the D_2 injected from the near gas pipe, contrary to what was observed previously. This is attributed to the fact that less D_2 is needed for improving the coupling, following the gas pipe modification.

IV.C.3. SOL Characterization During LH and Gas Puffing and Modeling

Time was devoted to characterizing the SOL plasma during P_{LH} and gas puffing. In order to improve the understanding of the phenomena leading to the increase of $n_{e,SOL}$, so as to extrapolate with some confidence the near-gas recipe to ITER (Ref. 145). In these experiments, the effect of the amount of gas, the LH power, and d_{PL} was studied. $n_{e,SOL}$ was measured with the RCP, which was situated at the top of the machine, at a different

toroidal location (octant 8) from the LH launcher (octant 3). The RCP is moved vertically in and out of the plasma to provide information on the electron density profile. In the experiments described, it shares the same magnetic flux tube as the LH antenna and the gas pipe. With P_{LH} and gas puffing, the far $n_{e,SOL}$ (i.e., a few cm away from the separatrix) increases compared to the case with gas puffing only, confirming that the LH power does affect the ionization. The increase is more pronounced at higher P_{LH} (and lower reflection coefficient is obtained as a result). In addition, the important parameter is the LH power density, rather than the total power. This is consistent with results from other machines, where it is found that the parasitic loss of LH power in the SOL in front of the LH grill depends on the electric field (i.e., the power density) at the grill.¹⁴⁴ The analysis of these experiments continues.

An important question arising from these experiments is whether the LHCD efficiency is decreased due to excessive power losses in the SOL when gas puffing is used¹⁴⁰ or due to changes of the wave characteristics as it travels through a “long” SOL. This was assessed in dedicated experiments in which the boundary flux (V_{loop}) was fixed and the plasma current was left floating.¹⁶⁴ The LH power, the total gas puffing, n_e , and V_{loop} were kept constant, while d_{PL} and the near gas puffing were varied from shot to shot. In these conditions, a change in the

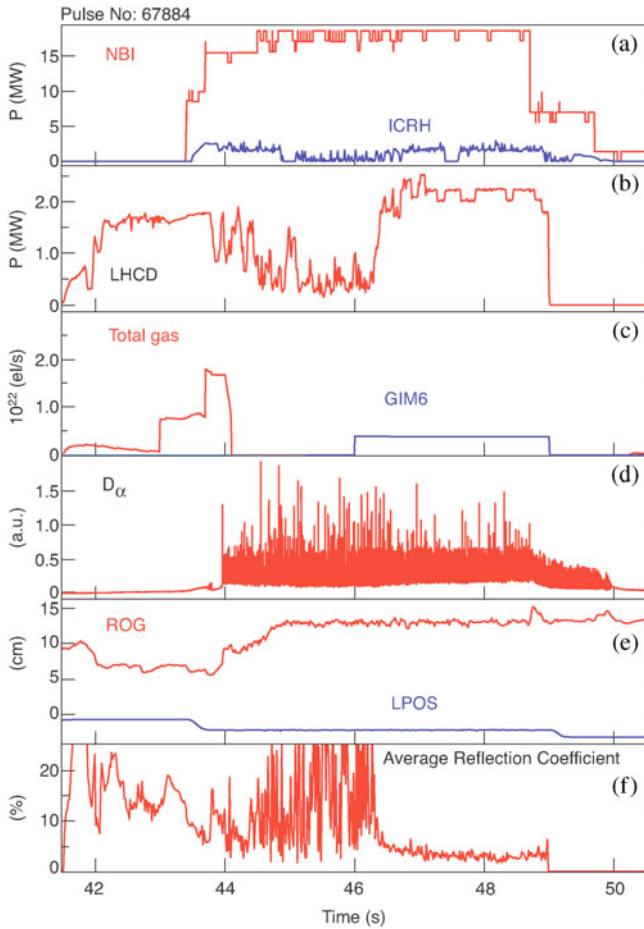


Fig. 29. Evolution of (a) NBI and ICRF power, (b) LH power, and (c) total gas and gas from the near gas pipe GIM6. Time shown here corresponds to valve opening. (d) D_α signal, (e) plasma-limiter distance and launcher position relative to the limiter, and (f) average reflection coefficient for pulse 67884 (with D_2). From Ref. 145.

plasma current would indicate a change in the current drive efficiency. The results from the experiment imply that the amount of LH power lost in the SOL varies little when increasing d_{PL} and gas puffing. Since the parasitic acceleration of electrons in front of the grill is a likely candidate for loss of power in the SOL, the surface temperature of the poloidal limiter magnetically connected to the grill was measured during this experiment. No difference in the temperature was observed when increasing d_{PL} and adding gas puffing, which supports this conclusion. Detailed analysis of this experiment is ongoing.

Modeling of the SOL plasma with gas puffing and P_{LH} has started using a version of EDGE-2D modified so that it can model plasmas with plasma-limiter distance up to 10 cm (Ref. 165). The effect of LH is taken into account in a simple way: It is assumed that a fraction of the LH power is lost in the SOL plasma, which leads to an

increase of T_e and hence enhances the ionization. (Contrary to the modeling mentioned in Sec. IV.C.1 (Ref. 148), no change in the particle transport is assumed.) To reproduce the measured increase in the far $n_{e,SOL}$, both gas puffing and an increase in $T_{e,SOL}$ (assumed to be due to P_{LH} lost in the SOL) are necessary (Fig. 30).

IV.C.4. Effect of ICRF on LH Coupling

The ICRF antennas being magnetically connected to the LH launcher affects LH coupling (mainly ICRF antenna B, since it is situated very near the LH launcher, as seen in Fig. 24, but also antenna A in some configurations).¹⁶⁶ Usually, adding ICRF power during LH degrades coupling, and the effect is worse at higher ICRF power or for ICRF monopole or $-\pi/2$ phasing, compared to dipole or $+\pi/2$ phasing. The LH coupling is affected differently on the different rows of the launcher and also varies toroidally along the rows, suggesting three-dimensional (3-D) modifications of the SOL plasma. These observations are consistent with the presence of rf sheaths modifying $n_{e,SOL}$ (for example, see Ref. 167). Of importance is that LH coupling in these conditions can be improved by puffing D_2 near the launcher, sufficiently for routine operation in JET experiments in 2006 and 2007

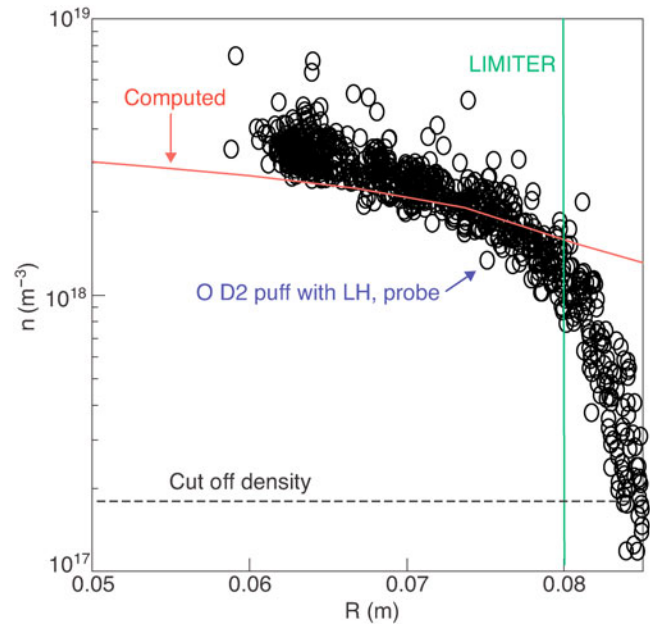


Fig. 30. Electron density profile (circles) measured by the reciprocating probe, for pulse 58667 at 4.8 s, with D_2 puffing rate = 8×10^{21} e/s. The curve shows the computed data, puffing rate = 1×10^{22} e/s, heating 300 kW in the slab between 2 and 4 cm from the separatrix (which is equivalent to 21.5 kW in the 3-D flux tube in front of the LH launcher). Plasma density at the separatrix is 1×10^{19} m^{-3} in the modeling. From Ref. 165.

with ICRF phasing +90 and dipole but not sufficiently for monopole or $-\pi/2$ phasing. This is also an issue for ITER if the LH antenna (assuming that an LHCD system is installed in ITER) is placed near the ICRF antenna.

IV.D. LHCD Efficiency and Other Physics Issues

IV.D.1. Operation Near to Fully Noninductive Current Drive

Nearly fully noninductive current drive with LHCD alone has been achieved in X-point configuration with plasma current I_p between 0.7 and 3 MA, line average electron density $\bar{n}_e < 2.0 \times 10^{19} \text{ m}^{-3}$, and high toroidal magnetic field, $B_T > 3 \text{ T}$, in order to permit a good penetration of the wave toward the plasma center. The resistive part of the surface loop voltage V_{res} is derived from measurements of the poloidal magnetic flux at different poloidal locations. The inductive contributions arising from varying magnetic energy are taken into account as $V_{res} = V_{loop} - I_p^{-1}(\frac{1}{2} \times LI_p^2)$, where L is the plasma inductance, I_p the plasma current, and V_{loop} the total surface loop voltage.¹³⁸ Full replacement of the plasma current is obtained when V_{res} is zero. This is shown in Fig. 31 for a 3-MA discharge. When full current replacement is obtained, the current drive efficiency can be defined as

$\eta_{CD} = \bar{n}_e I_p R_0 / P_{LH}$, where R_0 is the plasma major radius at the magnetic axis. For line-averaged electron density typically above $1.1 \times 10^{19} \text{ m}^{-3}$, the current drive efficiency increases with electron temperature up to a volume-averaged temperature of $\langle T_e \rangle \approx 2 \text{ keV}$ and reaches $\eta_{CD} = 0.26 \times 10^{20} \text{ m}^2 \text{ A/W}$. In this range, the experimental and calculated efficiencies are in good agreement.¹⁶⁸ The LHCD efficiency in JET has been found to fit a global scaling with the averaged electron temperature as shown in Fig. 32 (Ref. 169). However, although this scaling encompasses some physics, it has to be taken with caution since the damping of the LH wave depends on local parameters and the more recent estimates of LHCD efficiency rely on simulations. At low electron density, lower current drive efficiency is observed experimentally with a negative toroidal electric field being produced, especially at high LH power ($P_{LH} > 4 \text{ MW}$). This has been attributed to local overdriving of the current.¹³⁸ In such conditions, a negative electric field inside the plasma is produced that tends to decelerate the LH-produced suprathermal electrons, thereby reducing the current drive efficiency.

When a better coupling was found by injecting local gas close to the launcher, it was observed that the LHCD efficiency was not, or at least very little, affected by a large launcher-plasma distance and the amount of gas used. As discussed in Sec. IV.C, this implies that only a small amount of LH power was lost in the SOL for ionization of the gas in front of the launcher.

The LH power deposition and driven current profiles have been studied with the fast electron bremsstrahlung

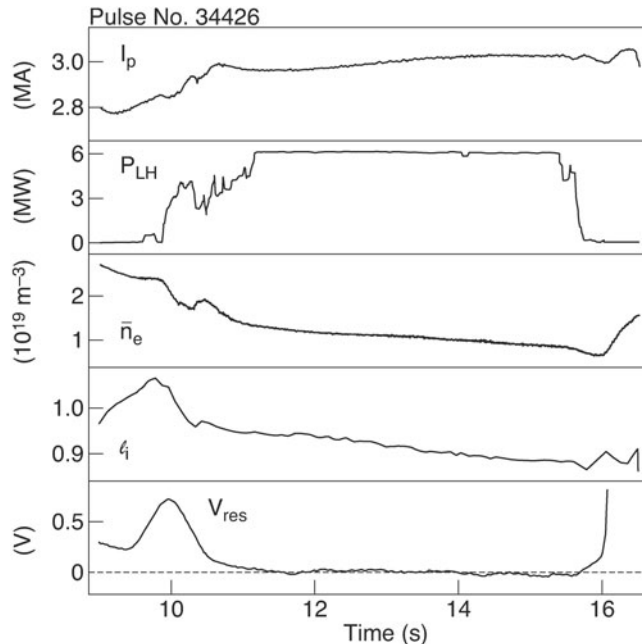


Fig. 31. 3-MA discharge near to 100% noninductive current drive with LHCD. (a) plasma current, (b) LH power, (c) line-averaged n_e , (d) internal inductance l_i , and (e) resistive part of the surface loop voltage V_{res} . The inductive contributions arising from varying magnetic energy are taken into account. From Ref. 138.

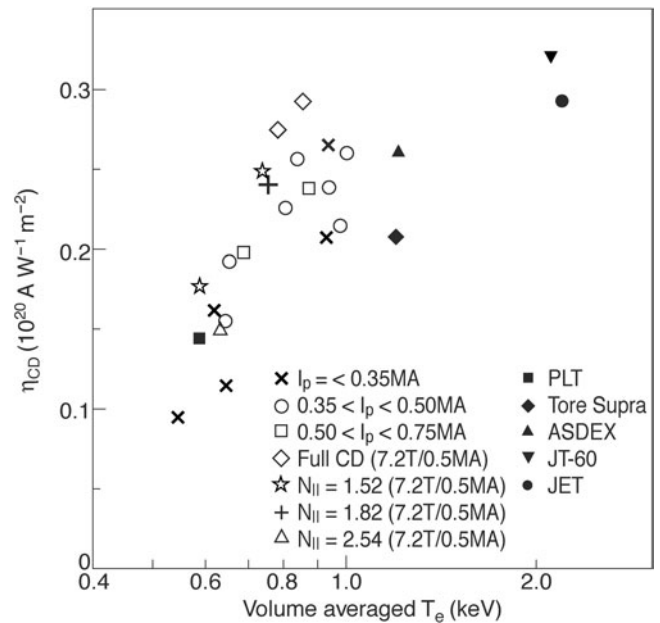


Fig. 32. LHCD efficiency in several machines as a function of the averaged electron temperature. From Ref. 169.

(FEB) diagnostic,^{170,171} which is the tool for determining the LH deposition profile. This diagnostic provides information about the location and energy distribution of the fast electrons, created by Landau damping of the injected LH waves. The FEB diagnostic detects hard X-rays with energy between 133 and 400 keV in four energy windows along 10 horizontal and nine vertical lines of sight. Abel inversion of the line-integrated brightness profiles yields the local emissivity as a function of the normalized poloidal flux. A limitation of the diagnostic is that it gives reliable data only in discharges with low neutron yield; i.e., it cannot be used during high-power NBI or ICRF heating. The fast electron distribution function and LH power deposition were modeled with the ray-tracing and Fokker-Planck code developed at the time in JET (Ref. 168). The code uses experimental profiles of electron density and temperature. The plasma equilibrium is obtained from the magnetic reconstruction code EFIT (Ref. 172). In the modeling calculations, a large number of rays are launched from different poloidal angles, representing the poloidal extent of the grill, and with a range of initial $n_{||}$ that covers the main lobe of the launched $n_{||}$ spectrum, as calculated by the SWAN code.¹⁴⁸ The code also allows calculation of the hard X-ray emission from the suprathermal electrons, which can then be compared with the measured FEB emission to validate the code. The propagation and absorption of the LH waves in conditions similar to the one of Fig. 31 are characterized by multipass absorption; i.e., the wave encounters many reflections at the plasma boundary before it is absorbed. This process can change the parallel refractive index of the wave considerably. Analysis of FEB profiles have been carried out in a wide range of plasma parameters: plasma current $I_p = 0.7$ to 3 MA, toroidal magnetic field $B_T = 1.8$ to 3.4 T, line-averaged electron density $n_e = 0.7 \times 10^{19}$ to $4.0 \times 10^{19} \text{ m}^{-3}$, and volume-averaged electron temperature $\langle T_e \rangle = 0.5$ to 3.0 keV. An example of ray-tracing calculations carried out with different combinations of magnetic equilibria and profiles is presented in Fig. 33a, showing the Abel-inverted FEB profiles for 2- and 3-MA discharges, normalized to the electron density. This is equivalent to a current profile. Figure 33b and 33c show the LH current profile and the power deposition profile from the ray tracing and Fokker-Planck code that are in reasonable agreement.

The effect of plasma parameters on the absorption of the LH power in the plasma was studied in Ref. 173, based on the changes in stored energy following LH switch-on or switch-off. This analysis showed that the amount of LH power absorbed decreases with the electron density, with 100% absorption at low line-averaged density ($n_e < 1 \times 10^{19} \text{ m}^{-3}$) but as little as 25% absorption for $n_e > 3 \times 10^{19} \text{ m}^{-3}$. The absorption coefficient also decreased with the magnetic field. The results were in agreement with predictions of the LH wave accessibility and suggested that this was the main factor for determining the power absorption.

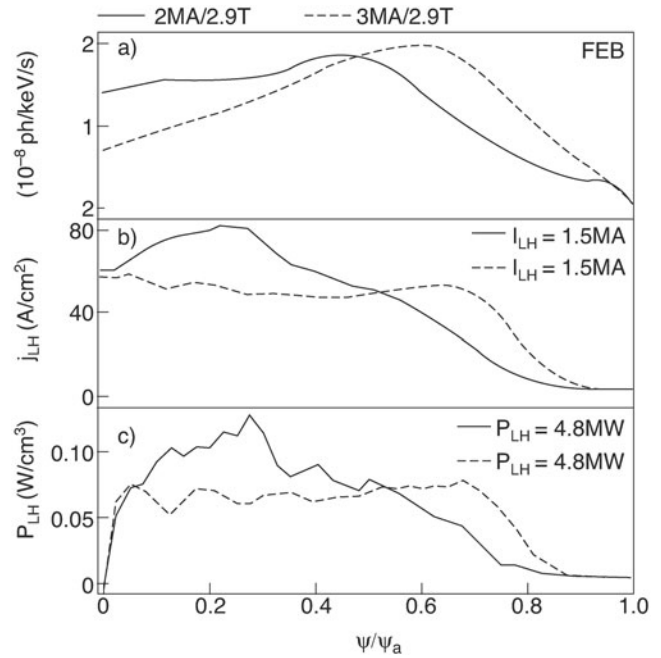


Fig. 33. Comparison of (a) experimental FEB profiles for discharges 30542 (2 MA) and 30505 (3 MA) and comparison of (b) LH-driven current profiles and (c) LH power deposition profiles from ray-tracing calculations for the 2- and 3-MA equilibria, using the density and temperature profiles of discharge 30505. From Ref. 138.

In the early experiments¹⁷⁴ it was found that synergistic effects with the ICRF FW can further accelerate the fast electron population to high velocities, thus increasing the current drive efficiency. This was attributed to the mode conversion to an electron Bernstein wave in some specific conditions. Since such conditions were difficult to reproduce on other machines, particularly in terms of location of the ICRF resonance and of the damping of the LH wave, the study of these synergistic effects was not pursued.

The evolution of the current profile during long (> 10 -s) LHCD pulses as shown in Fig. 26 has been modeled with the JETTO transport code,¹⁷⁵ using the LH current profile from ray-tracing calculations as input. It was found that the predictive transport code modeling can well reproduce the behavior of the internal inductance and the surface loop voltage.¹⁵²

IV.D.2. Counter-Current Drive Experiments

Since fixed mechanical phase shifters inside the multijunctions create the phase difference between the small waveguides of the launcher, the LH wave provides co-current drive in the configuration normally used in JET. Recent experiments¹⁷⁶ with reversed B_T and I_p in JET

have given a rare opportunity to investigate the LH wave current drive efficiency in the direction counter to I_p . The experiments were done with 2.9 MW of LH power, during flattop $I_p = -1.45$ MA, $B_T = -3.1$ T, and with central density $n_{e0} = 1.6 \times 10^{19} \text{ m}^{-3}$. The results were compared to those in plasmas with normal B_T and I_p , with similar but not identical plasma parameters ($I_p = 1.3$ MA and $P_{LH} = 3.3$ MW). The change in surface loop voltage is smaller in the counter-current case, but the core T_e is higher. The evolution of the internal inductance l_i reveals that the current profile is evolving differently in the co-current and counter-current cases. l_i decreases when P_{LH} is applied in the co-current case, indicating that the current profile is broadening. In contrast, l_i increases in the counter-current case, which indicates that the current profile is becoming more peaked. In addition, sawteeth are observed with counter-LH current, indicating that q has reached 1. No $q = 1$ sawteeth are seen in the shot with co-LH current. The code CRONOS (Ref. 177), which couples the diffusion equation to a 2-D equilibrium code, has been used to estimate the amount of LH current driven in the counter-current and the co-current cases. To reproduce the measured T_e , internal inductance l_i , and surface loop voltage in the counter-current case, a current drive efficiency of the same order of magnitude as the one found in the co-current case is required, with a central, wide, LH power deposition. However, the LH power deposition in this case is off-axis, at $r/a \sim 0.4$.

IV.D.3. Electron ITBs

When LHCD was used in the current ramp-up phase, with ramp rate typically 1 MA/s and low central density ($n_{e0} < 1.5 \times 10^{19} \text{ m}^{-3}$) and using LH power between 1 and 3 MW, a peaking of the electron temperature profile and central electron temperature reaching 10 keV was observed.¹⁵² In these particular experiments the launcher was retracted by 5 to 10 mm in the shadow of the poloidal limiters and local gas injection was used to obtain good coupling. The evolution of the plasma parameters and the temperature profiles is shown in Fig. 34. The q profile obtained from the equilibrium reconstruction has shown a broad current profile with negative magnetic central shear. The increase in T_e was attributed to the establishment of an ITB with improved central electron confinement. Simultaneously, increases in both central ion temperature and neutron yield were observed, indicating that the confinement of ions, as well as electrons, was improved. The profile of the LH-driven current, as given by the Abel inversion of the hard X-ray emission profile from the FEB camera, was peaked at approximately mid-radius. Preliminary transport code calculations¹⁵² have been carried out for the discharge shown in Fig. 34. The modeling has shown that the effective heat conductivity was in the order of $0.1 \text{ m}^2/\text{s}$ inside $r/a < 0.4$ during the whole LH phase. As the LH current profile gradually shifts toward the plasma center and more LH power is

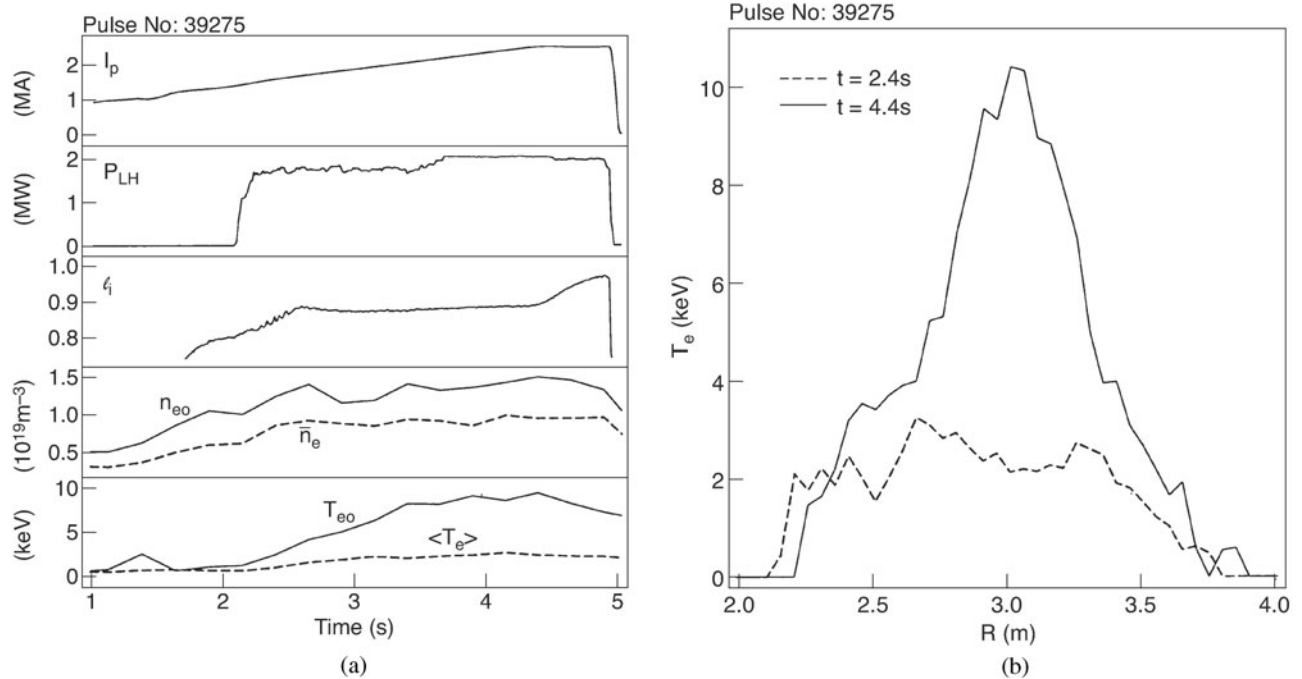


Fig. 34. Electron ITB with LHCD only. (a) Time traces of the main parameters and (b) electron temperature profiles from the Thompson scattering diagnostic. From Ref. 152.

deposited inside the region of improved confinement, the peaking of the electron temperature profile takes place. Quantitatively, however, the experimental profiles of the LH current and LH power deposition are too hollow, and more centrally peaked profiles were needed in order to reproduce the observed heating in the plasma center with the transport code.

It has been found¹⁷⁸ that for the same LHCD power, the ITB presence and width in the ramp-up phase depend on the plasma parameters early in the discharge. In particular, shots with lower plasma current at plasma initiation (i.e., in the first few hundred ms of the discharge) do not exhibit ITBs. Also, plasmas with lower electron density have a wider ITB. In plasmas with reproducible initial parameters, it is possible to move the electron ITB location outward by increasing LHCD power¹⁷⁸ (Fig. 35). In effect, this corresponds to changes in the current profile, which has been exploited in the development of advanced scenarios, as discussed in Sec. IV.E.

IV.D.4. Damping of the LH Wave on Energetic Ions

As discussed in the introduction, LH waves can interact with energetic ions via Landau damping of the n_{\perp} spectrum. It is important to assess the magnitude of such an effect experimentally since damping of the LH wave on energetic particles in fusion devices, such as alphas,

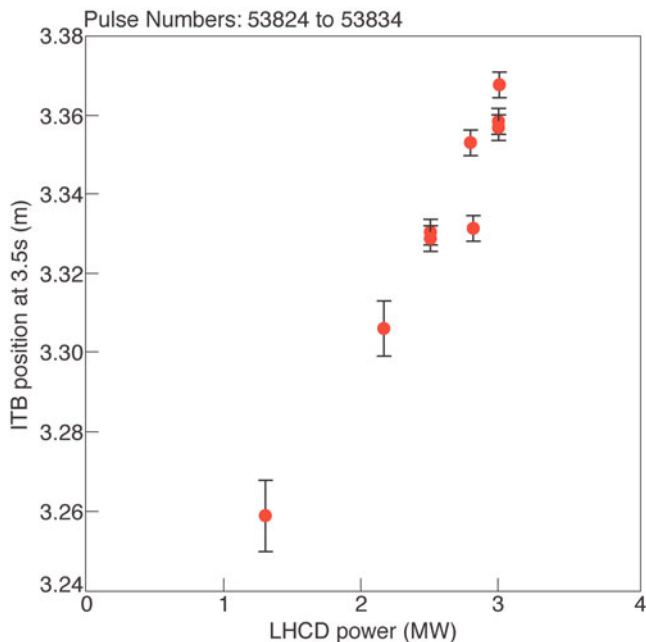


Fig. 35. Position of the ITB as a function of the LHCD power for shots with reproducible plasma initiation. (Note: The variation in Shafranov shift measured by soft X-rays is <3 cm for the extreme powers and therefore is too small to explain the change in the ITB position). From Ref. 178.

fast ions from NBI (1 MeV in ITER), and fast ions accelerated by ICRF power, is predicted to be important under certain conditions. Although the LH power might not be lost, this can be detrimental for current drive efficiency. Specific studies have been made at JET to try to estimate the power coupled from LH waves to the ICRF-induced energetic ions. Initial results were reported in Ref. 179 and indicated that only a few percent of the LH power was coupled to the energetic ions. More recent analysis is reported in Ref. 180, with the energy distribution function of the high-energy protons during minority ICRF heating of protons in deuterium plasmas in the range $0.3 \leq E$ (MeV) ≤ 1.1 from NPA measurements. Their distribution function is strongly anisotropic for energies higher than the critical energy at which the proton-electron and proton-ion slowing-down time are equal. During simultaneous LHCD and minority ICRF heating, the NPA measurements showed evidence of coupling of LH power to the high-energy anisotropic proton population. The coupling was deduced for driven as well as for slowing-down protons. The observations indicate that up to 30% of applied LH power was coupled to the protons, the interaction taking place in the whole energy range of the measurements. This suggested that the n_{\perp} of the LH wave was extending up to 40, twice the value given by conventional model calculations in JET of the LH dispersion relation¹⁷⁹ predicting only 5 to 10% of the LH power coupled to the high-energy proton population. By solving in Ref. 180 the hot-plasma dispersion relation in the LH range of frequencies for plasmas containing high-energy minority anisotropic protons and electrons, it was found that multiple solutions of the dispersion relation with $n_{\perp} > 40$ exist in the plasma center due to the presence of the protons. These hot-plasma modes give a 20 to 40% damping of LH input power onto the protons by perpendicular Landau damping. However, there are some prospects that these hot-plasma modes can be avoided, thus reducing damping of LH power to the protons to 5 to 10%. Work is still in progress to give a more complete physical interpretation and to study the interaction of LH waves with charged fusion products in more reactor-relevant conditions.

IV.E. LHCD as a Tool

IV.E.1. Sawtooth Control of Hot-Ion H-Modes

In the hot-ion H-mode scenario, which has been used to produce the highest transient fusion yield^{181,182} (see Sec. III.D), high-power NBI is applied to a low-density, high-triangularity divertor plasma. An ELM-free H-mode is produced in which the central ion temperature can reach above 20 keV and exceed the central electron temperature by a factor of 2. The high fusion performance phase lasts for 1 to 2 s and is then terminated by a deterioration of the confinement, which is associated with a variety of MHD activities, including giant ELMs,

sawteeth, and outer modes.¹⁸³ To investigate the effect of current profile modification and to improve the performance, a 5-s LHCD pulse at $P_{\text{LH}} = 5$ MW was applied in a 3-MA plasma at low density ($n_e \approx 1.0 \times 10^{19} \text{ m}^{-3}$). During LHCD the internal inductance decreased and the sawteeth were suppressed. The hot-ion H mode was then produced by high-power NBI ($P_{\text{NBI}} \approx 10$ MW). A first set of experiments was not successful because the reduction in l_i and broadening of the current profile resulted in the decrease of edge shear and triangularity and a subsequent degradation of the hot-ion H-mode. A second experiment was carried out in a modified plasma configuration that yielded relatively high edge shear, even at low internal inductance, resulting in longer ELM-free periods.¹⁸⁴ Figure 36 shows the result of the second experiment. In the discharge with LHCD (discharge 35006), the sawteeth were stabilized during the LHCD phase, but a small sawtooth was observed during the NBI phase. In the discharge without LHCD (discharge 35010), large sawteeth were present during the high power phase. In the pulse with NBI only, a large ELM terminated the high performance phase and the neutron rate decayed rapidly afterwards. With LHCD for q profile control, the high performance phase was ended by weak MHD activity, followed by saturation in the neutron rate instead of decay. No attempts at large statistics in these experiments have

been possible. The optimization studies of the q profile variation with LHCD before hot ion H modes with higher NBI power (18 MW) remain to be done.

IV.E.2. The Role of LHCD in the Optimized Shear Configuration Development

Improved core confinement and high fusion yield have been obtained in the so-called optimized shear scenario in JET plasmas with weak magnetic shear,^{5,185} allowing the record neutron yield to be achieved in D-D plasmas in JET (Ref. 186) as well as 8.2 MW of fusion power in D-T plasmas. Crucial for the performance in these discharges is the q profile, which is tailored early in the discharge by using an initial fast current ramp rate (1.5 MA/s), followed by a slower ramp (0.4 MA/s) up to 3 MA (Ref. 187). Applying LHCD during the current ramp-up phase can make further modification of the current profile. This phase is called the prelude phase. The LH power followed a waveform for the requested coupled power by using the real-time power control system. From the equilibrium reconstruction, which is accurate in the region $r/a > 0.5$, the q profile was found to broaden and the region of low shear to increase when LHCD was applied. Contrary to the case without LHCD, a prompt triggering of the ion ITB following the application of high power (NBI and ICRF) was obtained with a short LHCD phase at 1 MW applied immediately after the current formation, followed by ICRF to freeze the q profile and high-power injection at 5.0 s in the discharge (Fig. 37). In the scenario that has been used in the D-T experiments in JET, the main purpose of LHCD was to assist in the plasma breakdown and plasma formation. Until 1999 in JET, the best experimental results were obtained in plasmas with this short LHCD preheat. Further development was dependent on the progress of LHCD coupling, in particular during the high-performance phase, which is discussed in the following paragraphs.

IV.E.3. LHCD as a Tool to Change Plasma Current Profile in Noninductive Steady-State Scenarios

As discussed in Sec. IV.D.2, launching LH waves in the plasma current ramp-up phase contributes to the generation of a core region of negative magnetic shear, in some cases assisted by the formation of an electron energy ITB, which, in the presence of strong electron heating at low density, raises the central electron temperature so as to strongly inhibit the penetration of plasma current to the core. In the experiments reported in this paragraph, the LH power was normally switched off at the beginning of the main heating phase (NBI and ICRF). In a series of experiments, starting conditions and LH power were varied to determine the range of profile configurations that it was possible to achieve and the consequence on ITB formation when high power (NBI + ICRF) was applied.¹⁸⁸ For these experiments, the q profiles have been

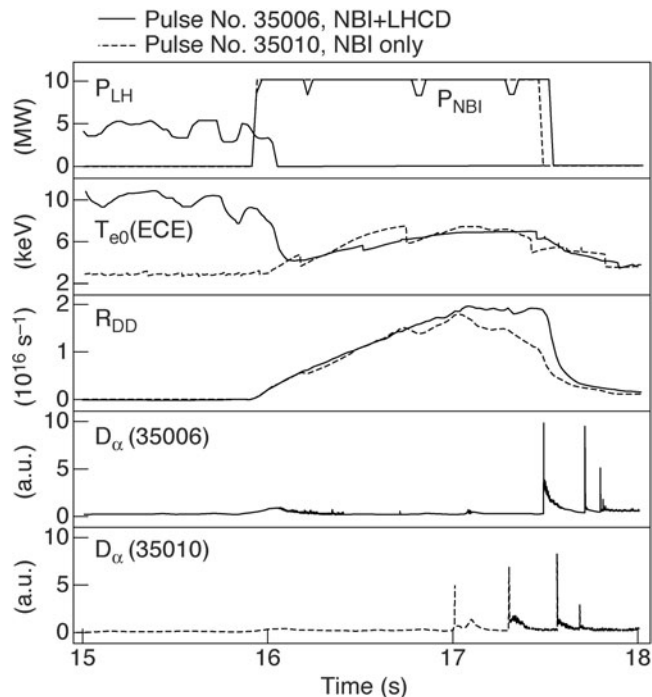


Fig. 36. Evolution of sawtooth activity, neutron rate, and D_α signal in hot-ion H-modes with preceding LHCD (discharge 35006) and without preceding LHCD (discharge 35010). The full length of the LH pulse is not shown. From Ref. 138.

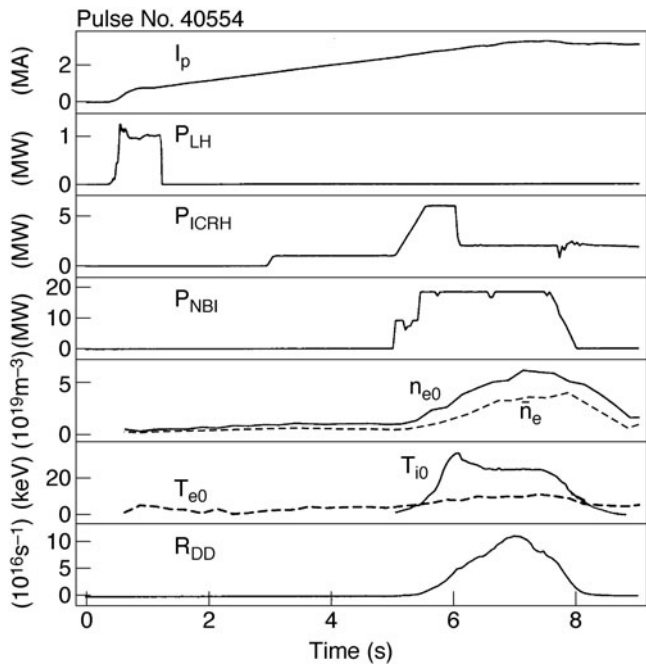


Fig. 37. Scenario for high fusion yield in the optimized shear experiments. From Ref. 138.

determined using the EFIT equilibrium reconstruction code¹⁷² constrained by motional stark effect (MSE) measurements.¹⁸⁹ The results are consistent with analysis using measurements from a far-infrared polarimeter, but since the resolution of the MSE instrument allows a better determination of the magnetic shear in the plasma core, the MSE measurements are used in the following. During the main heating phase, the use of several overlapping neutral beams in the diagnostic line of sight complicates the MSE measurement, so a reduced power phase was included at the start and the end of the main heating pulse to optimize the measurements. The uncertainty in the determination of the absolute magnitude of q has been estimated to be of order $\pm 15\%$. As can be seen in Fig. 38, the magnetic shear in the plasma interior was varied in a very large range from small and positive in the ohmic preheat case, through “weakly” negative with low-power LHCD, to “highly” negative (extremely high central q , attributed to the formation of a current hole; see below) when the LHCD prelude was accompanied by an optimized plasma initiation sequence. The experimental technique to obtain this third class of q profile is described in Ref. 189. The narrow minimum in the q profile shape in this case is thought to result from the localization of LH power deposition, and hence of current drive, at the ITB because of the high T_e it leads to. This feature, described in Ref. 190, quickly diffuses away when the LHCD is switched off. This capability of LHCD to vary the current profile and the magnetic shear, which plays a key role in the development of advanced tokamak scenarios, has been extensively used on JET from 2001 onward.

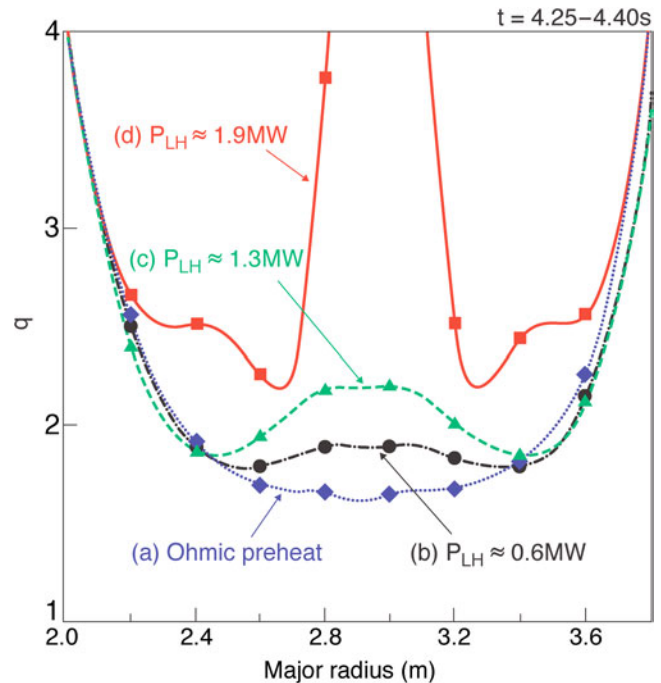


Fig. 38. Comparison of target q profiles prepared with varying LHCD prelude and plasma initiation conditions, which provide a “ q profile scan” for similar high-power main heating conditions. From Ref. 188.

The so-called current hole configuration formed by applying LHCD in the ramp-up phase is described in Ref. 190. Simultaneous current ramping and application of LHCD have produced a region with zero current density within measurement errors in the core ($r/a \sim 0.2$) of JET tokamak optimized shear discharges. The reduction of core current density is consistent with a simple physical explanation and numerical simulations of radial current diffusion including the effects of LHCD. However, the core current density is clamped at zero, indicating the existence of a physical mechanism, not yet identified, that prevents it from becoming negative. The energy confinement time in these current hole discharges is quite high. They provide an interesting regime to study various physics processes in conditions of near-zero poloidal magnetic field.

IV.E.4. Toward Fully Noninductive ITB Plasmas with LHCD

Thanks to the progress in techniques to improve the LHCD coupling, as described in Sec. IV.C, it has been possible to maintain the LH power at significant levels during the high-power ELMy H-mode phase in order to further slow down the current profile evolution and hence sustain the q profile favorable for the existence of ITBs. By injecting CD_4 gas near the launcher in the high-power phase of the plasma, with the launcher positioned 1 cm

behind the poloidal limiter at an average distance from the plasma separatrix of 5.5 cm, successful coupling of the LH waves up to 3 MW during the H-mode phase with reflected power in the range of 5% has been achieved.¹⁷⁸ One of the longest-lived ITB plasmas,^{160,161} with LH power in addition to NBI and ICRF power, combining an ELMy H-mode edge (type III) and core transport barrier, sustained with a loop voltage approaching zero at a plasma current plateau of 2 MA, is shown in Fig. 39 (discharge 53521, $q_{95} = 5.5$, $H_{ITER-89P} = 2$, $\beta_P = 1.1$, and $\beta_N = 1.7$ at $B_T = 3.45$ T). The discharge shown in Fig. 39 is not exactly at zero loop voltage; the time-averaged loop voltage is of the order of 0.1 V, corresponding to a flux consumption at the plasma boundary of 0.8 Wb during the high-power phase. A full current drive discharge has

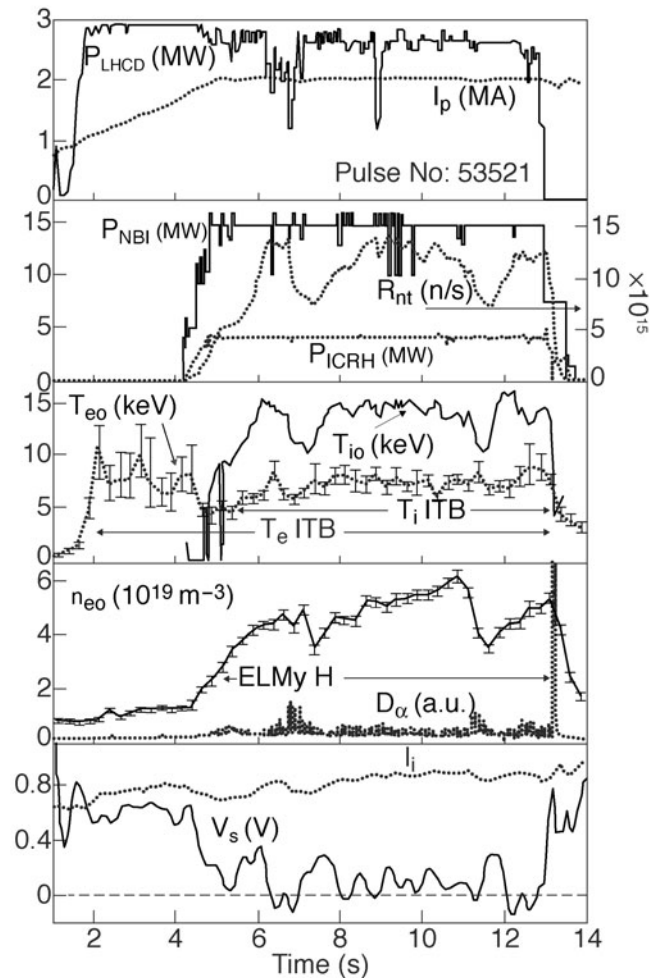


Fig. 39. Evolution of the main parameters of a highly noninductive discharge (53521): LHCD power (P_{LHCD}), plasma current (I_p), NBI (P_{NBI}), ICRF powers (P_{ICRH}), neutron yield (R_{nt}), central ion (T_{i0}) and electron (T_{e0}) temperatures, central electron density (n_{e0}), D_α emission, internal inductance (l_i), and plasma surface voltage (V_s). From Ref. 161.

been obtained at lower plasma current but for shorter times due to technical problems.¹⁶¹

In the discharge shown, all the heating and current drive systems available at the time at JET were used simultaneously at almost their full power and the injected energy was 193 MJ. The duration of this discharge was close to the JET technical operational limits fixed by the maximum duration of application of the full NBI power and the high toroidal field operation at $B_T = 3.45$ T. The electron ITB is maintained for 11 s from the LH preheat phase up to the preprogrammed end of the power waveforms. This duration corresponds approximately to 37 energy confinement times. The ITB observed on the ion temperature, electron density, and toroidal rotation profile is sustained during the whole high-power phase (≈ 8 s). During the LH preheat phase, the ITB on the electron temperature profile is located at a normalized radius of $\rho/\rho_{max} = 0.2$ to 3 (Ref. 178) and then expands radially up to 0.45 in the high-beta phase. The target q profile at $t = 4.2$ to 4.3 s has negative shear with $q_{min} \approx 3$ at $\rho/\rho_{max} \approx 0.5$. The use of high-power LHCD and the resulting high electron temperature have produced a freezing of the q profile evolution. In particular, the location and value of q_{min} allows maintaining the ITBs inside the midplasma radius, i.e., in the weak or negative magnetic shear region. The loss of confinement at 11.1 s has been attributed to a radiative collapse, the ITB recovering rapidly its characteristics. The likely cause of the collapse is an interaction between the plasma and the inner wall, located in the upper part of the vacuum chamber,¹⁹¹ due to an increase of the upper triangularity at high beta, while the position of the X point is kept fixed thanks to the feedback control system.

Use of LHCD in the development of noninductive steady-state scenarios has progressed following the installation of a new divertor in 2005 and a higher NBI heating capability.¹⁹² Noninductive regimes with ITBs have been developed at $q_{95} \sim 5$ ($I_p \sim 1.9$ MA and $B_T \sim 3.1$ T), closer to the ITER shape, with high value of triangularity by applying up to 27 MW of additional heating power (20 MW of NBI, 5 MW of ICRF power, and 2 MW of LHCD, the LHCD power being launched in the presence of type I ELMs). A noninductive current fraction of up to 70% was achieved at the peak of the performance.

IV.E.5. LHCD in Real-Time Current Profile Control Development

Since 2001, JET has developed a comprehensive set of real-time diagnostics, control tools, and simulation facilities for the operation of advanced tokamak scenarios. Steady-state noninductive operation with ITBs and high fraction of bootstrap current is very challenging (for instance, see Ref. 193). Among the recent tools developed in JET, the current profile measurements have dramatically enhanced the experimental work on the

integration of advanced tokamak scenarios. In particular, techniques to control the q and pressure profiles simultaneously in real time have been developed, and specific model-based multivariable techniques have been proposed.¹⁹⁴ This procedure was first applied to the control of a predefined q profile of five points ($r/a = 0.2, 0.4, 0.5, 0.6,$ and 0.8) with one actuator only, namely, the LH power.¹⁹⁵ The corresponding experiment was performed during an extended LHCD phase of 15 s ($I_p = 1.3$ MA, $B_T = 3$ T, and $n_e = 2.5 \times 10^{19} \text{ m}^{-3}$). The q profile has successfully reached the required shape and was maintained for about two resistive times.¹⁹³ After this first encouraging result, the specific techniques developed at JET were applied to the q profile control using three actuators (i.e., LHCD, NBI, and ICRF). Figure 40a shows the resulting feedback waveforms together with the demand produced by the controller and the time traces of q at $r/a = 0.5$. Figure 40b illustrates the evolution of the q profile during the controlled phase (from 7 to 13 s). Between 7 and 11 s the q profile falls sharply and then rises after 11 s toward the reference points as the actuators start to act on the current density diffusion. This demonstrates that the selected gains of the controller were ad-

equate and the technique effective on a timescale that approaches the current diffusion timescale.¹⁹⁶ The analysis of the deposition of the noninductive currents (LHCD at midradius and NB current drive in the plasma core) indicates that the q profile is controlled in effect at two different radial points. Such experiments, in which LHCD plays a key role, represent a significant step for the development of a high-beta noninductive steady-state scenario.

IV.E.6. Role of LHCD in Hybrid Scenario Development

The goal of the development of the so-called hybrid scenario is to provide very long pulse operation in ITER with sufficient fusion gain ($Q > 5$; for instance, see Ref. 197 and references therein). Successful demonstration of such discharges has been achieved in plasma configurations with flat current profiles with central q near 1. Interestingly, in this case $m = 1$ MHD activities can be present but do not prevent the discharge to reach high beta values. In the 2003 campaigns, a detailed study of the hybrid regime was started in JET. One of the key elements in achieving stationary discharge is a controlled

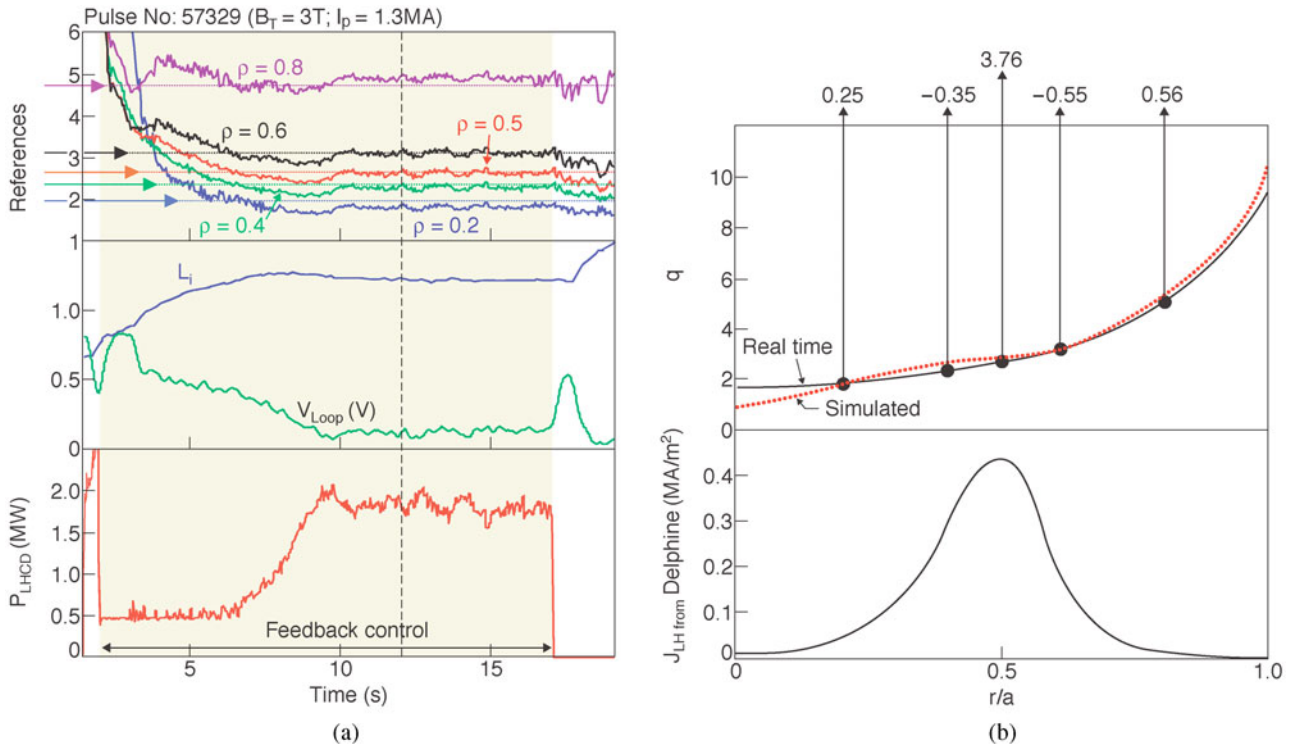


Fig. 40. (a) Real-time control of the q profile with LHCD only. In the top panel, the safety factor time traces are compared with the q reference used in the controller. In the center panel, the l_i and loop voltage (V_{loop}) demonstrate that this discharge reaches steady state. (b) Comparison of the q profile measured from real-time data and the simulation from the CRONOS code,¹⁷⁷ which includes the ray-tracing code DELPHINE (Ref. 206), at 12 s [indicated by the dotted line in (a)]. The five filled circles show the reference q values used in this experiment. The gains of the control matrix are displayed at the top of the graph. From Ref. 193.

q profile stable above or close to unity as obtained in ASDEX Upgrade.¹⁹⁸ Given the much longer resistive time constant in JET (typically five times longer than in ASDEX Upgrade), active tailoring of the q profile is required, and this is achieved with 0.5 to 1.5 MW of LH power. In this way, the q profile could be tuned so that a low magnetic shear close to $q = 1$ is obtained, almost independently of the machine start-up conditions. A typical discharge of this type is shown in Fig. 41 for a low-triangularity configuration with $B_T = 1.7$ T and $I_P = 1.4$ MA. The current ramp-up phase in L-mode is used to establish the target magnetic configuration and q profile. High NBI power is applied when the q profile approaches $q = 1$ in the plasma center. Since these early experiments, further optimization of hybrid scenarios has taken place. In particular, LHCD, at a power level of 1 to 2 MW, has been used during the high-power phase in combination with ICRF power to produce rf-dominated hybrid scenario discharges to control the possible evolution of the current profile during the stationary phase.¹⁹⁹ More recently, as described in Sec. IV.C, coupling during the high-power phase of hybrid plasmas at 1.7 T has been optimized, and more than 3 MW of LH power was coupled. A comparison of $n_{||} = 1.8$ and 2.3 was performed, in

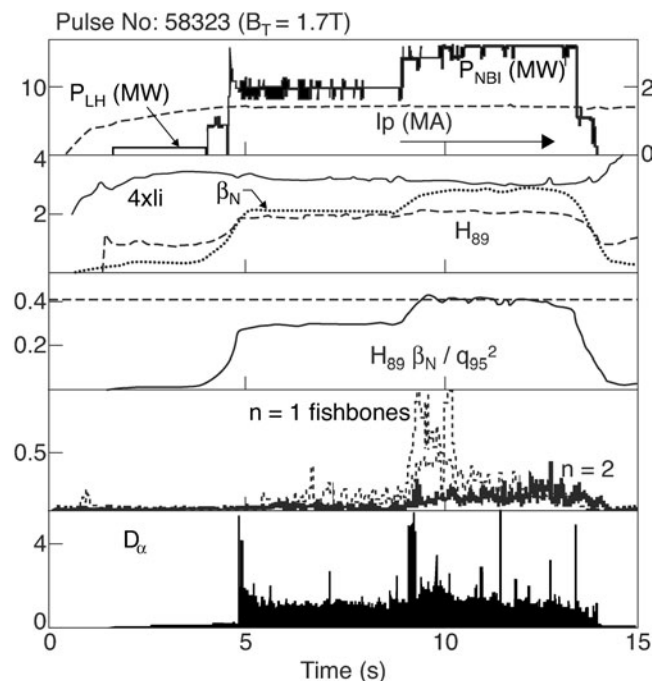


Fig. 41. Hybrid scenario achieved in JET from the JET-ASDEX Upgrade identity experiment. LH power is used in the plasma ramp-up to broaden the target q profile above unity before the beam power is launched. This discharge reaches β_N of 2.8 (dotted line), close to the estimated ideal kink (dashed line) and a fusion figure of merit of 0.4 with low MHD activity. From Ref. 197.

view of optimizing the use of LHCD for future experiments in this scenario.¹⁶⁴ Despite the low B_T and relatively high n_e , which means that it is more difficult for the LH waves to access the plasma, modifications in the MHD modes observed indicate that the LH power is absorbed in the plasma. The detailed analysis of this experiment, including LH and transport modeling, is ongoing.

IV.E.7. LHCD for NTM Control

As described in the chapter on MHD stability studies on JET in this special issue, NTMs can lead to considerable deterioration of the plasma confinement. They are observed in plasmas at high β_N with monotonic q profile and with $q = 1$ surface in the plasma. This makes it a crucial issue for the ITER baseline scenario, and studies on how to prevent NTMs, or the sawteeth that can destabilize them, represent an active area of work on several machines. It is reported in Ref. 200 that by using LHCD before the high-power heating phase, in order to raise $q_0 > 1$ and lower the magnetic shear globally in the central plasma, it was possible to reduce the amplitude of the $m = 3, n = 2$ (3/2) NTMs or to modify the threshold of the 4/3 NTMs. As a result, better plasma performances were obtained. More recent experiments²⁰¹ showed that applying LHCD could also raise the threshold for 2/1 NTMs and suppress partially preexisting 3/2 NTMs. This paper also reports that LHCD was used extensively to raise $q_0 > 1$ and prevent sawteeth and large NTMs in JET 2006 experiments.

IV.F. Conclusions

Although the LHCD system in JET never delivered the total amount of power that was envisaged originally (about 75% in L-mode plasmas and 35% in H-mode plasmas), it has proved to be a key tool in JET experiments and, in particular, for the development of the operational scenarios envisaged for ITER, i.e., for advanced scenarios (current profile control) but also possibly for the baseline scenarios (MHD control). The LHCD system has therefore fulfilled its initial objectives as set up in 1986, as indicated in the introduction, i.e., to improve confinement with changes in current profile, although advanced scenarios were not anticipated at the time.

The LH coupling in JET behaves close to that expected from the modeling based on the 2-D linear coupling theory, when the real geometry of the multijunction is taken into account. However, there is evidence of non-linear effects taking place in the SOL plasma (parasitic power loss). The current drive efficiency obtained attains the best one observed on other machines.

The current drive capabilities of the LH wave have been exploited in many experiments in JET. It has become the preferred tool for performing the q profile required for establishing the so-called hybrid plasmas and

the ITB plasmas. It has also been used for preventing or modifying detrimental MHD activity. In addition, it has provided the off-axis current component required for sustaining the q profile needed for the ITB to persist, consistent with both the ITB location and the bootstrap current. Predictions for ITER have shown that LHCD can provide the current drive capabilities required for the advanced tokamak scenario²⁰² and the hybrid scenario.²⁰³

Importantly, JET experiments have demonstrated that it is possible to achieve good LH coupling in ITER-like conditions, i.e., with simultaneously large plasma-launcher distance, ELMy H-mode plasma, and high triangularity, provided near gas puffing is used, to control the local SOL n_e independently from the main plasma. With the physics learned and the experience gained over the years, it is felt that the design of the JET LHCD launcher, done in the 1980s, could be significantly improved so that much higher power could be launched in ITER-relevant scenarios as compared to today's JET capability.

REFERENCES

1. J. JACQUINOT et al., *Plasma Phys. Control. Fusion*, **27**, 1379 (1985).
2. J. JACQUINOT et al., *Plasma Phys. Control. Fusion*, **28**, 1 (1986).
3. J. JACQUINOT et al., *Philos. Trans. R. Soc. London, Ser. A*, **322**, 95 (1987).
4. J. JACQUINOT et al., *Plasma Phys. Control. Fusion*, **35**, A35 (1993).
5. C. GORMEZANO et al., in *Radio Frequency Power in Plasmas*, Savannah, Georgia, P. RYAN, Ed., AIP Conf. Proc., Vol. 403, pp. 3–12 (1997).
6. C. GORMEZANO, *Plasma Phys. Control. Fusion*, **40**, A171 (1998).
7. D. J. CAMPBELL et al., *Phys. Rev. Lett.*, **60**, 2148 (1988).
8. D. F. H. START et al., in *Proc. 19th EPS Conf. Controlled Fusion and Plasma Physics*, Innsbruck, 1992, Vol. 16C, pp. 897–904, EPS (1992).
9. E. RIGHI et al., in *Radio Frequency Power in Plasmas*, Oxnard, California, T. K. MAU, Ed., AIP Conf. Proc., Vol. 595, pp. 110–113 (2001).
10. V. P. BHATNAGAR et al., *Nucl. Fusion*, **39**, 353 (1999).
11. J. G. CORDEY et al., *Physica Scripta*, **T16**, 127 (1987).
12. V. P. BHATNAGAR et al., *Nucl. Fusion*, **33**, 83 (1993).
13. D. F. H. START et al., *Nucl. Fusion*, **39**, 321 (1999).
14. M. L. MAYORAL et al., in *Radio Frequency Power in Plasmas*, Park City, Utah, S. J. WUKITCH, Ed., AIP Conf. Proc., Vol. 787, pp. 122–129 (2005).
15. P. U. LAMALLE et al., *Nucl. Fusion*, **46**, 391 (2006).
16. F. G. RIMINI et al., *Nucl. Fusion*, **39**, 1591 (1999).
17. G. A. COTTRELL et al., *Nucl. Fusion*, **39**, 389 (1999).
18. G. A. COTTRELL et al., *Nucl. Fusion*, **39**, 2025 (1999).
19. J. PAMELA et al., *Nucl. Fusion*, **42**, 1014 (2002).
20. J. JACQUINOT, *Plasma Phys. Control. Fusion*, **30**, 1467 (1988).
21. A. KAYE et al., *Fusion Eng. Des.*, **24**, 1 (1994).
22. A. KAYE et al., in *Radio Frequency Power in Plasmas*, Savannah, Georgia, P. RYAN, Ed., AIP Conf. Proc., Vol. 403, pp. 389–392 (1997).
23. J. M. NOTERDAEME et al., *Fusion Eng. Des.*, **74**, 191 (2005).
24. R. H. GOULDING et al., in *Radio Frequency Power in Plasmas*, Palm Springs, California, R. PRATER, Ed., AIP Conf. Proc., Vol. 355, pp. 397–400 (1995).
25. J.-M. NOTERDAEME et al., in *Proc. 17th IAEA Conf. Fusion Energy*, Yokohama, Japan, IAEA-CSP-1/C, ISSN1562-4153, CDP/11 (1998).
26. I. MONAKHOV et al., *Fusion Eng. Des.*, **74**, 467 (2005).
27. F. DURODIE et al., *Fusion Eng. Des.*, **74**, 223 (2005).
28. D. F. H. START et al., *Phys. Rev. Lett.*, **80**, 4681 (1998).
29. M. J. MANTSINEN et al., *Plasma Phys. Control. Fusion*, **41**, 843 (1999).
30. L.-G. ERIKSSON et al., *Nucl. Fusion*, **39**, 337 (1999).
31. G. CORDEY et al., *Plasma Phys. Control. Fusion*, **39**, B115 (1997).
32. G. ERICSSON et al., *Rev. Sci. Instrum.*, **72**, 759 (2001).
33. M. TARDOCCHI et al., *Nucl. Fusion*, **42**, 1273 (2002).
34. J. R. WILSON et al., *Phys. Rev. Lett.*, **75**, 842 (1995).
35. C. K. PHILLIPS et al., *Phys. Plasmas*, **2**, 2427 (1995).
36. J. R. WILSON et al., *Phys. Plasmas*, **5**, 1721 (1998).
37. V. BERGEAUD et al., *Nucl. Fusion*, **40**, 35 (2000).
38. D. VAN EESTER et al., *Nucl. Fusion*, **42**, 310 (2002).
39. M. J. MANTSINEN et al., *Nucl. Fusion*, **39**, 459 (1999).
40. P. U. LAMALLE et al., in *Proc. 31st EPS Conf. Controlled Fusion and Plasma Physics*, London, United Kingdom, ECA Vol. 28G, EPS P-5.165 (2004).
41. V. G. KIPTILY et al., *Rev. Sci. Instrum.*, **74**, 1753 (2003).
42. V. G. KIPTILY et al., *Nucl. Fusion*, **45**, L21 (2005).
43. J. HEDIN et al., *Nucl. Fusion*, **42**, 527 (2002).
44. L. GIACOMELLI et al., in *Proc. 31st EPS Conf. Plasma Physics and Controlled Fusion*, London, United Kingdom, ECA Vol. 28G, EPS P-5.171 (2004).
45. M. J. MANTSINEN et al., *Nucl. Fusion*, **41**, 1815 (2001).
46. M. I. K. SANTALA et al., *Plasma Phys. Control. Fusion*, **48**, 1233 (2006).
47. M. J. MANTSINEN et al., *Nucl. Fusion*, **44**, 33 (2004).
48. D. VAN EESTER, *Plasma Phys. Control. Fusion*, **46**, 1675 (2004).
49. A. LYSSOIVAN et al., in *Radio Frequency Power in Plasmas*, Moran, Wyoming, C. B. FOREST, Ed., AIP Conf. Proc., Vol. 694, pp. 130–133 (2003).
50. D. VAN EESTER et al., in *Radio Frequency Power in Plasmas*, Moran, Wyoming, C. B. FOREST, Ed., AIP Conf. Proc., Vol. 694, pp. 66–73 (2003).
51. ITER PHYSICS BASIS EDITORS et al., *Nucl. Fusion*, **39**, 12 (1999).
52. M.-L. MAYORAL et al., *Nucl. Fusion*, **46**, S550 (2006).
53. L.-G. ERIKSSON et al., *Phys. Rev. Lett.*, **81**, 1231 (1998).
54. M. J. MANTSINEN et al., *Phys. Rev. Lett.*, **89**, 115004 (2002).
55. M. J. MANTSINEN et al., *Plasma Phys. Control. Fusion*, **47**, 1439 (2005).
56. T. HELLSTEN, *Plasma Phys. Control. Fusion*, **31**, 1391 (1989).

57. J. M. ADAMS et al., *Nucl. Fusion*, **31**, 891 (1991).
58. L. CHEN et al., in *Proc. 12th IAEA Conf. Plasma Physics and Controlled Nuclear Fusion Research*, Nice, France, Vol. 2, pp. 77–88, IAEA (1989).
59. M. J. MANTSINEN et al., *Nucl. Fusion*, **40**, 1773 (2000).
60. T. HELLSTEN et al., *Phys. Rev. Lett.*, **74**, 3612 (1995).
61. L.-G. ERIKSSON et al., *Plasma Phys. Control. Fusion*, **43**, R145 (2001).
62. A. SALMI et al., *Plasma Phys. Control. Fusion*, **48**, 717 (2006).
63. O. SAUTER et al., *Phys. Rev. Lett.*, **88**, 105001 (2002).
64. E. WESTERHOF et al., *Nucl. Fusion*, **42**, 1324 (2002).
65. F. PORCELLI et al., *Plasma Phys. Control. Fusion*, **38**, 2163 (1996).
66. V. P. BHATNAGAR et al., *Nucl. Fusion*, **34**, 1579 (1994).
67. M. J. MANTSINEN et al., *Plasma Phys. Control. Fusion*, **44**, 1521 (2002).
68. M. L. MAYORAL et al., *Phys. Plasmas*, **11**, 2607 (2004).
69. L.-G. ERIKSSON et al., *Phys. Rev. Lett.*, **92**, 235004 (2004).
70. L. G. ERIKSSON et al., *Nucl. Fusion*, **46**, S951 (2006).
71. L.-G. ERIKSSON et al., *Nucl. Fusion*, **29**, 875 (1989).
72. D. F. H. START et al., *Nucl. Fusion*, **30**, 2170 (1990).
73. C. C. PETTY et al., *Nucl. Fusion*, **35**, 773 (1995).
74. C. C. PETTY et al., *Nucl. Fusion*, **39**, 1421 (1999).
75. B. SAOUTIC et al., *Plasma Phys. Control. Fusion*, **36**, B123 (1994).
76. T. HELLSTEN et al., *Nucl. Fusion*, **45**, 706 (2005).
77. L.-G. ERIKSSON et al., *Plasma Phys. Control. Fusion*, **34**, 863 (1992).
78. H. HSUAN et al., in *Radio Frequency Power in Plasmas*, Palm Springs, California, AIP Conf. Proc., Vol. 355, p. 39 (1995).
79. J. E. RICE et al., *Nucl. Fusion*, **38**, 75 (1998).
80. J.-M. NOTERDAEME et al., *Nucl. Fusion*, **43**, 274 (2003).
81. L.-G. ERIKSSON et al., *Nucl. Fusion*, **42**, 959 (2002).
82. L.-G. ERIKSSON et al., *Phys. Rev. Lett.*, **92**, 235001 (2004).
83. M. J. MANTSINEN et al., *Phys. Rev. Lett.*, **88**, 105002 (2002).
84. S. E. SHARAPOV et al., *Nucl. Fusion*, **45**, 1168 (2005).
85. A. LYSSOIVAN et al., *J. Nucl. Mater.*, **337–339**, 456 (2005).
86. T. T. C. JONES et al., in *Proc. 28th EPS Conf. Controlled Fusion and Plasma Physics*, Funchal, Portugal, ECA Vol. 25A, pp. 1197–1200, EPS (2001).
87. A. MARINONI et al., *Plasma Phys. Control. Fusion*, **48**, 1469 (2006).
88. P. MANTICA et al., *Phys. Rev. Lett.*, **96**, 1 (2006).
89. V. BOBKOV et al., in *Proc. 31st EPS Conf. Plasma Physics*, London, United Kingdom, ECA Vol. 28G, EPS P-1.141 (2004).
90. G. DUESING et al., *Fusion Technol.*, **11**, 1, 163 (1987).
91. J. PAMELA, *Rev. Sci. Instrum.*, **57**, 1066 (1986).
92. T. T. C. JONES et al., *Fusion Eng. Des.*, **47**, 205 (1999).
93. C. CIRIC et al., in *Proc. 19th IEEE/NPSS Symp. Fusion Engineering*, Atlantic City, New Jersey, pp. 140–142 (2002).
94. H. P. L. DE ESCH et al., in *Proc. 14th Symp. Fusion Engineering*, San Diego, California, Vol. 1, pp. 86–89 (1991).
95. D. COOPER et al., in *Proc. 16th Symp. Fusion Technology*, London, United Kingdom, Vol. 2, pp. 1109–1113 (1990).
96. A. J. BICKLEY et al., in *Proc. 13th Symp. Fusion Engineering*, Knoxville, Tennessee, p. 1438 (1989).
97. S. J. COX et al., in *Proc. 19th IEEE/NPSS Symp. Fusion Engineering*, Atlantic City, New Jersey, Vol. PC, pp. 1–18 (2002).
98. E. THOMPSON et al., *Phys. Fluids B*, **5**, 2468 (1993).
99. THE JET TEAM, *Plasma Phys. Control. Fusion*, **37**, A359 (1995).
100. T. T. C. JONES et al., *Phys. Plasmas*, **4**, 1725 (1997).
101. THE JET TEAM, *Nucl. Fusion*, **32**, 187 (1992).
102. THE JET TEAM, in *Proc. 16th IAEA Conf. Fusion Energy*, Montreal, Canada, Vol. 1, p. 239 (1996).
103. THE JET TEAM (presented by M. KEILHACKER), *Plasma Phys. Control. Fusion*, **39**, B1 (1997).
104. M. KEILHACKER, *Philos. Trans. R. Soc. London, Ser. A*, **357**, 415 (1999).
105. M. F. F. NAVE et al., *Nucl. Fusion*, **37**, 809 (1997).
106. T. H. STIX, *Plasma Phys. Control. Fusion*, **14**, 367 (1972).
107. W. OTT, “Neutral Beam Modulation for Heating Profile Measurements,” IPP4/276, Max-Planck Institut für Plasmaphysik (1997).
108. P. R. THOMAS et al., *Phys. Rev. Lett.*, **80**, 5548 (1998).
109. S. E. SHARAPOV et al., *Fusion Sci. Technol.*, **53**, 989 (2008).
110. F. B. MARCUS et al., *Plasma Phys. Control. Fusion*, **34**, 1371 (1992).
111. S. A. COHEN et al., *Plasma Phys. Control. Fusion*, **29**, 1205 (1987).
112. T. T. C. JONES et al., *J. Nucl. Mater.*, **162–164**, 503 (1989).
113. D. STORK et al., *J. Nucl. Mater.*, **176–177**, 408 (1990).
114. R. J. GOLDSTON et al., *J. Comput. Phys.*, **43**, 61 (1981).
115. G. FEDERICI et al., *Nucl. Fusion*, **41**, 1967 (2001).
116. T. T. C. JONES et al., in *Proc. 18th European Conf. Controlled Fusion and Plasma Physics*, Berlin, Germany, Vol. 15C, p. 185, EPS (1991).
117. M. R. WADE, *Phys. Plasmas*, **2**, 2357 (1995).
118. A. SAKASAI et al., *J. Nucl. Mater.*, **220–222**, 405 (1995).
119. A. SAKASAI, in *Proc. 17th IAEA Conf. Fusion Energy*, Yokohama, Japan, IAEA-CSP-1/C, EX6/5 (1998).
120. A. SAKASAI, in *Proc. 18th IAEA Conf. Fusion Energy*, Sorrento, Italy, IAEA-CSP-8/C, EX5/5 (2000).
121. K.-D. ZASTROW et al., *Nucl. Fusion*, **45**, 163 (2005).
122. D. STORK et al., *Nucl. Fusion*, **45**, S181 (2005).
123. J. W. CONNOR et al., *Nucl. Fusion*, **14**, 185 (1974).
124. J. A. WESSON, *Tokamaks*, p. 133, Oxford University Press (1997).
125. C. D. CHALLIS et al., *Nucl. Fusion*, **29**, 563 (1989).
126. C. GORMEZANO et al., *Fusion Sci. Technol.*, **53**, 958 (2008).
127. F. L. HINTON et al., *Phys. Fluids*, **27**, 1243 (1984).
128. H. P. L. DE ESCH et al., in *Proc. 17th EPS Conf. Controlled Fusion and Plasma Physics*, Amsterdam, The Netherlands, Vol. 14B, Part 1, pp. 90–93, EPS (1990).
129. K.-D. ZASTROW et al., *Nucl. Fusion*, **38**, 257 (1998).

130. P. C. DE VRIES et al., *Plasma Phys. Control. Fusion*, **48**, 1693 (2006).
131. D. CIRIC et al., in *Proc. 24th Symp. Fusion Technology*, Warsaw, Poland (2006).
132. C. GORMEZANO, *Plasma Phys. Control. Fusion*, **28**, 9A, 1365 (1986).
133. C. GORMEZANO et al., in *Proc. 10th IAEA Conf. Fusion Energy*, London, United Kingdom, CN-44, Vol. 1, p. 513, IAEA (1984).
134. C. GORMEZANO et al., *Nucl. Fusion*, **25**, 419 (1985).
135. M. PAIN et al., in *Proc. 13th Symp. Fusion Engineering*, Knoxville, Tennessee, Vol. 2, IEEE, New York (1989).
136. J. A. DOBBING et al., in *Proc. 17th Symp. Fusion Technology*, Rome, Italy, Vol. 1, p. 472, Elsevier Science, The Netherlands (1992).
137. A. EKEDAHL et al., *Plasma Devices Oper.*, **5**, 315 (1998).
138. A. EKEDAHL et al., *Nucl. Fusion*, **38**, 1397 (1998).
139. K. K. KIROV et al., in *Radio Frequency Power in Plasmas*, Park City, Utah, S. J. WUKITSCH, Ed., AIP Conf. Proc., Vol. 787, p. 305 (2005).
140. M. GONICHE et al., JET-R(97)14 (1997).
141. V. FUCHS et al., *Phys. Plasmas*, **3**, 4023 (1996).
142. P. JACQUET et al., CCFM RI 474e, Centre Canadien de Fusion Magnétique (1997).
143. K. M. RANTAMAKI et al., *Plasma Phys. Control. Fusion*, **47**, 1101 (2005).
144. M. GONICHE et al., *Nucl. Fusion*, **38**, 919 (1998).
145. K. M. RANTAMAKI et al., in *Radio Frequency Power in Plasmas*, Clearwater, Florida, P. M. RYAN, Ed., AIP Conf. Proc., Vol. 933, pp. 261–264 (2007).
146. M. BRAMBILLA, *Nucl. Fusion*, **16**, 47 (1976).
147. P. JACQUET et al., *Rev. Sci. Instrum.*, **68**, 1176 (1997).
148. X. LITAUDON et al., *Nucl. Fusion*, **30**, 471 (1990).
149. D. MOREAU et al., EUR-CEA-FC-1246, CEA (1984).
150. A. EKEDAHL et al., in *Radio Frequency Power in Plasmas*, Oxnard, California, T. K. MAU, Ed., AIP Conf. Proc., Vol. 595, pp. 249–252 (2001).
151. F. LEUTERER et al., *Plasma Phys. Control. Fusion*, **33**, 169 (1991).
152. A. EKEDAHL et al., in *Radio Frequency Power in Plasmas*, Savannah, Georgia, P. M. RYAN, Ed., AIP Conf. Proc., Vol. 403, pp. 169–172 (1997).
153. B. FISCHER et al., in *Proc. 22nd EPS Conf. Controlled Fusion and Plasma Physics*, Bournemouth, United Kingdom, Vol. 19C, Part III, p. 361, EPS (1995).
154. F. SOLDNER et al., in *RF Power in Plasmas*, Annapolis, Maryland, S. BERNABEI, Ed., AIP Conf. Proc., Vol. 485, p. 288 (1999).
155. J. STRACHAN et al., *J. Nucl. Mater.*, **290–293**, 972 (2001).
156. V. PERICOLI RIDOLFINI et al., *Plasma Phys. Control. Fusion*, **46**, 349 (2004).
157. A. TARONI et al., in *Proc. IAEA Conf. Fusion Energy*, Montreal, Canada, IAEA-CN-64/D3-3 Vol. 2, p. 477 (1996).
158. G. MATTHEWS et al., *Plasma Phys. Control. Fusion*, **44**, 689 (2002).
159. J. MAILLOUX et al., in *Proc. 28th EPS Conf. Controlled Fusion and Plasma Physics*, Madeira, Portugal, Vol. 25A, pp. 793–796, EPS (2001).
160. F. CRISANTI et al., *Phys. Rev. Lett.*, **88**, 14504-1 (2002).
161. X. LITAUDON et al., *Plasma Phys. Control. Fusion*, **44**, 1057 (2002).
162. G. JANESCHITZ et al., *Nucl. Fusion*, **42**, 14 (2002).
163. A. EKEDAHL, *Nucl. Fusion*, **45**, 351 (2005).
164. J. ONGENA et al., in *Radio Frequency Power in Plasmas*, Clearwater, Florida, P. M. RYAN, Ed., AIP Conf. Proc., Vol. 933, pp. 249–256 (2007).
165. V. PETRZILKA et al., in *Proc. 33rd EPS Conf. Plasma Physics*, Rome, Italy (2006) (submitted to *Nucl. Fusion*).
166. K. KIROV et al., in *Radio Frequency Power in Plasmas*, Park City, Utah, S. WUKITCH, Ed., AIP Conf. Proc., Vol. 737, pp. 315–318 (2005).
167. M. BÉCOULET et al., *Phys. Plasmas*, **9**, 2619 (2002).
168. Y. F. BARANOV et al., *Nucl. Fusion*, **36**, 1031 (1996).
169. C. GORMEZANO et al., *Fusion Sci. Technol.*, **45**, 303 (2004).
170. P. FROISSARD et al., in *Proc. 18th EPS Conf. Controlled Fusion and Plasma Physics*, Berlin, Germany, Vol. 15C, Part III, p. 389, EPS (1991).
171. M. BRUSATI et al., *Nucl. Fusion*, **34**, 23 (1994).
172. D. P. O'BRIEN et al., *Nucl. Fusion*, **32**, 1351 (1992).
173. V. PERICOLI RIDOLFINI et al., *Plasma Phys. Control. Fusion*, **39**, 1115 (1997).
174. C. GORMEZANO et al., in IAEA Technical Committee Meeting in Fast Wave Current Drive in Reactor Scale Tokamaks, Arles, France, p. 244, IAEA (1991).
175. G. CENACCHI et al., "A Free-Boundary Plasma Transport Code (Basic Version)," JET-IR(88)03, JET Joint Undertaking, Abingdon, United Kingdom (1988).
176. J. MAILLOUX et al., in *Proc. 20th IAEA Conf. Fusion Energy*, Vilamoura, Portugal, Vol. IAEA-CSP-25/CD, EX/P4-28, IAEA (2004).
177. V. BASIUK et al., *Nucl. Fusion*, **43**, 822 (2003).
178. J. MAILLOUX et al., *Phys. Plasmas*, **9**, 2156 (2002).
179. M. C. RAMOS DE ANDRADE et al., *Plasma Phys. Control. Fusion*, **36**, 1171 (1994).
180. D. TESTA et al., *Plasma Phys. Control. Fusion*, **41**, 507 (1999).
181. T. T. C. JONES et al., *Plasma Phys. Control. Fusion*, **37**, A359 (1995).
182. THE JET TEAM (presented by P. J. LOMAS), in *Proc. 16th IAEA Conf. Fusion Energy*, Montreal, Canada, Vol. 1, p. 239, IAEA (1996).
183. THE JET TEAM (presented by P. THOMAS), in *Proc. 16th IAEA Conf. Fusion Energy*, Montreal, Canada, Vol. 1, p. 331, IAEA (1996).
184. THE JET TEAM (presented by J. JACQUINOT), in *Proc. 16th IAEA Conf. Fusion Energy*, Montreal, Canada, Vol. 1, p. 57, IAEA (1996).
185. THE JET TEAM (presented by C. GORMEZANO), in *Proc. 16th IAEA Conf. Fusion Energy*, Montreal, Canada, Vol. 1, p. 487 (1996).
186. C. GORMEZANO et al., *Phys. Rev. Lett.*, **80**, 5544 (1998).
187. A. C. C. SIPS et al., *Plasma Phys. Control. Fusion*, **40**, 1171 (1998).
188. C. D. CHALLIS et al., *Plasma Phys. Control. Fusion*, **44**, 1031 (2002).

189. N. C. HAWKES et al., *Phys. Rev. Lett.*, **87**, 115001 (2001).
190. N. C. HAWKES et al., *Plasma Phys. Control. Fusion*, **44**, 1105 (2002).
191. R. DUX et al., in *Proc. 28th EPS Conf. Controlled Fusion and Plasma Physics*, Madeira, Portugal, Vol. 25A, p. 505, EPS (2001).
192. X. LITAUDON et al., in *Proc. 21st IAEA Fusion Energy Conf.*, Chengdu, China, IAEA-CN-149, STI/PUB/1292, EX/P1-12 (2006).
193. E. JOFFRIN et al., *Plasma Phys. Control. Fusion*, **45**, A367 (2003).
194. D. MOREAU et al., *Nucl. Fusion*, **43**, 870 (2003).
195. D. MAZON et al., *Plasma Phys. Control. Fusion*, **45**, L47 (2003).
196. F. CRISANTI et al., in *Proc. 30th EPS Conf. Plasma Physics and Controlled Fusion*, St Petersburg, Russia, Vol. 27A, EX/P2-1, EPS (2003).
197. E. JOFFRIN et al., *Nucl. Fusion*, **45**, 626 (2005).
198. A. SIPS et al., *Plasma Phys. Control. Fusion*, **44**, B69 (2002).
199. C. GORMEZANO et al., *Plasma Phys. Control. Fusion*, **46**, B435 (2004).
200. S. GÜNTER et al., *Nucl. Fusion*, **44**, 524 (2004).
201. M. WATKINS et al., in *Proc. 21st IAEA Conf. Fusion Energy*, Chengdu, China, IAEA-CN-149, STI/PUB/1292, OV/1-3 (2006).
202. A. A. TUCCILLO et al., *Plasma Phys. Control. Fusion*, **47**, B363 (2005).
203. F. IMBEAUX et al., *Plasma Phys. Control. Fusion*, **47**, B179 (2005).
204. M. KEILHACKER et al., *Nucl. Fusion*, **39**, 209 (1999).
205. T. T. C. JONES et al., in *Proc. 25th EPS Conf. Controlled Fusion and Plasma Physics*, Prague, Czech Republic, Vol. 22C, p. 368, EPS (1998).
206. F. IMBEAUX et al., EUR-CEA-FC-1679 (1999).